UNIVERSITÀ DEGLI STUDI DI BOLOGNA

Dipartimento di Fisica "Augusto Righi"

Corso di Dottorato di Ricerca in Fisica

XIX ciclo

settore FIS/02

THE NATURE OF DARK ENERGY:

THEORETICAL ASSUMPTIONS AND EXPERIMENTAL TESTS

Relatori: Prof. Roberto BALBINOT

Prof. Silvio BONOMETTO

Coordinatore: Prof. Fabio ORTOLANI

Tesi di Dottorato di:

Luciano CASARINI

"Guarda quante ce ne sono! Milioni di milioni di milioni di stelle. Ragazzi io mi domando come cavolo fa a reggersi tutta 'sta baracca! Perchè per noi, dico così per dire, in fondo è abbastanza facile. Devo fare un palazzo? Tot mattoni, tot quintali di calce... ma lassù, viva la madonna, dove le mettono le fondamenta?! Non son mica coriandoli."

Federico Fellini, 1973, "Amarcord"

Contents

Chapter 1

The dark side of the Universe

Modern cosmology is a daughter of Albert Einstein's Relativity. However, modern cosmology seems to amuse jeopardising the very bases of Relativity. The upper limit to possible velocities, the speed of light c, is challenged by the superluminal expansion outside the horizon. When the Cosmic Microwave Background (CMB) was discovered, the Lorentz equivalence of all systems of reference was challenged by the existence of a privileged system, *at rest* in respect to the CMB. Finally, after it became clear that most of the Universe is *dark*, the very equivalence between mass and energy is challenged by the distinction between *Dark Matter* (DM) and *Dark Energy* (DE).

None of the above acquisitions contradicts Relativity, of course. They are absolutely coherent with Einstein's wisdom. In this thesis, however, I shall focus on the last of these apparent paradoxes, discussing theory and phaenomenology of DE, a dark substance whose features are radically different from bayonic matter and DM.

Current observations require that $\sim 95\%$ of the energy density of the world cannot be ascribed to quanta enclosed within the standard model of elementary particles. These forms of matter or energy have no apparent interaction, apart of gravity, with ordinary matter. In particular, they do not emit light. Hence, they form the *dark sector* of the world.

Their direct observation is being attempted in several ways, but, up to now, there are scarce evidences in this direction. On the contrary, in the large volumes observed by astrophysical tools, their gravity is dominant and refusing their existence implies major modifications of newtonian gravity.

Though there are presently no direct observations of the dark sector, there are nevertheless many indirect measurements that give us clues about its nature. Rotation curves of spiral galaxies, temperature profiles of galaxy clusters, gravitational lensing by clusters, large-scale motions of galaxies between clus-

ters, the virial theorem applied to clusters, all require a mass much larger than what emits the observed light (see, e.g., Persic et al. 1995, Bahcall 1996, Freedman 1999, Turner 2000). A part of such mass could still have a baryonic nature, being due to various types of collapsed objects (black holes, brown dwarfs or dim white dwarfs, jupiters, etc.) or to dust, cold gas, etc.. Constraints on the amount of such baryonic component come from big–bang nucleosynthesis (BBNS) and from the amplitude of the anisotropies of the cosmic microwave background (CMB). They coherently prescribe that, altogether, baryons cannot exceed a fraction ~ 0.05 of the critical density of the world. On the contrary, a large deal of data require that the total world density is very close to its critical value. This is why an extra dark component, made of non–baryonic particles is compulsory. We shall refer to it as cold dark matter (CDM), giving for granted that it is a pressureless continuum. Numerical studies of structure formation and comparison with statistical studies of galaxy and/or cluster distributions support the CDM model on large scales.

But CDM is not the only dark component of the world. A first evidence of a second dark component came from the observation of the magnitude–redshift relation for Type Ia supernovae (SNIa; Riess et al 1998, Perlmutter et al. 1998, Tonry et al. 2003), which can be treated as standard candles. The observed relation requires that the world is now undergoing a phase of accelerated expansion. According to the Friedmann equations, this is possible only if a component exists with a negative pressure $p_{DE} \ll -\rho_{DE}/3$: here ρ_{DE} is the energy density of such component, currently dubbed Dark Energy (DE). The possibility that DE is a kind of *false*–vacuum was soon envisaged. This is formally equivalent to a Lemaitre model with a positive cosmological constant. In the next section we shall discuss this hypothesis and its implications, as far as fine tuning requirements are concerned.

Another candidate for DE is a scalar field ϕ, self interacting through a suitable potential density $V(\phi)$. Also this hypothesis will be widely discussed in the next chapters and we shall refer to that as *dynamical* DE.

Let us however outline soon that the evidence based on SNIa is not isolated and has been later reinforced by lots of independent observations. None of them indicates that the world expansion is accelerated, but all of them tell us that the sum of CDM and baryon densities is far less than critical, while the total density of the world is quite close to the critical value. Among such observations, let us remind those of deep galaxy samples, like the 2dF sample (Percival et al 2001, Efstathiou et al 2002), and the recent global parameter

estimates made by WMAP (Bennett et al 2003), confirming previous findings based on CMB observations (see, e.g., De Bernardis et al 2001, Hanany et al 2001, Spergel et al 2006).

Deep galaxy samples give evidence that the clustered matter, including baryons and DM, only comprises one-third of the energy density required for a flat Universe, while they also require that the world density is close to its critical value. This implies that a smoothly distributed DE component exists. Also CMB observations require that the total density is close to critical, because of the location of the first peak of the anisotropy spectrum, showing that the space section of the world model is (nearly) flat. Furthermore, their analysis confirms that CDM and baryons account for $\sim 30\,\%$ of the critical density.

A convenient parameterization of DE nature is provided by the so–called *state parameter* $w = p_{DE}/\rho_{DE}$. Assuming that w is constant in time, SNIa and other data yield the restriction $-1.62 < w < -0.74$ (see, e.g., Melchiorri et al. 2002). A false vacuum (cosmological constant) yields $w = -1$. Dynamical DE normally imply that $w > -1$, but is close to such value. It comes then as no surprise that some authors considered also the possibility that $w < -1$ (this case is dubbed *phantom* DE, ...). Should future observations indicate $w < -1$, what does this imply? First of all one should carefully examine if this is an apparent indication arising from a multiple component dark sector or from a rapidly varying w. Should all this be excluded, the new physics implicit in such range of values would have really exceptional features, violating the generally accepted condition on matter, called "*dominant energy condition*" (Carroll et al. 2003). In this thesis we shall not deal with phantom DE.

It is also important to outline that, at present, no observation requires DE with $w \neq -1$. The advantages of dynamical DE will be debated in the next chapter. In spite of that, the rapid accumulation of fresh observational material and the consequent reduction of observational uncertainties allow us to expect new stringent tests for the ΛCDM model, in the near future. It is therefore useful to have more general dark sector models, both to act as a foil to ΛCDM and as a possible replacement, should ΛCDM fail future tests.

Once DE is allowed to behave differently form a cosmological constant, a still more complicated dark sector cannot be excluded. In particular, models including an interaction between DM and DE are to be explored. Anderson and Carroll (1997) studied a cosmological model in which the dark matter particle mass was proportional to the expectation value of a scalar field. Similar models have also been studied by Bean (2001) and Farrar and Peebles (2003). Amen-

dola (1999) introduced a model with an exponential coupling between DM and a scalar field acting as DE. This model has been shown to be consistent with present CMB observations (Amendola & Tocchi Valentini 2002, Amendola & Quercellini 2003) and admits a late time attractor solution, yielding a ratio 1/2 between DM and DE densities, close to data. Other schemes for interactions within the dark sector have also been proposed by various authors (i.e. Gasperini et al. 2001). We shall refer to these models as coupled DE.

Although being smoothly distributed today, dynamical or coupled DE can affect the evolution of density fluctuation. This can be due both to the very existence of primeval DE density fluctuations, affecting scales which have recently entered the horizon, and to indirect effects of DE state equation on the evolution of density fluctuations in other components (ISW effect). This must be taken into account when CMB properties are tested against DE parameters.

However, to test DE parameters against the present state of the world, also its impact on the non–linear evolution of density fluctuations can be considered.

This thesis will explore both contexts. CMB data can be confronted with *lenear* predictions of cosmological models. Data on cosmic systems, instead, require the use of non–linear physics. In this thesis I shall therefore report results of both linear and non–linear studies, the latter being based on N–body simulations, mostly performed with the ART code. Using these results we tested the behavior of a large set of non–linear observables which depend on DE nature.

1.1 Fine tuning problems

Pre–inflationary cosmology had plenty of fine tuning problems. Assuming a period of accelerated expansion in the early Universe allows to overcome most of them, simultaneously. Inflation makes the generic predictions that we ought to live in a Universe whose space section is flat, homogeneous and isotropic on the very large scales, characterized by early density fluctuations with a (nearly) Zel'dovich–Harrison spectrum, where topological monsters are absent. Hence, e.g., to admit that we live in a world whose density is (almost) critical, we no longer need to invoke exceptional initial conditions or suitable *fine tunings*.

The beauty of this achievement is spoiled if we assume that DE is due to a *false vacuum*. Replacing this kind of DE with DDE apparently eases the fine tuning problems, which become even less disturbing in the frame on CDE models. We should remind that the inflationary model is now currently accepted even though none has yet been able to implement its particle aspects. Quite

in the same way, there are various particle aspects of dynamical of coupled DE which need a further exam in the frame of particle physics. In spite of that, avoiding unpleasant fine tunings has become a valid motivation for cosmological advancements; DDE and CDE are to be considered in such perspective.

Let us now consider in more detail the fine tuning problems arising in ΛCDM models. The world self gravitation is currently studied on the basis of the Einstein equations:

$$R_{\mu\nu} - \frac{1}{2} g_{\mu\nu} R = \frac{8\pi G}{c^4} T_{\mu\nu}. \tag{1.1}$$

Here $R_{\mu\nu}$ is the Riemann tensor and R is its trace. The Riemann tensor comprises first and second order derivatives of the metric tensor $g_{\mu\nu}$. Eq. (1.1) can be therefore considered a second order, non–linear equation in the unknown components of $g_{\mu\nu}$, whose dependence on the metric coordinates is fixed by its solution. $T_{\mu\nu}$, instead, is the stress–energy tensor, whose components are linked to energy and momentum densities. From this point of view, eq. (1.1) is strictly analogous to the Poisson equation in electromagnetism, whose source term is the electric 4–current j_μ.

However, while differentiating the Poisson equation we obtain a continuity equation, whose meaning is that the *electric charge* is conserved, in the case of Einstein equation, the equation

$$T^{\mu}_{\nu;\mu} = 0 \tag{1.2}$$

follows, which yields a sort of (pseudo–)conservation of energy and momentum, apart of their modifications due to the effects of gravity.

Here we shall use the Friedman–Robertson–Walker metric

$$ds^2 = c^2 dt^2 - a^2(t)\left[\frac{dr^2}{1-\kappa r^2} + r^2 d\Omega^2\right] \quad \text{with} \quad d\Omega^2 = d\theta^2 + \sin^2\theta\, d\phi^2 \tag{1.3}$$

and both eq. (1.1) and (1.3) will be considered in the forms involving directly the scale factor a and the curvature constant κ only.

The stress–energy tensor $T_{\mu\nu}$ can also be considered in a reference frame where the metric is locally minkowskian, with reference to carthesian orthogonal axes. In the absence of anisotropic stresses, in such frame, its components are purely diagonal and $T_{00} = \rho$ (energy density), while $T_{ii} = p$ (pressure; $i = 1, 2, 3$).

Among the expressions that $T_{\mu\nu}$ can have, let us consider the case

$$T_{\mu\nu} = \Lambda g_{\mu\nu} \ , \tag{1.4}$$

Clearly, in this case, $-p = \rho = \Lambda$. Eq. (1.2), in the case of the FRW metric given by eq. (1.3), becomes

$$\dot{\rho} = -3\frac{\dot{a}}{a}(\rho + p) \tag{1.5}$$

and yields $\rho =$ const. if $\rho = -p$, as it is if $T_{\mu\nu}$ has the expression (1.6).

More in general, we may consider the case when

$$T_{\mu\nu} = T^{(m)}_{\mu\nu} + \Lambda g_{\mu\nu} \tag{1.6}$$

and replace it in the eq.(1.1), so obtaining

$$R_{\mu\nu} - \frac{1}{2}g_{\mu\nu}(R + 2\lambda) = \frac{8\pi G}{c^4}T^{(m)}_{\mu\nu} \tag{1.7}$$

if

$$\lambda = \frac{8\pi G}{c^4}\Lambda\ . \tag{1.8}$$

Eq. (1.7) is the generalization of Einstein equation, introduced by Einstein himself, enclosing the *cosmological constant* λ. In this equation, however, also negative λ values are admissible. Leaving them apart, however, there is a complete identity between introducing a cosmological constant and taking a time independent background energy density $\rho = \Lambda$, as is obtained form a source term with the expression (1.6).

Bearing this in mind, let us now discuss observational limits on Λ. They are related to the fact that this *vacuum* energy density cannot exceed the total energy density of the world, as is determined through CMB and SNIa observations. Accordingly,

$$\rho_\Lambda < 4 \times 10^{-29}\ \ \mathrm{gcm}^{-3} \simeq 10^{-46}\frac{m_n^4}{(\hbar/c)^3}. \tag{1.9}$$

Here m_n is the nucleon mass. In natural units ($\hbar = c = 1$), this equation also reads

$$\rho_\Lambda < 10^{-48}\mathrm{GeV}^4. \tag{1.10}$$

and therefore yields

$$\Lambda < 10^{-12}\mathrm{GeV} \simeq 10^{-55}\mathrm{cm}^{-1}. \tag{1.11}$$

The problem with the cosmological constant is that Λ and/or ρ_Λ are so amazingly and unnaturally small. If ρ_Λ and p_Λ represent the density and pressure of a *false vacuum*, which is understood to be the ground state of a quantum system ($\rho_\Lambda \equiv \rho_v$), we ought to compare the above values with modern theories of elementary particles with spontaneous symmetry breaking, for which:

$$\rho_v \sim V(\Phi, Temp = 0), \tag{1.12}$$

$V(\Phi, T)$ being the effective potential of the scalar field Φ (Higgs' field) responsible for spontaneous symmetry breaking. The order of magnitude of ρ_v should then not be too far from T_C^4, T_C being the transition temperature, where the symmetry naturally breaks down.

Accordingly, the jump in vacuum energy density $\Delta\rho_v$, occurring at the temperatures $T_{GUT} \simeq 10^{15}$GeV (for the GUT transition), 10^2GeV (for the electroweak transition), 10^{-1}GeV (for the quark–hadron transition, if it is a first–order phase transition) should be of orders 10^{60}GeV^4 (for GUT), 10^8GeV^4 (for the EW transition) and 10^{-4}GeV^4 (for QCD).

In the light of these previous comments the cosmological constant problem can be rephrased as follows:

$$\begin{aligned} &\rho_v(t_P) = \rho_v(t_0) + \textstyle\sum_i \Delta\rho_v(T_{Ci}) \simeq 10^{-48}\ \ \text{GeV}^4 + 10^{60}\ \ \text{GeV}^4 = \\ &= \textstyle\sum_i \Delta\rho_v(T_{Ci})(1 + 10^{-108}), \end{aligned} \tag{1.13}$$

where $\rho_v(t_P)$ and $\rho_v(t_0)$ are the vacuum density at the Plank and present times respectively and T_{Ci} are the transition temperature of the various phase transitions occurring between t_P and t_0. Equation (1.13) can be phrased in two ways: $\rho_v(t_P)$ must differ from $\sum_i \Delta\rho_v(m_i)$ over the successive phase transitions by only one part in 10^{108} or the sum $\sum_i \Delta\rho_v(m_i)$ must, in some way, arrange itself so as to satisfy (1.13). Either way, there is a definitely problem of *fine tuning* in terms of $\rho_v(t_P)$ or $\sum_i \Delta\rho_v(m_i)$.

It was in view of these problems that most cosmologists refrained from considering models with a cosmological constant, until quite recently, and that Einstein himself considered the cosmological constant as the worst *blunder* in its research life. In spite of all that, current cosmological observations apparently require, with a good confidence level, a component of the Universe with negative pressure. Indeed, many cosmologists regard this requirement as the most serious problem in modern cosmology.

When this was made clear, ideas to avoid the above fine–tuning ugliness were urgently seeken. The main outcome of this quest was the possibility that DE arises from a self interactive scalar field, similarly to what took place during inflation. We shall discuss such idea in the next section.

1.2 Dynamical Dark Energy

An accelerated expansion can arise not only in the presence of a world component with $w = -1$, as is for the false vacuum, but also if there is a component

whose clustering scale exceeds the large scale structures and whose energy density decreased more slowly than non relativistic matter, during the expansion of the Universe. In this way, today, this kind of DE became dominant and causes the expansion to accelerate.

Such a component could have a state equation $p = w\rho$, with a constant $w > -1$, but close to -1. In some recent work this *ad–doc* component was seriously considered. Unfortunately, it is even less justified, on physical bases, than false vacuum itself, requiring us to accept that we are dealing with an approximate treatment of more complex physics still to be unveiled.

Dynamical Dark Energy (DDE), to our knowledge, is then the main alternative to false vacuum and the only one, up to now, apparently avoiding its fine tuning problems. In some papers DDE was also dubbed as *quintessence*. In this thesis we shall deliberately avoid to use such an *alchemic* appellation.

1.2.1 Lagrangian approach

DE is due to a scalar field ϕ, which self–interacts through a suitable potential (density) $V(\phi)$. More in detail, let

$$\mathcal{L} = -\frac{1}{2}\sqrt{-g}\left[\partial^{\mu}\phi\,\partial_{\nu}\phi + 2V(\phi)\right] \qquad (\mu,\nu = 0,1,2,3) \tag{1.14}$$

be the lagrangian density of the field. Here g is the determinant of the metric. Assuming spatial homogeneity ($\partial_i\phi = 0, \quad i = 1,2,3$), the Eulero-Lagrange equations read:

$$\ddot{\phi} + 2\frac{\dot{a}}{a}\dot{\phi} + a^2\frac{dV}{d\phi} = 0\ . \tag{1.15}$$

Here dots represent derivation with respect to conformal time τ ($d\tau = dt/a$). The cosmic expansion interferes with the dynamics of ϕ thanks to the *friction term* $2(\dot{a}/a)\dot{\phi} = 2aH\dot{\phi}$, H being the standard Hubble parameter when the scale factor is a. In turn, H depends on the state equation of the dominant component of the Universe: e.g., when the transition from radiation to matter dominance occurs, at $z \sim 10^4$, this causes a variation in the rate of ϕ variation.

From the expression (1.14) we obtain the stress–energy tensor:

$$T^{\mu}_{\nu} = \partial^{\mu}\phi\,\partial_{\nu}\phi - \frac{1}{2}\left[\partial^{\alpha}\phi\,\partial_{\alpha}\phi + 2V(\phi)\right]\delta^{\mu}_{\nu}; \tag{1.16}$$

in the homogeneity limit, the energy density then reads

$$\rho_{\phi} = T^{0}_{0} = \frac{\dot{\phi}^2}{2a^2} + V(\phi), \tag{1.17}$$

while the pressure is

$$p_{\phi} = \frac{1}{3}T^{i}_{i} = \frac{\dot{\phi}^2}{2a^2} - V(\phi). \tag{1.18}$$

Accordingly, the *state parameter*

$$w \equiv \frac{p_\phi}{\rho_\phi} = \frac{\dot{\phi}^2/2a^2 - V(\phi)}{\dot{\phi}^2/2a^2 + V(\phi)} \tag{1.19}$$

is time dependent and lays between 1, when the kinetic energy density $\rho_k = \dot{\phi}^2/2a^2$ widely exceeds $V(\phi)$, and -1, when $\rho_k \ll V$. In the latter case, the effects of the ϕ field approach those of a cosmological constant.

The actual behavior of ϕ depends on the shape of V; there are important cases when its behavior is quite far from DE. An example is the dynamics of the Peccei–Quinn (1977) scalar field, after the global symmetry $U(1)$ is spontaneously broken and the scalar axion field A becomes subject to a potential

$$V(A) = m_a^2 F_a^2 [1 - \cos(A/F_a)] \ , \tag{1.20}$$

where F_a is an energy scale ranging around 10^{11}GeV, and m_a will turn out to be the variable axionic mass. When $A \ll F_a$, the potential $V(A)$ becomes $\simeq m_a^2 A^2$ and the equation of motion approaches that of an harmonic oscillator. Accordingly $\langle \rho_k \rangle \simeq \langle V \rangle$ and $\langle p \rangle = 0$, so that the axion field behavior approaches CDM, as is known.

The ρ_k/V ratio, therefore, determines the cosmological effects of ϕ. If $\rho_k/V < 1/2$, $w < -1/3$; values of w close to -1 require that $\rho_k \ll V$.

In order to know such ratio, eq. (1.15) must be solved. In most relevant cases it will yield a monotonic behavior for ϕ, which is significantly affected by the friction term. Accordingly, the DE state parameter w will show substantial variations when the expansion law changes.

1.2.2 Scale factor evolution

There are however some general relations which hold for any behavior of w and ought to be outlined, being of practical use. In this subsection we shall use the ordinary time t, instead of the conformal time τ, and dots will indicate differentiation in respect to t.

Quite in general, according to the Friedmann equations, the scale factor $a(t)$ of flat models obeys the relation

$$\frac{\dot{a}}{a} = H_o \sqrt{\frac{\rho(a)}{\rho_{cr,0}}} \ , \tag{1.21}$$

H_0 being the present Hubble parameter, ρ_{cr} being the critical density at a generic time and $\rho_{cr,0}$ being its present value; here

$$\rho(a) = \frac{\rho_{m,0}}{a^3} + \frac{\rho_{r,0}}{a^4} + \frac{\dot{\phi}^2}{2} + V(\phi) \ , \tag{1.22}$$

figure=fig/evo.ps,angle=0.,height=8.0truecm

Figure 1.1: Time evolution of dt/da for and DE models.

with a clear meaning of symbols. From eq. (1.22), at low z, we can safely omit radiation contributes. Then, for flat models, at any time,

$$\rho_\phi = \frac{\dot{\phi}^2}{2} + V(\phi) = \rho_{cr}(a)[1-\Omega_m(a)] = \rho_m(a)\frac{1-\Omega_m(a)}{\Omega_m(a)} \tag{1.23}$$

and the Friedmann equation reads

$$\left(\frac{\dot{a}}{a}\right)^2 = \frac{8\pi}{3}G\rho_m(a)\left[1+\frac{1-\Omega_m(a)}{\Omega_m(a)}\right] = \frac{8\pi}{3}G\frac{\rho_{m,0}}{a^3\Omega_m(a)}\ , \tag{1.24}$$

so that:

$$\dot{a} = H_0\sqrt{\frac{\Omega_{m,0}}{a\Omega_m(a)}}\ . \tag{1.25}$$

This equation holds regardless of the equation of state of DE, and can also be inverted providing the derivative

$$\frac{dt}{da} = H_0^{-1}\sqrt{\frac{a\Omega_m(a)}{\Omega_{m,0}}} \tag{1.26}$$

that shall be explicitly used in N-body simulations.

In figure 1.1 the time dependence of dt/da for and two DE models (for all of them $\Omega_m = 0.3$ and $h = 0.7$) is shown. A decrease of dt/da indicates the onset of cosmic acceleration. Eq. (1.5), equivalent to the equation $T^w_{\mu\nu} = 0$ on the stress–energy tensor, can also read

$$d(\rho_{DE}a^3) = -p_{DE}d(a^3) \tag{1.27}$$

and, replacing at the r.h.s. $p_{DE} = w\,\rho_{de}$, can be integrated by parts, yielding

$$\rho_{DE} = \rho_{DE,0}\exp\left[-3\ln(a) + 3\int_a^1 da\, w(a)/a\right]. \tag{1.28}$$

For $w = \text{const}$, eq. (1.28) simplifies into

$$\rho_{DE} = \rho_{DE,0}\, a^{-3(1+w)}. \tag{1.29}$$

and it is also possible to work out analytic expression yielding

$$\Omega_{DE}(z) = \Omega_{DE,0}\left[\frac{H_0}{H(z)}\right]^2(1+z)^{3(1+w)}. \tag{1.30}$$

It may also be interesting to see what happens under the condition that

$$H^2 > V'', \tag{1.31}$$

with $V'' \equiv d^2V/d\phi^2$. A first consequence of such condition is that $\dot{\phi}$ is almost constant in time. In fact, when it is so,

$$\dot{\phi} = -V'/H, \tag{1.32}$$

and differentiating this relation in respect to t, we have that

$$\ddot{\phi} \sim \frac{V''}{H}\dot{\phi} \ll H\dot{\phi}. \tag{1.33}$$

Using eq. (1.32), it is then

$$\dot{\phi}^2 = \frac{V'^2}{H^2} \sim \frac{V\,V''}{H^2} \ll V \ , \tag{1.34}$$

so that the kinetic term is negligible in respect to the potential. Accordingly, if eq. (1.31) holds, DE behavior approaches false vacuum.

1.2.3 Potentials

Before discussing in detail properties linked to the potential shape, it may now be worth listing some of the potentials considered in the literature.

- $V(\phi) = \frac{\Lambda^{4+\alpha}}{\phi^\alpha}$ (Ratra & Peebles 1988)
- $V(\phi) = \frac{\Lambda^{4+\alpha}}{\phi^\alpha} e^{\frac{\kappa}{2}\phi^2} \quad \kappa = 8\pi G = 8\pi/m_p^2$ (Brax & Martin 1999,2000)
- $V(\phi) = \Lambda^4 e^{-\lambda\phi}$ (Ratra & Peebles 1988, Ferreira & Joyce 1998)
- $V(\phi) = \Lambda^4[e^{\alpha\lambda\phi} + e^{\beta\lambda\phi}]$ (Barreiro, Copeland & Nunes 2000)
- $V(\phi) = \Lambda^4[1 + \cos\frac{\phi}{f}]$ (Kim 1999)
- $V(\phi) = \Lambda^4[(\phi - B)^\alpha + A]e^{-\lambda\phi}$ (Albrecht & Skordis 2000)
- $V(\phi) = \Lambda^4[\cosh(\lambda\phi) - 1]^p$ (Sahni & Wang 2000)

In this thesis we will deal only the first two potentials: $V(\phi) = \frac{\Lambda^{4+\alpha}}{\phi^\alpha}$ and $V(\phi) = \frac{\Lambda^{4+\alpha}}{\phi^\alpha} e^{\frac{\kappa}{2}\phi^2}$ (where $\alpha > 0$ is a dimensionless parameter and Λ is an energy-like parameter); the first one is called the Ratra-Peebles potential (RP hereafter) the second one the SUGRA (SUper GRAvity) potential. The RP potential coincides with SUGRA if $\phi \ll m_p$.

Most potentials listed above have a theoretical and particle physics motivation: in this thesis we focus our attention on the RP and SUGRA potentials without discussing their links with fundamental physics (for this subject see, e.g., Brax & Martin 1999, 2000; Copeland 2000; Hellerman et al. 2001).

From the cosmological point of view the most important feature that these potential should exhibit is the presence of *tracker solutions*.

1.3 Tracking potentials

Although in the present epoch DE is assumed to self–interact and to have gravitational interactions only, an implicit assumption is that, at very early times, possibly as early as inflation or Planck, it could be suitably coupled to the other cosmic components. This coupling, in principle, sets the initial conditions for the ϕ field, once the initial conditions of the other components are known. Trying to detail such primeval coupling is highly speculative and any hypothesis should be tested through its present cosmological consequences. Should they be significant, a further multi–dimensional parameter space opens and generic predictions become quite problematic.

Early work on DE (Zlatev et al. 1999, Steinhardt et al. 1999) took therefore much care to determine under which restrictions generic initial conditions leave no trace on the present ϕ field behavior. This program had success and, for a wide parameter space, within DE theories ruled by the above potentials, the present solutions of eq. (1.15) are not affected by early initial conditions. Such solution are then dubbed *tracker solutions* and potentials admitting tracker solutions are dubbed *tracking potentials*.

Let us now outline which restrictions are to be imposed to have tracker solutions. To this aim it is convenient to define the function

$$\Gamma = \frac{V^{''}V}{V^{'2}} \tag{1.35}$$

(the prime refers to differentiation with respect to ϕ) and it can be shown that tracker solutions exist if

$$\Gamma(\phi) \approx \text{constant} \quad \text{and} \quad \Gamma > 1 \ , \tag{1.36}$$

provided that, at early times, for example just after inflation, the *initial* DE density $\rho_{DE,i}$ fulfills the condition

$$\rho_{B,eq} < \rho_{DE,i} < \rho_{B,i} \ ; \tag{1.37}$$

here $\rho_{B,i}$ is the density of the radiative component (background component) which dominates the expansion at the *initial* time, while $\rho_{B,eq}$ is the background density at the equivalence time, when the relativistic and non–relativistic world component have an equal density.

To show this point, let us first define the new variable

$$x = \frac{1+w}{1-w} \tag{1.38}$$

and its logarithmic derivatives

$$\dot{x} = \frac{d\ln x}{d\ln a} \quad , \quad \ddot{x} \equiv \frac{d^2\ln x}{d\ln a^2} \, . \tag{1.39}$$

Steinhardt et al (1999) showed that, independently from the potential expression, and at any time, it is

$$\Gamma = 1 + \frac{\omega_B - w}{2\,(1+w)} - \frac{1+\omega_B - 2w}{2\,(1+w)}\frac{\dot{x}}{(6+\dot{x})} - \frac{2}{(1+w)}\frac{\ddot{x}}{(6+\dot{x})^2}. \tag{1.40}$$

Here ω_B is the state parameter of the world component which dominates the expansion.

If the first condition in eq. (1.36) is fulfilled, in eq. (1.40) $\dot{x}$ and $\ddot{x}$ must vanish and a solution with $w \simeq const$ must exist, that, owing to the second condition in eq. (1.36), is characterized by $w < \omega_B$. Accordingly, in this regime, ρ_{DE} is gradually approaching the background density.

1.4 The case for RP and SUGRA potentials

Most work reported in this thesis has dealt with *Ratra-Peebles* (RP) and *supergravity* (SUGRA) potentials. When $\phi \ll m_P$, the behavior of such potentials is identical. Values of $\phi \sim m_P$ are attained at the present epoch, when DE begins to dominate over the other world components, and ϕ is monotonically increasing during the whole cosmic expansion. Accordingly, at early times, all conclusions holding for RP can be extended to SUGRA.

It is easy to verify that both conditions in eq. (1.36) are satisfied by the RP potential

$$V(\phi) = \frac{\Lambda^{4+\alpha}}{\phi^\alpha}, \tag{1.41}$$

which simply yields $\Gamma = 1 + \alpha^{-1}$, showing that Γ is constant and greater than unity. Solutions with $w = \text{const}$, therefore, exist, provided that also $\omega_B = \text{const}$. According to eq. (1.40), with $\dot{x} = \ddot{x} = 0$, then

$$w = \frac{\alpha\omega_B - 2}{\alpha + 2} \tag{1.42}$$

By inserting this value in eq. (1.5), its integration is trivial and yields that

$$\rho_\phi \propto a^{-3(1+w)} \, . \tag{1.43}$$

By differentiating eq. (1.19) with respect to the time and using eq. (1.15), we also obtain that $\dot{\phi}^2 = -\dot{\rho}_\phi a^3/3\dot{a}$ and, therefore

$$\phi \propto a^{\frac{n}{\alpha+2}} \, . \tag{1.44}$$

figure=fig/w.ps,angle=0.,height=8.0truecm

Figure 1.2: Redshift dependence of w for 4 RP and 4 SUGRA models (Λ = 10,10^3,10^5 and 10^7 GeV; decreasing from top to bottom curves).

figure=fig/rho.ps,angle=0.,height=8.0truecm

Figure 1.3: Evolution of the matter, radiation and DE field energy density for a Ratra Peebles model (h=0.7)

Here n is 4 (3) for $\omega_B = 1/3$ (0).

In conclusion we can summarize the properties of the tracker solution:

- Both ϕ and ρ_ϕ approach a power-law behavior both in the radiation and matter dominated eras.
- The equation of state changes with the change in the expansion rate, according to eq. (1.42)
- The ratio between the kinetic and potential energy densities ($\frac{\dot{\phi}^2/2a^2}{V}$), given by $(1+w)/(1-w)$ is constant in time, until w keeps constant.

All these points hold until DE itself takes the lead. This occurs at different times, in different models, according to the value of Ω_m. In Fig. 1.3, we plot the redshift dependence of the state parameter w models with $\Omega_m = 0.3$.

The redshift at which ρ_{DE} can no longer be neglected is clearly indicated by the change in slope of the w curves. Owing to eq. (1.43), the redshift at which ρ_{DE} becomes dominant is given by

$$(1+z_{DE})^{3(-w)} = \frac{\Omega_{DE,o}}{\Omega_{m,o}}, \tag{1.45}$$

where the average is taken in the time interval after DE becomes dominant and it is explicitly outlined that density parameters, at the r.h.s., are to be taken with their present values. In the case of vacuum, being $w = -1$, if $\Omega_m = 0.3$, $z_{DE} \simeq 0.33$. For RP or SUGRA models, z_{DE} is suitably greater.

All this can be seen directly in Figs. 1.3 and 1.4, where we plot the behaviors of the densities ρ_i and the density parameters Ω_i (i =DE, matter, radiation) during the cosmic expansion.

figure=fig/omega.RP.ps,angle=0.,height=8.0truecm

Figure 1.4: Evolution of Ωs for matter, radiation and DE field for the same model of fig (1.3)

Before concluding this section it is important to outline that further tracker solutions hold, besides of those fulfilled by the ϕ field, in the spatial homogeneity limit. The initial condition problem described at the beginning of this section exists also for density fluctuations. Under the same conditions granting tracker solution for the background quantities, tracker solutions exist for the equations ruling fluctuation evolution.

Both kind of tracker solutions are essential to allow the implementation of linear programs, studying model evolution until the onset of non–linearities on the relevant scales. In fact, tracker solutions, in the expansion regime dominated by relativistic matter, set the initial conditions, both for the background components and for density inhomogeneities outside the particle horizon.

In this thesis we shall not debate linear codes, in any detail. It must be however outlined that CMB analysis and simulations of DDE could be started only thanks to the availability of linear algorithms, developed within the cosmology group of the Milano–Bicocca University, based on generalizations either of the public programs like CMBFAST or CAMBS, which had been in use here since many years, to work out linear transfer functions.

Chapter 2

CMB properties

Testing DE theories against CMB data could appear a sinple task, owing to the linearity of equations involved. However the effect of varying DE state equation interfere with changes in other parameters, while the actual sensivity of realistic observational apparati is also to be taken into account.

In this chapter we shall therefore debate all the scheme leading to predictions of CMB anisotropy and polarization. This is strictly necessary to focus the role that DE state equation has in shaping real data.

2.1 Description of the radiation field

The properties of an electromagnetic wave, propagating in a direction $\vec{k}$, can be conveniently described by a rank 2 symmetric tensor, $I_{ab}(\vec{k})$. Labeling E_i the components of the wave's electric field vector with respect to an orthonormal basis $(\vec{e}_1, \vec{e}_2)$ in the plane perpendicular to $\vec{k}$, such tensor reads:

$$I_{ab}(\vec{k}) = \frac{\langle E_a E_b \rangle}{4\pi c}. \tag{2.1}$$

The total intensity of the radiation along the direction $\vec{k}$ is then the tensor trace

$$I(\vec{k}) = I_{11}(\vec{k}) + I_{22}(\vec{k}). \tag{2.2}$$

Averaging over all possible directions $\vec{k}$, we obtain the *average* radiation intensity $\bar{I}$, which is related to the thermodynamic temperature by the usual relation $\bar{I} = \sigma T^4$ (in units yielding $c = \hbar = 1$, it is $\sigma = \pi^2/15$). However, much cosmological information enclosed in the CMB radiation is conveyed by the field's temperature and polarization *fluctuations*. It is then convenient to replace I_{ab} with the dimensionless tensor $\Delta_{ab} = I_{ab}/\bar{I} - \delta_{ab}/2$. Its components are directly related to the temperature anisotropies and the Stokes parameters accounting

for linear polarization as follows:

$$\hat{T} = (\Delta_{11} + \Delta_{22})/4 \ , \ Q = \Delta_{11} - \Delta_{22} \ , \ U = \Delta_{12}/2. \tag{2.3}$$

The fourth Stokes parameter V, accounts for circular polarization. The main source of CMB polarization is Thomson scattering of photons on free electrons, during recombination and reionization, which does not induce circular polarization. Therefore, V will not be considered here.

While temperature anisotropies $\hat{T}$ are a scalar field, the values of Q and U clearly depend on the choice of the basis $(\vec{e}_1,\vec{e}_2)$ and change under rotations of the reference system. In particular, if the basis is rotated by an angle ψ, so that

$$\vec{e}_1' = \cos\psi \ \vec{e}_1 + \sin\psi \ \vec{e}_2, \quad \vec{e}_2' = -\sin\psi \ \vec{e}_1 + \cos\psi \ \vec{e}_2 \ , \tag{2.4}$$

the Stokes parameters transform as

$$Q' = \cos 2\psi \ Q + \sin 2\psi \ U, \quad U' = -\sin 2\psi \ Q + \cos 2\psi \ U. \tag{2.5}$$

Accordingly, $Q \pm iU$ are spin–2 fields.

It is then convenient to define a 3–component quantity

$$\mathbf{D} \equiv (\hat{T}, Q, U) \tag{2.6}$$

which, under rotation of the basis' vectors by an angle ψ, transforms into

$$\mathbf{D}' = \mathbf{R}(\psi)\mathbf{D} \ , \tag{2.7}$$

where the unitary rotation matrix $\mathbf{R}$ reads:

$$\mathbf{R}(\psi) = \begin{pmatrix} 1 & 0 & 0 \\ 0 & \cos 2\psi & \sin 2\psi \\ 0 & -\sin 2\psi & \cos 2\psi \end{pmatrix} \tag{2.8}$$

2.2 The CMB angular power spectra

When we observe the CMB, we see it projected on the celestial sphere. It is then clear that the observed values of $\hat{T}$, Q and U are functions of the sky direction $\vec{n}$ (notice that $\vec{n} = -\vec{k}$). Accordingly, we can expand $\hat{T}$ using spherical harmonic functions, Y_{lm}, which form an orthonormal basis for differentiable functions on the sphere. The temperature anisotropy in the direction $\vec{n}$ then reads:

$$\hat{T}(\vec{n}) = \sum_{l=2}^{\infty} \sum_{m=-l}^{m=+l} a_{T,lm} Y_{lm}(\vec{n}) \ . \tag{2.9}$$

This expansion neatly separates the relevant cosmological information, enclosed in the coefficients $a_{T,lm}$, from purely geometrical effects, expressed by Y_{lm}. Coefficients with index l are related to features on angular scales $\alpha \sim \pi/l$, while m refers to the azimuthal orientation of such features. At each l, there are $2l+1$ independent orientations m. Notice that the expansion includes contributions only by the quadrupole and higher moments, as the monopole vanishes by construction and the dipole component is dominated by the Doppler shift due to observer's motion with respect the CMB frame.

An analogous expansion for polarization must take into account the behaviour of Q and U under rotations of the vectors $(\vec{e}_1, \vec{e}_2)$. Here we shall follow the approach by Seljak & Zaldarriaga (Seljak and Zaldarriaga 1996, Seljak and Zaldarriaga 1997). An alternative approach by Kamionkowski, Kosowsky & Stebbins (Kamionkowski, Kosowsky and Stebbins). The two formalisms are equivalent, apart for slight differences in normalization. Consider then the linear combinations $Q \pm iU$ which are quantities of spin ± 2 (Goldberg et al., 1967) and, under rotations of the reference system by ψ, simply change by a phase:

$$(Q \pm iU)' = e^{\pm 2i\psi} (Q \pm iU) \tag{2.10}$$

An orthonormal basis on the sphere for functions of definite spin s, is provided by the *spin-weighted spherical harmonics* ${}_sY_{lm}$, which can be obtained by applying suitable operators, called spin raising or lowering operators, to ordinary spherical harmonics. The resulting expansions read:

$$\begin{array}{rcl} (Q+iU)(\vec{n}) & = & \sum_{lm} a_{+2,lm}\, {}_{+2}Y_{lm}(\vec{n}) \\ (Q-iU)(\vec{n}) & = & \sum_{lm} a_{-2,lm}\, {}_{-2}Y_{lm}(\vec{n}). \end{array} \tag{2.11}$$

We can then introduce two new scalar quantities E and B, defined through their expansion coefficients:

$$\begin{array}{rcl} a_{E,lm} & = & -\left(a_{2,lm} + a_{-2,lm}\right)/2 \\ a_{B,lm} & = & -\left(a_{-2,lm} + a_{2,lm}\right)/2i. \end{array} \tag{2.12}$$

Being defined in harmonic space, the E and B fields are nonlocal and, in principle, in order to know them in one direction, measurements are required over all the celestial sphere. If data cover it partially, the decomposition of CMB polarization into E and B is not unique (Bunn 2002, Bunn 2003, Turok 2002). In this case a third, *ambiguous* mode must be added, in order to avoid leakages between E and B modes.

Besides the advantage of being scalar quantities, E and B allow to relate CMB polarization to its physical origin, thanks to their different behaviour

under parity transforms: while E remains unchanged, B changes sign, in analogy with electric and magnetic field. For this reason, they are often called *electric* and *magnetic* modes. As we will outline in Sec. 2.6, this different behaviour has several important consequences.

The set of expansions coefficients $\{a_{T,lm}, a_{E,lm}, a_{B,lm}\}$ completely describes the CMB field. If the field is Gaussian, their phases are completely random and the mean of each multipole vanishes, $\langle a_{T,lm}\rangle = \langle a_{E,lm}\rangle = \langle a_{B,lm}\rangle = 0$. All physical information is then enclosed in four angular power spectra (APS):

$$\begin{aligned}
\langle a^*_{T,lm} a_{T,l'm'}\rangle &= C_{Tl}\,\delta_{l,l'}\,\delta_{m,m'} \\
\langle a^*_{E,lm} a_{E,l'm'}\rangle &= C_{El}\,\delta_{l,l'}\,\delta_{m,m'} \\
\langle a^*_{B,lm} a_{B,l'm'}\rangle &= C_{Bl}\,\delta_{l,l'}\,\delta_{m,m'} \\
\langle a^*_{T,lm} a_{E,l'm'}\rangle &= C_{TE,l}\,\delta_{l,l'}\,\delta_{m,m'}.
\end{aligned} \tag{2.13}$$

The power spectra for the cross-correlations between B and $\hat{T}$ or E vanish due to their different behaviour under parity transforms.

The brackets at the l.h.s of eq. 2.13 prescribe an averaging operation which, in principle, is an ensemble average. However, we are given only a single realization of the CMB sky. When applying the above definition to real data, eq. 2.13 translates into:

$$\tilde{C}_{Tl} = \frac{1}{2l+1}\sum_{m=-l}^{+l} |a_{T,lm}|^2 \tag{2.14}$$

with similar relations holding for the other APS. Under ideal conditions, these are the minimum variance estimators of CMB APS, with associated errors:

$$\Delta\tilde{C}_{Tl} = \sqrt{\frac{2}{2l+1}}\tilde{C}_{Tl}. \tag{2.15}$$

Expression 2.15 yields the upper limit on the precision with which a CMB multipole can be directly known by a single observer, due to Cosmic Variance (CV). This variance can be particularly limiting at low multipoles; for instance, CV implies a relative uncertainty on the quadrupole $\sim 65\%$. However, these are not absolute limits, and several suggestions for bypassing CV have been proposed (Kamionkowski and Loeb 1997, Seto and Sasaki 2000) These methods aim to probe the quadrupole as seen by high-z clusters, which can be considered as the quadrupole associated to a different realization of the cosmological model.

2.2.1 The tensor harmonic expansion

An alternative description of CMB polarization has been given by Kamionkowski, Kosowsky & Stebbins, and makes use of tensor instead of spin-weighted harmonics. Indicating with θ the azimuthal angle corresponding to

the direction $\vec{n}$, the trace–free part of the tensor Δ_{ab} can be rewritten as:

$$P_{ab}(\vec{n}) = \frac{1}{2}\begin{pmatrix} Q(\vec{n}) & -U(\vec{n})\sin\theta \\ -U(\vec{n})\sin\theta & -Q(\vec{n})\sin^2\theta \end{pmatrix}. \tag{2.16}$$

An appropriate basis for the expansion of this tensor is obtained through linear combination of covariant derivatives of spherical harmonics. Let us define the functions:

$$\begin{aligned} Y^{G}_{(lm)ab} &= N_l\left(Y_{(lm);ab} - \tfrac{1}{2}g_{ab}Y_{(lm);c}{}^{c}\right) \\ Y^{C}_{(lm)ab} &= \tfrac{N_l}{2}\left(Y_{(lm);ac}\epsilon^{c}{}_{b} + Y_{(lm);bc}\epsilon^{c}{}_{a}\right), \end{aligned} \tag{2.17}$$

where g_{ab} is the metric tensor on the sphere, ϵ_{ab} is the completely antisymmetric rank 2 tensor and $N_l = [2(l-2)!/(l+2)!]^{1/2}$. We can then write

$$P_{ab} = \sum_{lm}\left[a^{G}_{(lm)}Y^{G}_{(lm)ab}(\vec{n}) + a^{C}_{(lm)}Y^{C}_{(lm)ab}(\vec{n})\right]. \tag{2.18}$$

This expression is the extension to spherical geometry of the decompositon of a vector field as the sum of the gradient of a scalar field and of the curl of a vector field (then, the notation G for "gradient" and C for "curl"). In principle, this approach can be generalized to an arbitrary geometry once the expression of the relevant metric tensor g_{ab} is known.

If the linear polarization field is visualized with headless "vectors" representing the amplitude and orientation of the polarization, then the C and G harmonics respectively describe the component of the polarization field which does or does not have an associated handedness.

Finally, from the multipole components $a^{G}_{(lm)}$ and $a^{C}_{(lm)}$, one obtains the corresponding APS, in the same way of eqs. 2.13. It is possible to verify that the resulting multipole G and C components are equivalent to E and B modes, respectively (except for a factor $\sqrt{2}$ in the amplitude). Polarization patterns associated with G and C (or E and B) modes are shown in Fig. 2.1. In the following we choose utilize the Seljak & Zaldarriaga's formalism.

2.3 Correlation functions on the Celestial Sphere

As the power spectrum of a distribution in euclidean space is the Fourier transform of the distribution's two–points correlation function, so the APS defined in the previous section are related to the two–points correlation functions of $\hat{T}$, Q and U through appropriate spherical transforms.

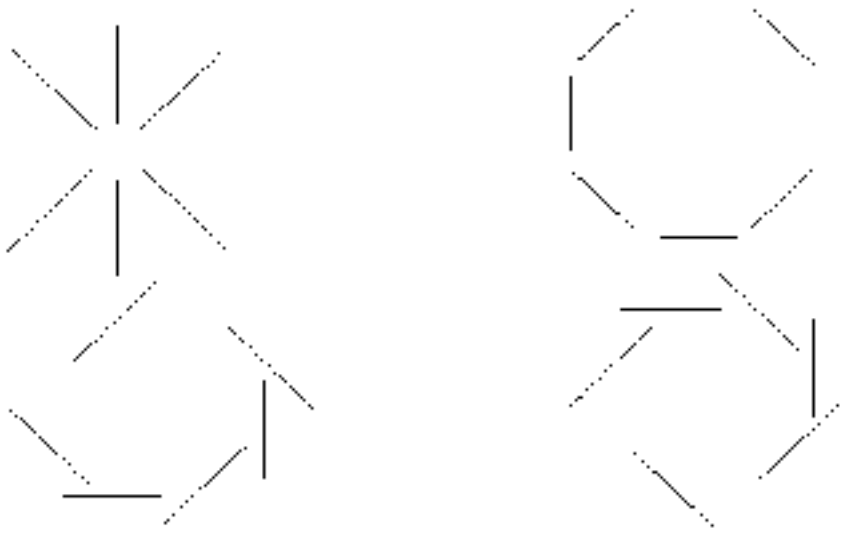

Figure 2.1: Polarization patterns without (top) or with (bottom) associated handedness. Top patterns correspond to pure E–mode (G–mode) polarization, while bottom ones are associated with pure B–mode (C–mode).

We start by rewriting eq. 2.9 and 2.11 as:

$$\begin{aligned}
\hat{T}(\vec{n}) &= \sum_{lm} a_{T,lm} Y_{lm}(\vec{n}), \\
Q(\vec{n}) &= -\sum_{lm} \left[a_{E,lm} X_{1,lm}(\vec{n}) + i a_{B,lm} X_{2,lm}(\vec{n}) \right], \\
U(\vec{n}) &= -\sum_{lm} \left[a_{B,lm} X_{1,lm}(\vec{n}) - i a_{E,lm} X_{2,lm}(\vec{n}) \right],
\end{aligned} \tag{2.19}$$

where we have introduced the auxiliary functions $X_{1,lm}(\theta,\phi) \equiv ({}_2Y_{lm}(\theta,\phi) + {}_{-2}Y_{lm}(\theta,\phi))/2 = F_{1,lm}(\theta)\, e^{im\phi}$, $X_{2,lm}(\theta,\phi) \equiv ({}_2Y_{lm}(\theta,\phi) - {}_{-2}Y_{lm}(\theta,\phi))/2 = F_{2,lm}(\theta)\, e^{im\phi}$; θ and ϕ are the angles corresponding to direction $\vec{n}$ and $F_{1-2,lm}$ are defined in terms of associated Legendre functions.

Simple but lengthy calculations allow to evaluate the expected correlation between temperature signals measured in the directions 1 and 2:

$$\langle \hat{T}(1)\ \hat{T}(2) \rangle = \sum_l \frac{2l+1}{4\pi} C_{Tl} P_l(\cos\alpha_{12}) \tag{2.20}$$

α_{12} is the angle between the directions 1 and 2 and P_l are ordinary Legendre polynomials. Again, brackets on l.h.s. of eq. 2.20 prescribe an ensemble average. When applying this definition to real data, the average is taken on all pairs of sky directions with angular separation α_{12}. This can be critical at large angular scales (i.e. low multipoles), at which there are relatively few pairs of independent directions.

Evaluating the corresponding expressions for Stokes' Q and U is simpler in a reference system in which the basis vector $\vec{e}_1$ is aligned with the great circle connecting directions 1 and 2. There they read

$$\begin{aligned}
\langle Q(1)Q(2)\rangle &= \sum_l \frac{2l+1}{4\pi}[C_{El}F_{1,l2}(\alpha_{12}) - C_{Bl}F_{2,l2}(\alpha_{12})] \\
\langle U(1)U(2)\rangle &= \sum_l \frac{2l+1}{4\pi}[C_{Bl}F_{1,l2}(\alpha_{12}) - C_{El}F_{2,l2}(\alpha_{12})] \\
\langle \hat{T}(1)Q(2)\rangle &= -\sum_l \frac{2l+1}{4\pi} C_{TEl}F_{1,l0}(\alpha_{12}) \\
\langle \hat{T}(1)U(2)\rangle &= 0. \qquad (2.21)
\end{aligned}$$

Together with eq. 2.20, such relations form the components of the $3 \otimes 3$ matrix $\langle \mathbf{D}^T(i)\mathbf{D}(j)\rangle$, where $\mathbf{D}(i)$ is defined in eq. 2.6 and evaluated along direction i. Corresponding expressions in a generic basis are more complicated; they can be obtained from those in the preferred frame using eq. 2.7. We obtain:

$$\langle \mathbf{D}'^T(i)\mathbf{D}'(j)\rangle = \mathbf{R}^T(\psi_i)\langle \mathbf{D}^T(i)\mathbf{D}(j)\rangle \mathbf{R}(\psi_j) \qquad (2.22)$$

with $\mathbf{R}(\psi)$ defined in eq. 2.8 while $\psi_{i,j}$ are the angles by which we need to rotate, along the line of sight, the reference frames at the points i and j, respectively. As we are considering a spherical geometry ψ_i and ψ_j can be different. Making use of these transformations, we can pass from the privileged basis, where eqs. 2.21 hold, to the generic basis needed for observational or modellization aims.

2.4 Comparison with real data and parameter extraction

For Gaussian fields, the APS and the two–point correlation functions completely define the statistical properties of the pure CMB anisotropies and polarization fields, in multipole and position space respectively. The comparison of predictions with real data, however, involves additional complications. The microwave signal is observed through a finite resolution antenna, and the resulting measurements are collected into sky maps with pixels of finite size. Moreover, the signal in each pixel of an actual sky map sums up the CMB contribution and different kinds of foreground and instrumental noises.

Both antenna resolution and pixelization effects are expressed through a convolution of the actual signal with appropriate window functions; in harmonic space this translates into an effective reduction of the power at each multipole. The measured APS then become

$$C_{X,l}^{meas} = C_{X,l}|_s W_l|^2 \qquad (2.23)$$

$(Y = \hat{T}, E, B, TE)$ with

$$ {}_sW_l = b_{pix,l}\, {}_sB_l \tag{2.24} $$

where $b_{pix,l}$ is the decomposition of the pixel window function onto the appropriate spherical harmonic basis (ordinary or spin-weighted), and ${}_sB_l$ is the transformed beam window function. In the ideal case of a purely Gaussian beam, this writes

$$ {}_sB_l = \exp[-(l(l+1) - s^2)\sigma^2/2], \tag{2.25} $$

where $\sigma = \mathrm{FWHM}/\sqrt{8\ln 2}$ and $s = 0$ ($s = 2$) for anisotropy (polarization) (Ng 1999). The rms polarization $P_{\rm rms}$ measured over a finite–resolution map is then given by

$$ P^2_{\rm rms} = \sum_{l \geq 2} \frac{2l+1}{4\pi} C_{Pl}\, {}_2W_l^2, \tag{2.26} $$

where

$$ C_{Pl} = C_{El} + C_{Bl}. \tag{2.27} $$

If Q and U maps are both available, the relation $P^2_{\rm rms} = Q^2_{\rm rms} + U^2_{\rm rms}$ can be used instead.

As an example, for an instrument with a FWHM aperture of 7°, the reduction on polarization spectra due to beam smoothing is e^2 for $l \simeq 27$. It is then clear why, with such angular resolution, it does not make sense to explore spherical harmonics above $l = 30$. Let us also recall that an optimal exploitation of the signal is achieved using pixels with centers at a distance $\sim$ FWHM/2.

The temperature anisotropy in the i–th pixel can then be decomposed as

$$ \hat{T}_i = \sum_{lm} \left({}_sW_l a_{Tlm} + a^{noise}_{Tlm} \right) Y_{lm}(\vec{n}_i) \tag{2.28} $$

where the *effective* noise term includes the contribution from instrumental noise as well as the residual power from all non–CMB components, e.g. foreground contaminations. We assume here that CMB is not correlated with any other component:

$$ \langle a_{Tlm}\, a^{noise}_{T'l'm'} \rangle = 0. \tag{2.29} $$

Similar expressions hold for polarization multipoles.

In order to compare data with predictions, it is convenient to order measurements in a vector $\mathbf{x} = \{\hat{T}_1, ..., \hat{T}_{N_T}, Q_1, ..., Q_{N_P}, U_1, ..., U_{N_P}\}$, where N_T and N_P are the number of pixels with temperature and polarization measurements. Notice that N_T and N_P can be different, as data may cover different portions of the sky, either because different sky cuts are applied to the $\hat{T}$ and Q, U maps

(e.g., the foreground removal efficiency can be different) or because they come from different experiments.

The correlation matrix $\langle \mathrm{x}_i^T \mathrm{x}_j \rangle \equiv \mathbf{C}_{ij} = \mathbf{S}_{ij} + \mathbf{N}_{ij}$ expresses then the expected statistical properties of the vector x for a given cosmological model $\mathcal{M}$. It has been written as the sum of a CMB signal term, $\mathbf{S}_{ij}$ which depends on cosmology and geometry, and a term accounting for the statistical properties of the effective noise. $\mathbf{S}_{ij}$ can be evaluated using relations as those of eqs. 2.20 and 2.23, while, if the only contribution to effective noise is provided by an uniform white noise, $\mathbf{N}_{ij}$ is a diagonal matrix.

The likelihood that the measurements x corresponds to the cosmological model $\mathcal{M}$ is then

$$\mathcal{L}(\mathcal{M}|\mathrm{x}) = \frac{1}{(2\pi)^{N_T/2+N_P}} \frac{1}{\sqrt{\det \mathbf{C}}} \exp\left(-\frac{1}{2}\mathrm{x}^T \mathbf{C}^{-1} \mathrm{x}\right) . \qquad (2.30)$$

In a Bayesian analysis, the posterior probability density function (p.d.f.) for the set of parameters specifying $\mathcal{M}$ is the product of the likelihood function and the prior p.d.f. In the case of uniform priors, the most probable model is simply the one maximizing the likelihood function.

In experiments sensitive only to large angles, CV can pose a serious problem, and a given model can yield significantly different skies. When evaluating the expected performance and capabilities of such experiments, as is done in this thesis, average results can be misleading. It is then convenient to adopt a frequentist approach, by generating a large number of synthetic skies and analyzing them as real data. The posterior p.d.f is then simply given by the relative frequencies of the parameters recovered.

Let us finally point out that, as we are here concerned with large angular scales, the number of pixels involved is comparatively low and working in pixel instead of multipoles space is not numerically expensive. Moreover, this approach has the added benefit of simplifying joint likelihoods for temperature and polarization data coming from different experiments.

2.5 Time Evolution of Energy Density Fluctuations

In this section we briefly describe the physical processes responsible for the birth and evolution of CMB temperature and polarization anisotropies, outlining how several cosmological parameters affect the APS introduced in the previous sections. As most features become imprinted in CMB at the epoch of Last Scattering, the linear theory of fluctuation evolutions provides a very accurate framework for working out the CMB APS, and forms the core of the so-called

precision cosmology. This is not only due to advances in instrumental and experimental conditions, but also to the high capacity of theory to meet them.

Several authors have accurately studied the problem of setting initial conditions in cosmology and the expressions of the dynamical equations governing the evolution of perturbations. Here we shall mostly describe the key procedures and results of such analysis, and refer to the comprehensive work by Ma & Bertschinger (Ma and Bertschinger 1995) for analytical details.

It is convenient to start the analysis of fluctuations' evolution at a time t_i earlier than matter–radiation equivalence, which occurs at a redshift $z_{eq} \simeq 2.6 \cdot 10^4 \Omega_m h^2$, and selected in order that all scales of interest are still outside the cosmological horizon.

To first order, perturbations in the metric tensor arise either from primordial density fluctuations or from gravity waves (GW) generated during Inflation. Density fluctuations involve all components of the cosmological fluid (radiation, baryons, dark matter and, possibly, dark energy) and produce only scalar perturbations, as they are invariant under parity transform. Density perturbations are typically expressed in term of their power spectrum, $P(k)$ (i.e. the Fourier transform of the field two–points correlation function), often assumed to follow a power law, $P(k) = Ak_s^n$. Generic inflationary model predict a scalar spectral index $n_s \sim 1$; if $n_s = 1$ (Zel'dovich spectrum) fluctuations at horizon entry display the same average amplitude on all scales.

If $n_s < 1$, generic Inflation models predict a background of GW, with a power spectrum (Knox and Turner 1996, Dodelson at al. 1994)

$$P_t(k) = rA\,k^{n_T} \quad \text{with} \quad n_T = n_s - 1 \text{ and } r = 7(1 - n_s) \tag{2.31}$$

which have a tensor nature and are then responsible for pseudoscalar features in the CMB APS.

The sequel of events that shape the observed APS are then the following ones:

(1) – Entry into the horizon and passage from radiation dominated to matter dominated expansion.

(2) – Gradual passage from the tight–coupling regime to photon free streaming, during the primeval hydrogen recombination.

(3) – Reionization at low–z ($\sim$ 5–25) and cosmic opacity to CMB photons.

(4) – Late deviations from matter dominated expansion, when Dark Energy (DE) becomes first sub–dominant and then eventually drives the expansion.

Here we shall briefly comment on the first two points, deferring a more accu-

rate discussion of the impact of reionization and dark energy to later chapters.

Until recombination, photons and the electron–baryons component form a tightly coupled fluid on all scales of cosmological relevance. In fact, electric charge accumulation would require high amounts of energy and thus never occurs. Electron and baryons therefore move together as though they were bound in atoms. Photons could in principle follow a different distribution, however the strong electromagnetic coupling implies that the photon mean free path is well below all scales of cosmological interest. In the first stages of Universe evolution, then, the dynamical state of the baryon–electron–photon plasma is completely defined by its density (fluctuation) and velocity fields.

Outside horizon, no causal relation is possible and perturbation modes in the Newtonian gauge are frozen. Once a relevant scale enters the horizon, fluctuations start evolving and compression waves can form. The number of compressions and rarefaction phases experienced by a given perturbation is set by the time elapsing from the moment of horizon entering, and hence the mass scale of the fluctuation, and recombination. A mass scale of $\sim 10^{15} M_{\odot}$ enters the horizon around recombination and will be in a state of maximum compression, oscillations on scales $\lesssim 10^{12} M_{\odot}$, instead die out before recombination.

At recombination, the photon energy is no longer enough to keep electrons and protons from bounding into hydrogen atoms. The number of free charged particles drops rapidly and in a narrow redshift interval around $z_{rec} \sim 1100$ the Universe becomes transparent to electromagnetic radiation.

As the coupling fades, a set of higher order multipoles gradually switch on in the photons distribution and power is transferred from low l's to higher ones. This expresses, in the momentum space, the gradual free–streaming of photons from initial fluctuations. Most of the features observed in present APS have then been imprinted at the Last Scattering Band, when more of 95% of the CMB photons had their last interaction with matter.

2.5.1 Physical effects in the last scattering band

Evolution of CMB perturbations can be followed accurately only through numerical integration[1], however a qualitative understanding of the characteristic

[1]Solving the full set of Boltzmann equations governing the photons' distribution, up to $z = 0$ is quite expensive in terms of computational resources. An alternative approach consists in integrating the Boltzmann equations along the line of sight (Seljak and Zaldarriaga 1996). The resulting expressions for APS depend on a source term and a geometrical term. The former takes into account contributions from relatively few multipoles, which need to be calculated exactly through Boltzmann equations, the latter does not depend on cosmology and can be evaluated once and then stored for subsequent evaluations. The line–of–sight approach forms

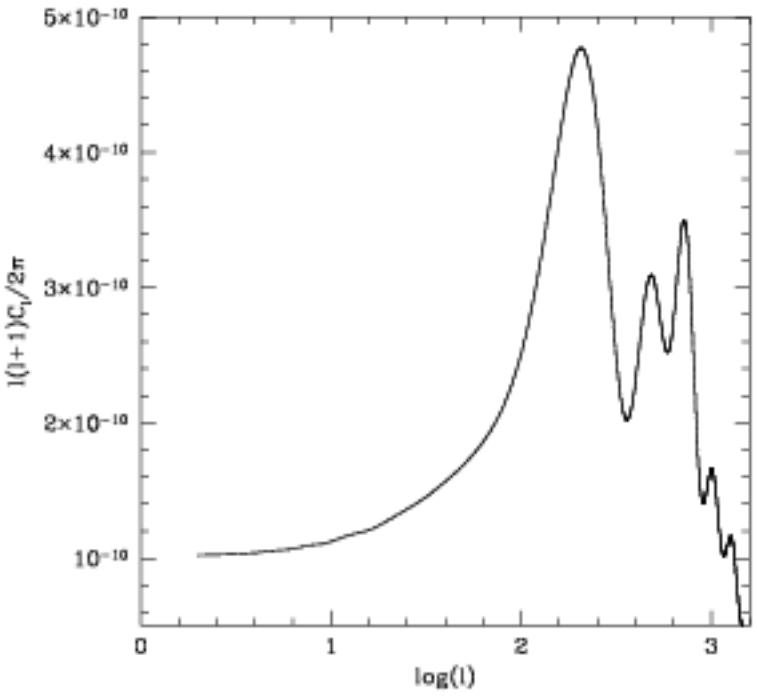

Figure 2.2: Anisotropy spectrum in a SCDM model

features of the APS is possible. In Fig. 2.2 the C_{Tl} spectrum, for the Standard Cold Dark Matter (SCDM) model is plotted. In this model, critical density is achieved by adding to ordinary matter quite a large component made by non–relativistic particles. This model is considered unlikely in the light of recent data, however it provides a useful reference to outline the physical effects occurring in the last scattering band.

The SCDM spectra clearly shows an almost flat region at low multipoles, followed by alternated peaks and deeps, that are related to the presence of compression waves in the baryons–radiation plasma, until recombination. At $l > 1000$, the spectrum starts to fade. All these features can be reconduced to three main effects affecting the photons' distribution at recombination:

(1) – *The Sachs & Wolfe effect* (Sachs and Wolfe 1967). On scales larger than the horizon at recombination, density fluctuations trace the gravitational potential ψ, as they had not yet entered an oscillatory regime. At decoupling photons are no longer tied to the matter distribution; as they climb out from potential wells, photons suffer the effects of a gravitational redshift and time dilation. The net results are temperature fluctuations $\hat{T} \propto \psi$, whose variance is seen as C_{Tl} over very large scales. Additional anisotropies can also arise

the core of most modern codes. Among them we mention here the CMBFAST code by Seljak & Zaldarriaga (Seljak and Zaldarriaga 1996)

along the photon's path, if the time derivative of the metric is non–vanishing. This effect, called *Integrated Sachs & Wolfe* (ISW), can be due to GW or time evolution of the gravity potential, and is therefore expected to play a key role in models with DE.

(2) – *Radiation concentration or rarefaction.* Fluctuations on scales entering the horizon before recombination begin oscillating as acoustic waves. Waves reaching the LSS in an antinode state correspond to fluctuations δ undergoing a state of maximum compression or rarefaction and with vanishing velocity. The CMB temperature fluctuation for scales attaining recombination with a antinode is, therefore, $\hat{T} = Tr(\Delta_{ab}) = \delta/4$.

(3) – *Doppler shifts.* Compression waves attaining recombination in a node phase corresponds to fluctuations of vanishing amplitude but with maximum velocity, $|\vec{v}| = \delta$. While δ is a scalar quantity, $\vec{v}$ is a vector and its contribution to CMB spectra arise because of its component along the line of sight, which, in average is $v/\sqrt{3}$. Accordingly, the observed temperature fluctuation $\hat{T}$, on scales attaining recombination in this state, is lower than on scales attaining recombination with an antinode.

These effects are clearly visible in the features of the APS displayed in Fig. 2.2. The plateau extending up to $l \sim 100$ is a consequence of the Sachs & Wolfe effect, which predicts $l(l+1)C_l = const$ for $P(k) \propto k$. The $\hat{T}$ peak at $l \simeq 200$ denotes the largest scale undergoing compression exactly at recombination. This is clearly the scale which is just entering the horizon. The position of the first peak in l space, is then fixed by the angle under which the Hubble radius at recombination is seen by an observer at $z = 0$. The following peaks correspond to waves attaining recombination with an antinode phase. In absence of Doppler effects, power between subsequent peaks would vanish, in correspondence of waves reaching the LSS in a node state. Doppler effects are then mainly responsible for filling the gaps between peaks, and the habit of dubbing the first acoustic peak, *Doppler* peak is misleading.

The alternating heights of the peaks also has a simple qualitative explanation. As already stated, when a scale enters the horizon, baryonic matter and radiation begin oscillating. DM fluctuations, not being subjected to photon drag, are instead free to continue growing. The growing potential well due to DM sets the zero–point for the sonic oscillations in the photon-baryon plasma. Peaks corresponding to oscillations in phase with DM fluctuations (first and third in the Fig shown) will then be higher than peaks for oscillations in phase opposition with DM.

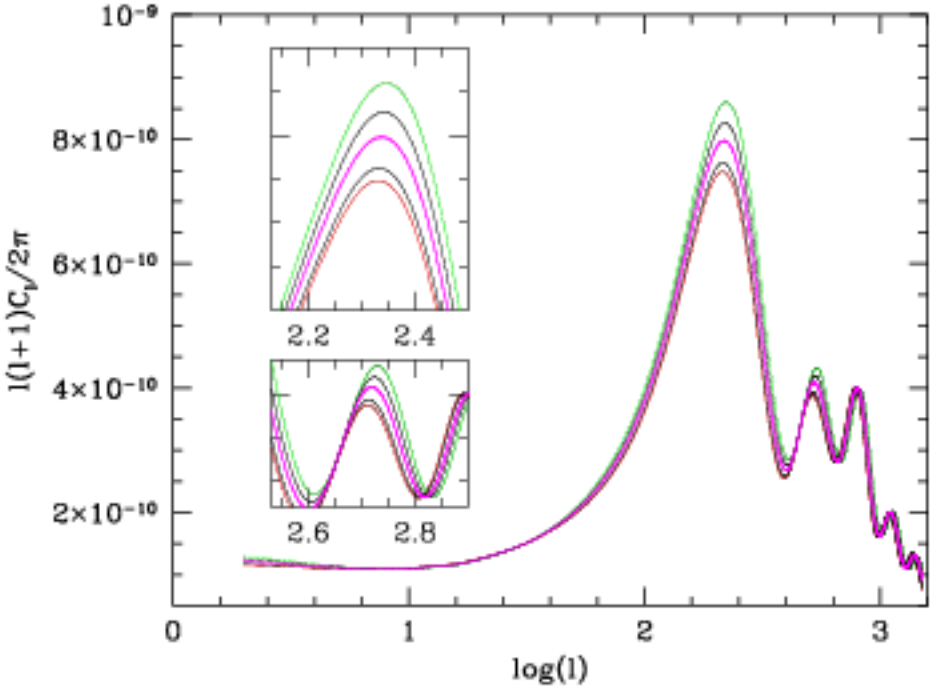

Figure 2.3: Dependence of C_{Tl} spectrum on $\Omega_m h^2$. The magenta curve corresponds to $\Omega_m = 0.3$, $h = 0.7$. Curves above (below) it yield lower (higher) density models; the top green (bottom red) curve is for $\Omega_m h^2 = 0.25$ (0.35). We took $T_o = 2.73$, $N_\nu = 3$, $\Omega_b = 0.04$. In the small boxes, features around the *Doppler* peak and the successive peak are magnified. Notice that the green (red) curve is the top (bottom) one in both plots.

Finally, on scales smaller than the width of the LSS fluctuations are smoothed out due to the high optical depth to Thomson scattering during recombination. For a LSS width of $\Delta z \simeq 40$, this results in drastic erase of features on angular scales smaller than of $\simeq 20$ arcmin and is shown by the APS' amplitude decrease after the third peak.

2.5.2 Constraints from primary T−anisotropy data

The qualitative discussion in the previous section outlined the main physical processes responsible for the *primary anisotropies* observed in the microwave sky. In turn, these processes depend on several cosmological parameters and variation of such parameters affects the CMB spectra in a precise (and predictable) way. In this section we show how some of this parameters alter features in APS for models more realistic than the simple SCDM. Most of these effects were first ordered by Hu and Sugiyama (Hu and Sugiyama 1996).

For purely adiabatic perturbations, power-law initial conditions are deter-

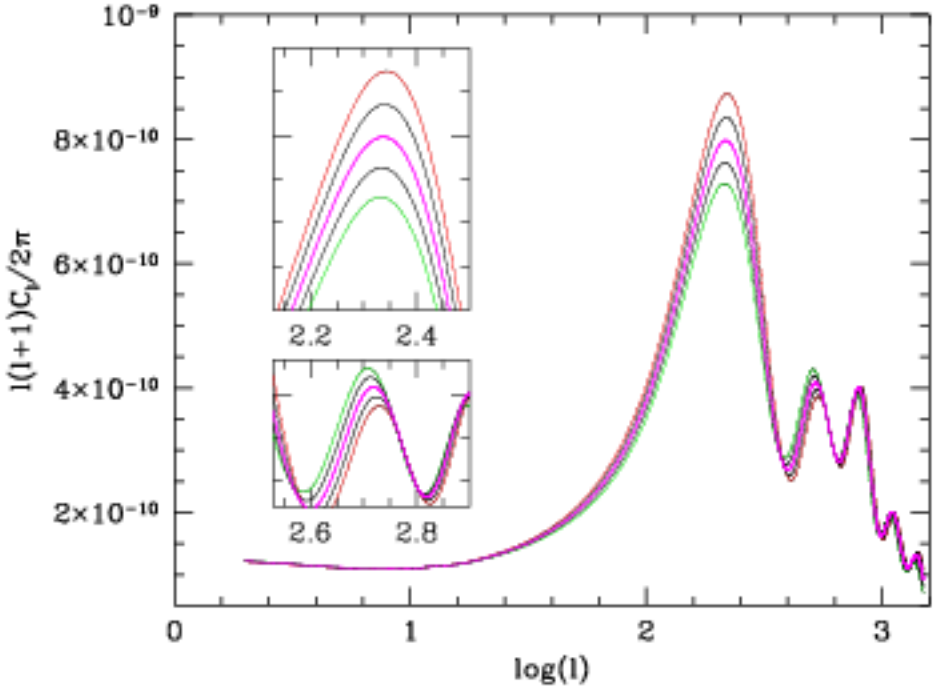

Figure 2.4: Dependence of $C_{T,l}$ spectrum on $\Omega_b h^2$. The magenta curve corresponds to $\Omega_b = 0.04$, $h = 0.7$. Curves above (below) it yield lower (higher) density models; the green (red) curve is for $\Omega_b h^2 = 0.0147(0.0245)$. We took $T_o = 2.73$, $N_\nu = 3$, $\Omega_m = 0.3$. In the small boxes, features around the *Doppler* peak and the successive peak are magnified. Notice that the green (red) curve is the top (bottom) one for the *Doppler* peak and the bottom (top) one for the successive peak: $\Omega_b h^2$ controls the ratio between the heights of the first two peaks .

mined completely by four parameters A, n_s, r, and n_T. The first two parameters enter into the definition of the primeval fluctuation spectrum $P(k)$, the latter two in the definition of the spectrum of GW's. Within the context of single–field Inflation, the consistency relation 2.31 implies that GW's parameters are univocally fixed by the scalar fluctuations' tilt and amplitude. Departures from power law behaviour or an admixture of isocurvature initial conditions would require additional parameters (Bucher et al.).

The evolution of perturbations from these initial state until decoupling involves a set of *physical* parameters, which are specific combinations of standard cosmological parameters.

(i) Relativistic particles at recombination include photons and massless neutrinos. The energy density of radiation is fixed by the current microwave background temperature T_o, while that of the neutrino backgrounds depends on the effective number of massless neutrino species N_ν.

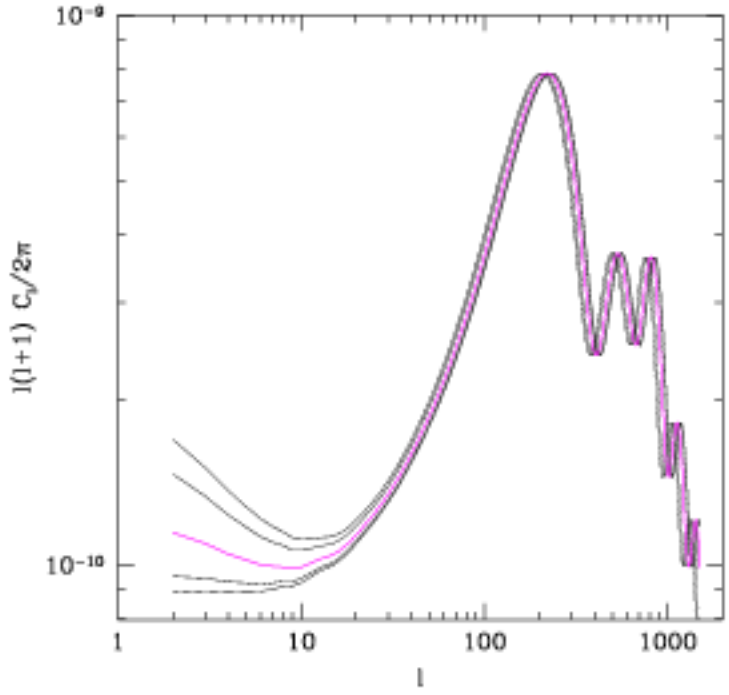

Figure 2.5: Dependence of $C_{T,l}$ spectrum on $\Omega_m h$. The magenta curve corresponds to $\Omega_m = 0.3$, $h = 0.7$. Curves above (below) correspond to lower (higher) density models. Normalization was set so to have equal height for *Doppler* peaks. This shows the gradual displacement to the right of the peaks as $\Omega_m h$ increases.

(ii) The magnitude of the Sachs-Wolfe effect depends on the gravitational potentials describing scalar perturbations, which in turn depend on $\Omega_m h^2$, the fraction of critical density as nonrelativistic matter. The gravitational potentials also appear as a forcing term in the oscillator equation describing the acoustic waves in the plasma.

(iii) The baryon density, $\Omega_b h^2$, alters the effective mass in the oscillator equation and reduce sound speed in the plasma (with a slight extra dependence on N_ν). Together this effects lead to an enhancement of the amplitude of oscillations, and a displacement of the equilibrium point, thus breaking the symmetry of oscillations.

(iv) The redshift z_{eq} is then determined by the $\Omega_m h^2$, which in turn affects the size of DM fluctuations, since they start to grow gravitationally only after z_{eq}. Also, the gravitational potentials evolve in time at $z > z_{eq}$ and cease to do so afterward. Hence, the later z_{eq} occurs, the greater the time evolution of the potentials at decoupling, increasing the Integrated Sachs-Wolfe effect.

(v) The horizon size at recombination, which sets the overall scale of the acoustic

oscillations and, in particular, the position of the Doppler peak, depends only on the total mass density $\Omega_m h$.

(vii) The scale for diffusion damping depends on the baryon density $\Omega_b h^2$ with a slight extra dependence directly on Ω_b alone.

In summary, the $\hat{T}$ spectrum at last scattering is shaped by the physical parameters $\Omega_m h^2$, $\Omega_b h^2$, $\Omega_m h$, instead by the individual cosmological parameters Ω_m, Ω_b, h. The quality of present data sets allow to constrain several parameters simultaneously. Accurate exploration of such large parameter spaces requires however great computational resources; adopting physical parameter instead of cosmological ones can then lead to improved efficiency. Further details on the way how $C_{T,l}$ depends on these parameters are outlined in the captions of Figs. 2.3–2.4.

2.5.3 Secondary anisotropies and low–z effects

During the path from the LSS to the observer, several effects induce further anisotropies in the photons' distribution. These anisotropies are often dubbed *secondary* anisotropies to distinguish them from the primary anisotropies tied to recombination, and usually originate at redshifts much lower than z_{rec}. The main physical sources of secondary anisotropies are:

(i) *Curvature and Dark Energy.* While conceptually distinguished, a non–flat geometry and DE affect the CMB spectra in much a similar way. On large angular scales, the rapid variation of the gravitational potentials associated with the passage from a matter–dominated expansion to a curvature– or DE–dominated expansion marks the APS through the ISW effect. The angular position of the peaks is instead altered due to variations to the angular diameter distance.

(ii) *Reionization.* Observations of the Inter Galactic Medium (IGM) show that it is fully ionized at least up to $z \sim 6$. The scattering of CMB photons on free electrons induces further anisotropies in the CMB spectra which, in a first approximation, depend on the total optical depth for Thomson scattering, τ. In the simplest model of a single and instantaneous, or *sharp*, reionization, a non vanishing τ reduces the amplitude of the peaks in $C_{T,l}$ spectra, as the re-scattering smoothers the peaks associated with primary anisotropies, while at largest scales the APS remain almost unchanged.

(iii) *Sunayev–Zel'dovich effect* (Sunyaev and Zel'dovich 1969). CMB photons traversing clusters of galaxies experience inverse Compton scattering on the highly energetic electrons of the Intra Cluster Medium. Scattered photons

acquire energy at the expense of the electrons, resulting in a *diminished* temperature of CMBR in correspondence of the cluster, as photons get shifted from microwave to lower wavelengths. The SZ effect alters the high multipoles of the APS ($l \sim 1500 - 2000$).

Aside from these physical effects, APS are modified by the photons' free–streaming, which produces a transfer of power from lower to higher l's. Although it is simply a geometrical effects, free-streaming is fundamental in accounting for large angle polarization.

While each of the physical parameters discussed in this section and in the previous one affect the APS in a precise and predictable way, there exist combinations of parameters which can be changed in such a way as to leave the temperature anisotropies spectrum almost unchanged. As an example of such degeneracies, in Fig. 2.6 we show the effects of simultaneously varying n_s and τ. In this case, polarization measures can help break the degeneracy (see Cha. 3), in other situations other sorts of data, e.g. analysis of large scale structure, are needed.

As the main focus of this thesis concerns the constraints on reionization history and DE from large angle measurements of CMB polarization, we defer a more accurate discussion of these physical mechanisms and their observational effects on APS to later chapters.

2.6 The polarization of the CMB

Photons undergoing Thomson scattering become linearly polarized, as outgoing radiation cannot have an oscillation mode parallel to its direction of propagation. Nevertheless, if the distribution of the radiation incident on an electron is isotropic, the outgoing radiation has no net polarization, as polarization states originating from incident directions separated by 90° balance each other exactly. A similar argument shows that a dipole pattern is not enough to generate net polarization and therefore the incident radiation field needs to have a quadrupole moment (Kosowsky 1996).

2.6.1 Kinematics of Thomson scattering

Let us consider a (nearly) monochromatic, unpolarized and plane wave of intensity I' incident on a stationary electron. The Thomson scattering cross-section is given by

$$\frac{d\sigma}{d\Omega} = \frac{3\sigma_{Th}}{8\pi}|\vec{\epsilon}' \cdot \vec{\epsilon}|^2 \,, \tag{2.32}$$

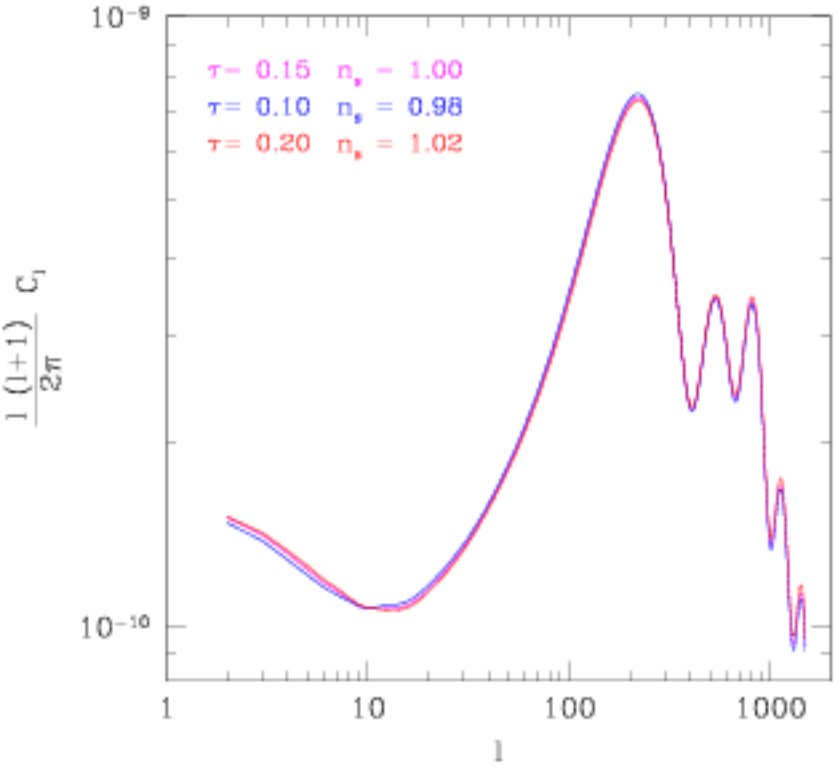

Figure 2.6: Degeneracy of C_{Tl} spectrum with respect to simultaneous changes of n_s and τ.

where $\vec{\epsilon}'$ and $\vec{\epsilon}$ are unit vectors describing the polarization states of incoming and outgoing waves, respectively. The reference frame is chosen so that the scattered waves propagates along the z-axis direction and label $\vec{\epsilon}_x$ ($\vec{\epsilon}_y$) the polarization vectors of the outgoing wave perpendicular (parallel) to the scattering plane. Likewise $\vec{\epsilon}'_x$, $\vec{\epsilon}'_y$ define the polarization vectors of the incoming wave. Since this is unpolarized, $Q' = U' = V' = 0$ while intensities along the directions defined by $\vec{\epsilon}'_x$ and $\vec{\epsilon}'_y$ are equal, $I'_x = I'_y = I'/2$. The scattered intensities are instead

$$\begin{aligned} I_x &= \frac{3\sigma_T}{8\pi}[I_x(\vec{\epsilon}'_x\cdot\vec{\epsilon}_x)^2 + I_y(\vec{\epsilon}'_y\cdot\vec{\epsilon}_x)^2] = \frac{3\sigma_T}{16\pi}I \\ I_y &= \frac{3\sigma_T}{8\pi}[I_x(\vec{\epsilon}'_x\cdot\vec{\epsilon}_y)^2 + I_y(\vec{\epsilon}'_y\cdot\vec{\epsilon}_y)^2] = \frac{3\sigma_T}{16\pi}I\cos^2\theta\,, \end{aligned} \tag{2.33}$$

where θ is the angle between the incoming and outgoing waves. The Stokes parameters of the outgoing wave are then:

$$\begin{aligned} I &= I_x + I_y = \frac{3\sigma_T}{16\pi}I'(1+\cos^2\theta), \\ Q &= I_x - I_y = \frac{3\sigma_T}{16\pi}I'\sin^2\theta\,. \end{aligned} \tag{2.34}$$

Q and U describe the polarization state with respect to sets of directions rotated by $\pi/4$. To obtain U, then, we can simply rotate the $x-y$ plane by $\pi/4$. The

rotated Q will be equal to the U parameter in the original frame. Moreover, Thomson scattering does not induce circular polarization and V remains zero.

When considering a radiation field instead of a single wave, the net polarization of scattered light is determined by integrating eqs. 2.34 over all incoming directions. Notice that the Stokes parameters of outgoing radiation must be defined with respect to a common reference frame. Therefore, the coordinate system for each incoming direction must be rotated about the z–axis by a suitable angle. We obtain then:

$$\begin{aligned} I &= \frac{3\sigma_T}{16\pi}\int d\Omega(1+\cos^2\theta)I'(\theta,\phi)\,, \\ Q &= \frac{3\sigma_T}{16\pi}\int d\Omega\sin^2\theta\cos(2\phi)I'(\theta,\phi)\,, \\ U &= -\frac{3\sigma_T}{16\pi}\int d\Omega\sin^2\theta\sin(2\phi)I'(\theta,\phi)\,. \end{aligned} \tag{2.35}$$

The outgoing polarization state depends only on the intensity distribution of the unpolarized incident radiation. Expanding the incident radiation field in spherical harmonics,

$$I'(\theta,\phi) = \sum_{\ell m} a_{\ell m} Y_{\ell m}(\theta,\phi), \tag{2.36}$$

leads to the following expressions for the outgoing Stokes parameters:

$$\begin{aligned} I &= \frac{3\sigma_{Thom}}{16\pi}\left[\frac{8}{3}\sqrt{\pi}\,a_{00} + \frac{4}{3}\sqrt{\frac{\pi}{5}}a_{20}\right]\,, \\ Q &= \frac{3\sigma_T}{4\pi}\sqrt{\frac{2\pi}{15}}\mathrm{Re}(a_{22})\,, \\ U &= -\frac{3\sigma_T}{4\pi}\sqrt{\frac{2\pi}{15}}\mathrm{Im}(a_{22})\,. \end{aligned} \tag{2.37}$$

Thus, Thomson scattering of an unpolarized radiation field having a non–vanishing quadrupole moment leads to a linearly polarized outgoing radiation. Notice that eqs. 2.37 hold in the reference frame in which the electron is at rest.

2.6.2 Origin of polarization

At times significantly before decoupling, the Universe is hot enough that protons and electrons exist freely in a plasma. During this epoch, the rate for photons to Thomson scatter off of free electrons is large compared to the expansion rate of the Universe. This tight coupling regimes ensures that the photons' distributions behaves like a fluid and therefore can have only a monopole and dipole terms, while higher momenta are rapidly damped away. Prior to decoupling, therefore, no net polarization can arise.

As recombination proceeds and free–streaming of photons begins, higher momenta gradually switch on. In particular, a quadrupole term forms due to velocity gradients in the photon–baryon fluid across the last scattering surface (Zaldarriaga and Harari 1995). In fact, photons, coming from regions where the fluid has slightly different velocities, are seen in the rest frame of the electron with an intensity which depends on direction. However, as recombination is a fairly rapid process, only a relatively small fraction of photons become polarized before the Universe become totally transparent to CMB.

Furthermore, a quadrupole moment can only arise after a given scale has entered the horizon. We thus expect that on scales still outside the horizon at recombination, the degree of polarization be small. This corresponds to l's laying below the Doppler peak. On the contrary, on smaller scales, the polarization amount depends on the phase of the fluctuation, when it meets recombination, and is stronger for those scales entering recombination in the kinetic stage.

Following all these effects in detail require numerical integration, however the above arguments allow to qualitatively understand the features of polarization APS. In Fig. 2.7 we show the $rm\hat{T}$–, E– and TE– APS for SCDM model. Dotted lines refer to a no–reionization scenario. The E–mode APS show a series of peaks in the range $l \sim 10^2$–10^3, in correspondence of scales that enter the horizon in sonic regime. On this scales $C_{E,l} \sim 10^{-2}$–$10^{-3}\langle C_{T,l}\rangle$, as only a small fraction of photons scatters during the last phases of recombination. On larger scales, no significant quadrupole is present at recombination and the spectrum drastically falls at negligible levels. Moreover, polarization is produced by velocity gradients while temperature anisotropies receive contributions from both density and velocity perturbations, with those from density being the dominant ones. As velocity's and density's oscillations are out of phase, peaks in polarization's APS will have a different position from those of $C_{T,l}$. This arguments also explains why peaks in $C_{E,l}$ increase in height with increasing l, at variance with temperature's spectrum.

This picture is however radically altered when the effects of an early reionization are taken into account. CMB photons can again undergo Thomson scattering on free electron and new polarization can form. If reionization occurs at redshifts $10 < z < 30$, as suggested by recent data., the associated optical depth can be relatively low, due to the low density of electrons with respect to recombination. However, the CMB quadrupole has been greatly enhanced by free–streaming since z_{rec}, and even a low τ can produce a significant signal. As

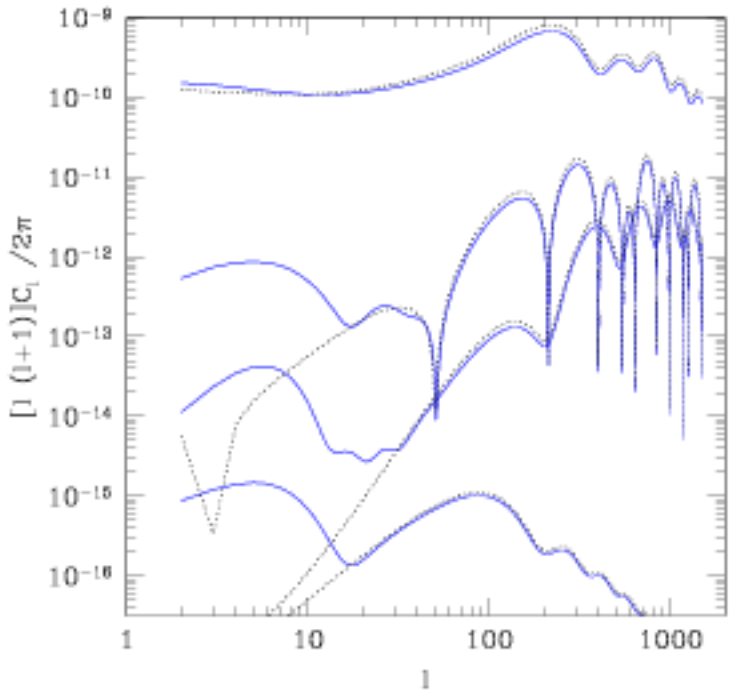

Figure 2.7: Angular power spectra $C_{Y,l}$ for (top to bottom) $Y = T, TE, E, B$, for a ΛCDM model with $\Omega_m = 0.3$, $\Omega_b = 0.05$, $h = 0.7$ and $n_s = 0.99$. Dotted curves refer to a model with no reionization, while solid curves refer to $\tau = 0.17$.The most noticeable effect due to reionization is the appearance of a new peak in the low-l region of polarization APS.

shown by the solid lines in Fig. 2.7, the most noticeable imprint of reionization on CMB is the appearance of new peaks in polarization APS at low l's (see Chapter 3 for a more thorough discussion).

2.6.3 B–modes and lensing

We conclude this Chapter with a brief discussion of B–mode polarization. Density fluctuations, being a scalar field, produce features in CMBR that are invariant under parity transform, and therefore contribute only to $\hat{\mathrm{T}}$, E and TE spectra. Tensor modes, instead, add power to all four APS. Then, detection of *cosmological* B–modes would be direct proof of a background of primordial GW's and yet another hint in favour of Inflation.

Inflationary models predict that GW's rapidly decay on scales below the Hubble radius, therefore we expect the $C_{B,l}$ to be relevant up to $l \sim 200$, and rapidly decrease afterward. In the absence of reionization, the best observational window for B–modes is then $50 \lesssim l \lesssim 200$ (see Fig. 2.8). A non–vanishing optical depth acts on $C_{B,l}$ in much the same way it did on $C_{E,l}$: however, for

B–modes the reionization peak has about the same height has the main peak, although being more affected by CV.

Detection of B–modes is impaired by the low–value of the expected signal. The relative contribution to the level of polarization induced by GW's with respect to density fluctuations, depends on the tensor–to–scalar ratio, r, which in turn is fixed by n_s. For realistic values of n_s, the $C_{B,l}$ spectrum is expected to be $1\sim2$ orders of magnitude smaller than E–mode spectrum for $l \lesssim 200$.

Despite detection of the B–mode polarization proves to be quite difficult, a large theoretical effort on the study of its properties has been made (Seljak and Zaldarriaga 1997). In fact, measuring the $C_{B,l}$ power spectrum appears to be, at the moment, the only way to obtain precise enough detection of the tensor perturbations, although some loose constraints are available by the analysis of current anisotropy data (Spergel 2003, Peiris et al 2003). In Inflation models, the amplitude of the tensor perturbations is directly proportional to the energy scale at which Inflation occurred. Then B–mode polarization becomes a probe of GUT–scale physics at 10^{16} GeV (Kinney 1998).

Aside the low intrinsic level of B–modes, further difficulties in detection of tensor modes arise from the effects of *gravitational lensing* on CMB. Lensing by large scale structure induce additional shear and vorticity in the CMB fields, even in the absence of any intrinsic handedness. In particular, lensing causes a leakage between different polarization modes, so that a spurious B–mode can appear.

It can be shown that lensed APS are related to unlensed ones by:

$$\begin{aligned}
\tilde{C}_{T,l} &= C_{T,l} + W^{l'}_{11} C_{T,l'} \\
\tilde{C}_{E,l} &= C_{E,l} + \frac{1}{2}[W^{l'}_{11} + W^{l'}_{22}]\ C_{E,l'} + \frac{1}{2}[W^{l'}_{11} - W^{l'}_{22}]\ C_{B,l'} \\
\tilde{C}_{B,l} &= C_{B,l} + \frac{1}{2}[W^{l'}_{11} - W^{l'}_{22}]\ C_{E,l'} + \frac{1}{2}[W^{l'}_{11} + W^{l'}_{22}]\ C_{B,l'} \\
\tilde{C}_{ET,l} &= C_{ET,l} + W^{l'}_{33}\ C_{ET,l'},
\end{aligned} \tag{2.38}$$

Details of the physical mechanism responsible for lensing are here encoded by the *filter* functions $W^{l'}_{il}$ $(i = 1, 2, 3)$: their full analytical expressions can be found in (Zaldarriaga and Seljak 1998). For the purpose of this discussion, it suffices to say that (i) they are oscillatory functions of l' and their main contribution is concentrated around l, and (ii) filters corresponding to different i's, only differ at the % level. Accordingly their differences are much smaller than their sum. The main effect of lensing on $\tilde{T}$, E and TE spectra, therefore, amounts to smearing the l–dependence.

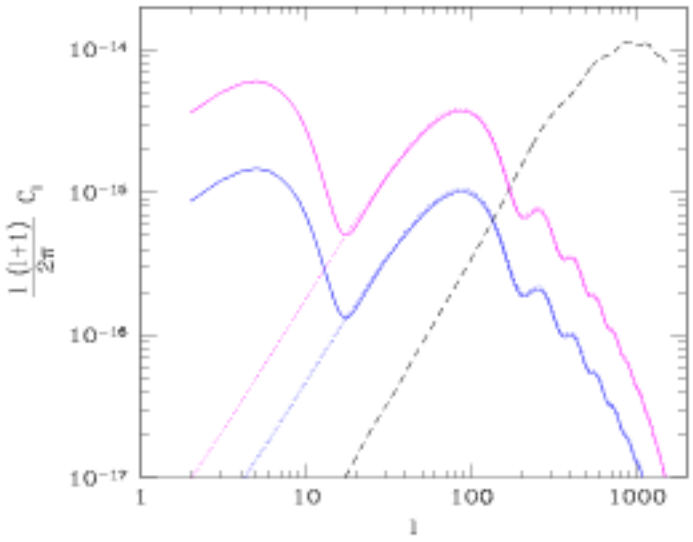

Figure 2.8: B–spectra possible lensing effect. Solid lines are for $\tau = 0.17$. Dotted lines are for $\tau = 0$. The magenta (blue) lines are for $n = 0.95$ (0.99). The black dashed line shows the B–mode generated by lensing the E–mode of the $n = 0.95$ model. Clearly the observational window for the B–mode due to GW's goes up to $l \simeq 100$. Resolving angles $< 3°$, only allows to confirm the B–mode due to lensing.

For polarization spectra an additional effect consists in the leakage between different polarization modes. In particular, the third row of eqs. 2.38 shows that gravitational lensing can induce a spurious B–mode even if unlensed $C_{B,lm}$ vanish. Moreover, as the E–mode can surpass the B–mode by more than a factor of 10^2, the term proportional to $C_{E,l}$ can dominate over those proportional to $C_{B,l}$, despite the differences in the magnitude of the respective coefficients.

In Fig. 2.8 the APS of the lensing–induced B–mode is shown by the dashed line. Depending on the value of r, primordial B–modes surpass lensing–induced ones up to multipoles $l \sim 100 - 200$. At higher multipoles, corresponding to angular scales $1°$, detection of B–mode polarization does not provide any insight on inflationary physics.

Additional complications arise in the case of incomplete sky coverage. As shown in sec. 2.2, E and B modes are non–local quantities; if measurements are available only on a finite sky–patch, decomposition of polarization field into electric and magnetic parts is not well defined, and the two polarization modes mix. These leakage is significant on the largest scales probed, and becomes progressively negligible at scales much smaller that the size of the region explored. It is then clear why probing primordial GW's with CMB polarization requires a full sky experiment.

Chapter 3

Cosmological Reionization

The process of cosmological reionization plays a key role in the production of secondary CMB polarization. The capability itself of detecting large angle polarization strongly depends on details of the reionization history. A full understanding of this process is then necessary in order to comprehend the low l's features in polarization APS. Conversely, measurements of CMB spectra can provide useful constraints on several reionization models. In this chapter, we briefly review the theoretical and observational picture of reionization before the last release of measurements by the WMAP satellite (Spergel 2006), and then debate what insights can be gained through large angle CMB measurements.

3.1 Simple reionization history

After recombination, the fraction of free electrons drops to levels $x_e \lesssim 10^{-4}$ and the Universe becomes transparent to CMB photons. Present day Inter Galactic Medium (IGM) is fully ionized, but the current density of free charged particles is so low that the scattering time for CMB photons, $t_s \simeq 4.45 \cdot 10^{18} \Omega_b^{-1} h^{-2}$s, greatly exceeds the Hubble time, $t_H = 3.09 \cdot 10^{17} h^{-1}$s. However, these characteristic times scale with the expansion factor, a, in different ways. While t_H's scaling depends on the cosmological model, it is generally slower than the scaling $t_s \propto a^3$, due to volume effects. If reionization occurs early enough secondary polarization may arise.

The lack of strong HI absorption in the spectra of high redshift objects, the so–called Gunn–Peterson through, shows that IGM Hydrogen is already fully ionized at redshift $z \sim 5$–6 (see, e.g., (Fan et al 2000). Helium reionization, instead, occurs at $z \sim 3$ (Songaila and Cowie 1996, Songaila 1998). On the other hand, a reionization occurring too early would erase all information on primordial anisotropies from CMB spectra, as all photons undergo new scatter-

ings. Detection of acoustic peaks in C_{Tl} spectra then provides an evidence that reionization has not occurred too early. In particular, the peaks' height places an upper limit on the redshift of reionization, $z_{ri} \lesssim 30$ (Stompor et al 2001, Spergel 2003,). Taken together, these findings imply then $6 \lesssim z_{ri} \lesssim 30$. As we will discuss in Sec. 3.2, recent observations have yet to provide a definitive assessment of the epoch of reionization.

Until few years ago, cosmological reionization was generally ascribed to the radiation produced by metal–free stars in early galaxies (see, Loeb and Barkana 2001 for a review). Reionization is then strongly connected with the formation of the first objects. In ΛCDM cosmology, structure formation proceeds through hierarchical clustering. The first objects are predicted to condense at redshift $z \sim 25$ in dark matter (DM) halos with masses $\sim 10^6 M_\odot$, corresponding to 3σ peaks of the density fields. These halos represent the balance point between collapse mass and cooling mass, and provide then the natural candidates for the hosts of the first astrophysical sources. The basic outline of reionization assumes then that gas falling into DM gravity wells condense into ionizing sources. Radiation escaping from the early proto–galaxies must traverse the surrounding high–density neutral regions, before reaching the low–density IGM. In the high–density regions, recombination rates are sufficiently high to keep Hydrogen neuter. In this phase, the IGM is characterized by low–density ionized regions separated from neutral regions by ionization fronts. Once ionized regions starts to overlap, the combined photon flux rapidly overcomes the remaining neutral bubbles, and Universe is reionized.

A key role in the formation of the first ionizing sources is played by cooling mechanisms. Gas falling into gravity wells is heated through collisional shocks to characteristic virial temperatures of few hundreds Kelvin degrees. In order for collapse to continue until astrophysical objects are formed, an efficient way to dissipate this thermal energy is needed. Otherwise, the gas would simply reach hydrostatic equilibrium and remain in this state until the baryon–DM halo becomes incorporated into larger structures through merging.

A viable mechanism for energy dissipation is radiative cooling via molecular Hydrogen (see, e.g.,Tegmark 1997). If enough molecular Hydrogen is present, the first stars form in halos with virial temperature in the range $100\mathrm{K} \lesssim T_{vir} \lesssim 10^4\mathrm{K}$. Such stars are expected to be very massive, $M \sim 200 M_\odot$, thus burning rapidly. The resulting supernovae explosions strip the host halo of most gas, thus halting further star formation for a time and enriching the surrounding IGM with metals. Moreover, only a small fraction of total baryons,

possibly lower than ~ 0.01 is expected to form PopIII stars. However, ionization requires an energy of 13.6eV per Hydrogen atom, while fusion reactions free ~ 1 MeV for each Helium nucleus produced. The ionizing radiation emitted by PopIII stars and supernovae might then be enough to reionize the Universe by $z_{ri} \sim 10$–12. If H_2 cooling is not efficient, stars can form only in halos with $10^4\mathrm{K} \lesssim T_{vir} \lesssim 10^5\mathrm{K}$, due to atomic line cooling. In this case reionization is completed at lower redshifts.

Detailed predictions of these models depend on several parameters describing the population of the first stars, such as the kind and slope of initial mass function (Salpeter or top–heavy), and the efficiency of ionization, e.g., the fraction of baryons turned into stars, f_*, the number of ionizing photons per baryon, N_γ, and the fraction of photons escaping into the IGM, f_{esc}. Feedbacks processes also plays very important roles. Many studies however agreed that reionization should have been a very rapid process (see Cen and McDonald 2002, Fan et al. 2002).

Assuming then that reionization is an instantaneous and isotropic process, the so–called *sharp* reionization, the associated optical depth to Thomson scattering for CMB photons, τ, is given by:

$$\tau(z_{ri}) = \int_0^{z_{ri}} dz \, \frac{(1+z)}{H(z)} \sigma_{Th} n_e(z), \tag{3.1}$$

where $H(z)$ is the Hubble constant as a function of redshift, σ_{Th} is the Thomson cross–section and $n_e(z)$ is the number density of electrons. Here we assumed that the fraction of ionized electrons, x_e, vanishes at $z > z_{ri}$ while $x_e = 1$ if $z \leq z_{ri}$ (i.e., we are neglecting the effects of Helium ionization as they do not bear a great impact on CMB features). In the case of more complicated reionization histories, $x_e(z)$ appears in the integral of Eq. 3.1. The value of τ clearly depends on cosmology, however, for a broad range of cosmological models, the range of z_{ri} discussed above leads to $0.03 \lesssim \tau \lesssim 0.30$ (see Fig. 3.1).

Low values of the optical depth, $\tau \sim 0.05$, were however favoured by several observational and numerical evidences. Observations of QSO's in the redshift range $5 \lesssim z \lesssim 6$ showed an increase in the opacity of the Lyman–α (Lyα) forest toward $z \sim 6$ (Djorgovski et al. 2001), moreover, evidence of the Gunn–Peterson effect was detected in the spectrum of a single QSO at $z = 6.3$ (Becker et al. 2001). The Gunn–Peterson test saturates for very small IGM neutral fractions ($x_n \sim 10^{-4}$ for an homogeneous IGM, and $x_n \sim 10^{-2}$ in any case;nonetheless, these findings were generally taken as indications that observations at $z \sim 6-7$ were probing the end of reionization, on the basis of several additional hints.

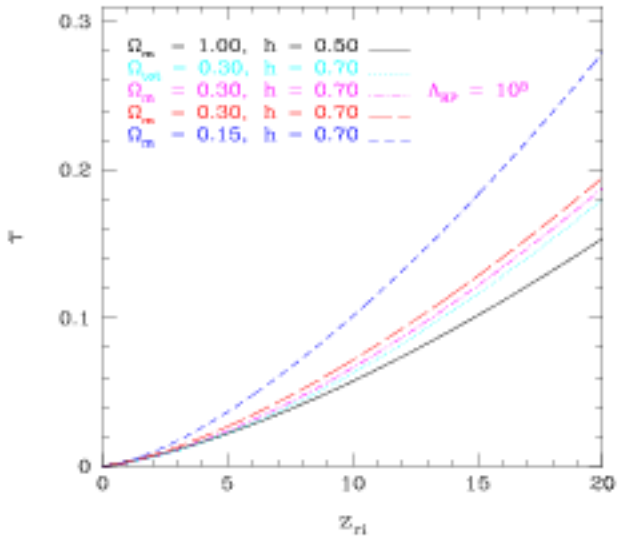

Figure 3.1: Opacity τ as a function of the reionization redshift, assuming instantaneous reionization at z_{ri}. In the third model, dark energy is due to a scalar field, self–interacting through a Ratra–Peebles potential (Ratra and Peebles 1988) , with $\Lambda_{RP}/\mathrm{GeV} = 10^3$. For $\tau > 0.16$ reionization must have occurred at $z_{ri} > 15$, unless matter density is significantly lower that the currently accepted value, $\Omega_m \sim 0.30$.

In fact, extrapolation to high–z of the ionizing flux observed today leads to $z_{ri} \sim 8 - 10$ for a wide range of models (Miralda-Escudé 2003). These figures were consistent with those from numerical simulation of first objects' formation and reionization, which generally predicted $7 \lesssim z_{ri} \lesssim 12$, even leaving all parameters free to vary along the whole range of allowed values and allowing for high efficiency of H_2 cooling. Finally, a reionization occurring around $z_{ri} \sim 7-8$ could reconcile the excess of galactic satellites predicted by N–body simulations with observations. In fact, pressure exerted by the ionizing photons could free baryons from the gravity wells of DM halos with masses $M \lesssim 10^{5-6} M_\odot$ (Bullock, Kravtsov, and Weinberg. 2000). The *photoevaporated* halos would then be hardly detectable.

3.1.1 Effects on CMB power spectra

On the ground of the theoretical and observational picture described in the previous section, studies of the effects of reionization on CMB spectra focused on models of sharp–reionization with relatively low values of optical depth, $\tau \sim 0.03 - 0.05$.

The probability that a photon reaches the observer without rescattering after recombination is given by $e^{-\tau}$. Rescattered photons lose any information

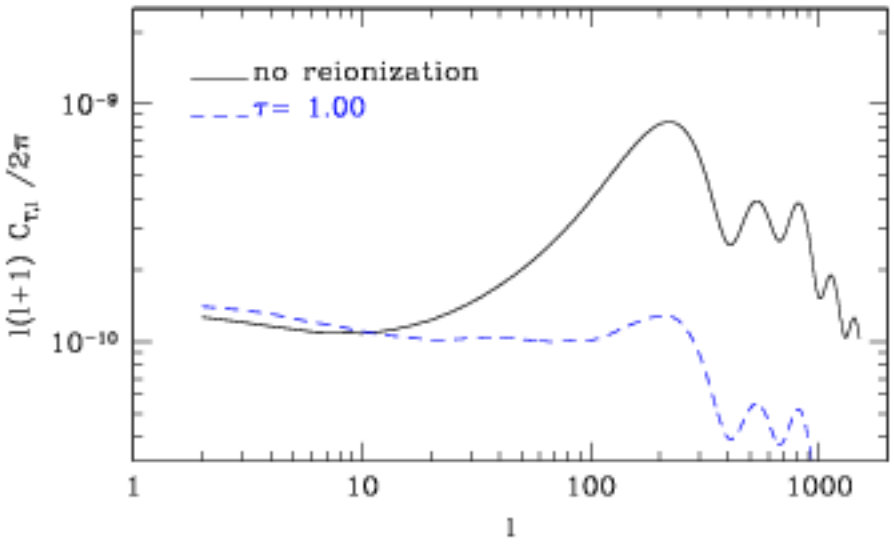

Figure 3.2: Anisotropy spectra for a ΛCDM model with different values of τ. Solid lines has no reionization, while dashed line corresponds to $\tau = 1.00$. High values of the optical depth erase the acoustic structure of the peaks, while at low multipoles new anisotropies form which compensate the loss of primordial anisotropies. Spectra are COBE–normalized.

on recombination they carried, resulting in a reduction of $C_{T,l} \propto e^{-2\tau}$ on multipoles greater than a few tens. For values $\tau \sim 1.0$, the acoustic structure of the APS is greatly suppressed. New anisotropies form instead on scales corresponding to the Hubble radius at reionization, $l \lesssim 20$. For temperature APS, this effect compensates the power's reduction and, at low l's, the spectrum remains almost unchanged (see Fig. 3.2).

Similar effects are produced by changes in the parameters defining the primordial power spectrum of density fluctuations. In fact, decreasing the spectral index n_s reduces power on small scales (high wavenumbers or multipoles) with respect to large scales, thus lowering the peaks' height. The $C_{T,l}$ spectra are then degenerate for simultaneous changes of τ and n_s; in particular, an increased optical depth can be balanced by raising n_s by a suitable amount (see Fig. 2.6). Including the variations of power spectrum normalization A and of physical baryon density $\Omega_b h^2$ further complicates these degeneracies.

As seen in Sec. 2.6.2, CMB polarization is proportional to the quadrupole moment of temperature's anisotropies and primordial polarization on scales greater than few degrees has vanishing levels. At reionization, $a_{T,22}$ has grown due to free-streaming and the newly produced polarization anisotropies greatly surpass the loss of primordial polarization. This results in a new peak in $C_{E,l}$ (see Fig. 3.3) and $C_{B,l}$. The height of this peak is related to τ, while its

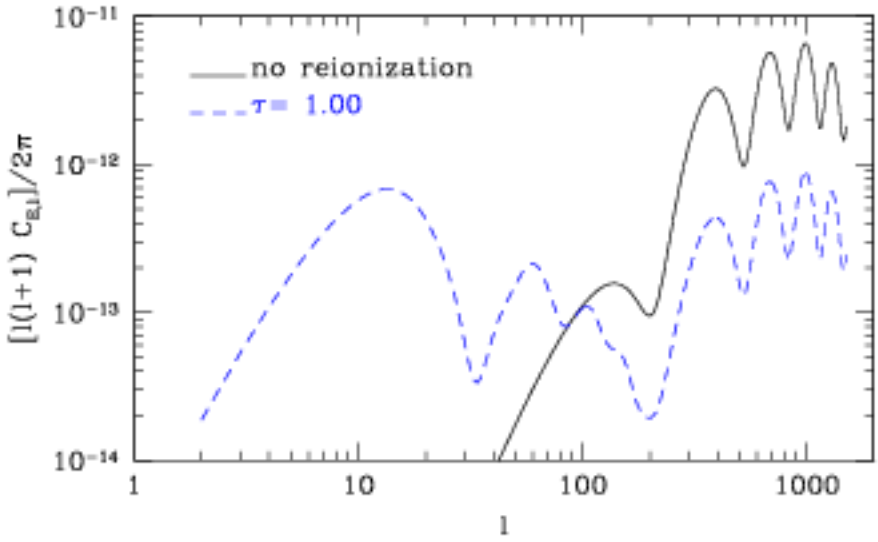

Figure 3.3: Same as Fig. 3.2, but for E–mode polarization. Notice the new peak at $l_{ri} \sim 15$.

position in harmonic space is given by $l_{ri} \sim k(\eta_0 - \eta_{ri})$. Here η_0 and η_{ri} are the conformal time today and at recombination, while the wavenumber k is set by the time elapsing between recombination and reionization. Ultimately then, l_{ri} provides an estimate of z_{ri}. Within the context of sharp reionization, the relation between τ and z_{ri} is unique; thus, the height and position of the reionization peak convey essentially the same information. Additional peaks may arise at greater multipoles if τ is sufficiently high. The high multipoles of polarization APS, instead, are affected by reioinization in a way similar to the power reduction in $C_{T,l}$ peaks.

The appearance of a new peak in polarization APS has two important consequences. First of all, it greatly enhances the rms polarization level at low multipoles, thus opening a new observational window for experiments exploring large angular scales. As an example, $\tau \sim 0.05$ corresponds to an E–mode polarization signal of $\sim 0.2\,\mu$K on scales of 7°, rising to $\sim 0.5\,\mu$K for $\tau = 0.15$. Moreover, The reionization peak is only slightly affected by n_s, as such scales were far outside the horizon at recombination. In principle, polarization measurements can break the τ–n_s degeneracy present in $\hat{T}$–spectra. However, large scales are affected by significant CV, and it is not *a priori* clear whether an experiment measuring only large angles polarization could actually determine the optical depth.

3.2 WMAP1 results on the optical depth

The above picture was radically modified by the WMAP first–year results (Spergel et al. 2003). The WMAP observatory, launched in 2001, measured $\hat{T}$, Q and U using radiometers operating at five frequencies of 22.8, 33.0, 40.7, 60.8 and 93.5GHz. The first year–data[1] did not include polarization maps, due to difficulties in assessing residual systematic errors in U maps (Kogut at al. 2003). Cross correlation between different Stokes' parameters, instead, are largely unaffected by such errors. Detection of TE–correlation , using either $\hat{T}Q$ and $\hat{T}U$ correlation functions, or a direct estimate of $C_{TE,l}$ spectrum, led then to a value of the optical depth much higher than previously thought, $\tau = 0.16 \pm 0.04$ (68 % c.l., *model independent*). This can well be considered the most striking result of WMAP first–year release.

As other cosmological parameters' estimates were consistent with those obtained from pre–WMAP data, such high optical depth is likely to have an astrophysical rather than cosmological explanation. This led to a renewed interest in the study of reionization history and its connection to early objects formation.

Within the context of sharp reionization, an optical depth $\tau = 0.17$ corresponds to a reionization redshift in the range $15 \lesssim z_{ri} \lesssim 20$, depending on cosmology. Several mechanisms have been proposed to account for such an early reionization. The implementation of semi–analytic models of galaxy formation and Monte Carlo radiative transfer codes within high resolution N–body simulations, showed that PopIII stars in early galaxies can account for values up to $\tau \lesssim 0.15$ (Ciardi, Ferrara and White 2003). Despite the fact that feedback effects are yet to be fully assessed, this figure seems the upper limit achievable within this scenario, and requires suitable tuning of parameters (Ricotti and Ostriker 2004).

Earlier ionizations, and higher τ, could be produced by non–stellar mechanisms, such as miniquasars powered by intermediate mass black holes (madau et al. 2004). In this scenario, black holes formed around $z \sim 25$ and then become incorporated into progressively larger systems where they could accrete cold material;, the resulting X–ray emission would be able to reionize Hydrogen by $z_{ri} \sim 15$. Alternatively, the action of black holes in small galaxies has been considered in this case X–ray reionization is completed by stellar emission at redshifts ~ 7.

[1] Publicly available through the LAMBDA archive:
http://lambda.gsfc.nasa.gov/product/map/

All these models, while able to account for an high optical depth, have problems in explaining the Lyα and Gunn–Peterson data at $z \sim 6$. While recent analysis of luminosity function of Lyα emitters indicate that the ionization state of the IGM is largely unchanged between $z = 5.7$ and $z = 6.5$ (Rhoads and Malhotra 2001), the apparent contradiction between WMAP's findings and QSO's observations implies that reionization is a more complex process than previously thought.

3.3 Complex reionization histories

An intriguing hypothesis, being investigated lately, is that reionization occurred twice, or even several times (Cen 2003, Wyithe 2003,Sokasian et al. 2004). Radiation emitted by PopIII stars causes the photodissociation of H_2 molecules, thus inhibiting the formation of new objects until much later redshifts, at which line cooling becomes a viable options. However, feedback mechanisms, like X–ray emission from supernova explosions or miniquasars, can efficiently trigger the formation of new H_2, thus allowing for a prolonged production of PopIII stars. The resulting ionizing photon flux is able to bring about a complete reionization by $z_{ri} \sim 15$–16. This first ionization is followed by a short ($\Delta z \sim 1$) epoch in which the IGM stays completely ionized. Meanwhile supernova explosions enrich both galactic and intergalactic medium with metals.

When metallicity reaches a critical value, metal cooling supplant molecular Hydrogen cooling, allowing for the formation of PopII stars with a Salpeter IMF. Ordinary stars are far less efficient emitters of ionizing photons than very massive metal–free stars by a factor of ~ 10. The transition from PopIII to PopII star formation is associated to a strong decrease of the ionizing flux, and the ionized IGM fraction falls to $x_e \sim 0.5 - 0.6$. In this phase, the thermodynamical state of the IGM is regulated by two competing processes: Compton cooling by CMB photons and photoheating by the stars themselves. Star formation then happens almost exclusively in large halos, where atomic line cooling is efficient. Eventually, enough PopII stars are formed, photoionization again overcomes recombination and the Universe is reionized for the second time at $z_{ri} \sim 6$.

While numerical details depend on several parameters, the broad outline of this double reionization history is a characteristic of all scenarios with top–heavy IMF, if feedback effects continuously trigger a significant H_2 formation. In Fig. 3.4, the behaviour of the neutral Hydrogen fraction, and the complimentary ionized fraction, is plotted for a typical double reionization model.

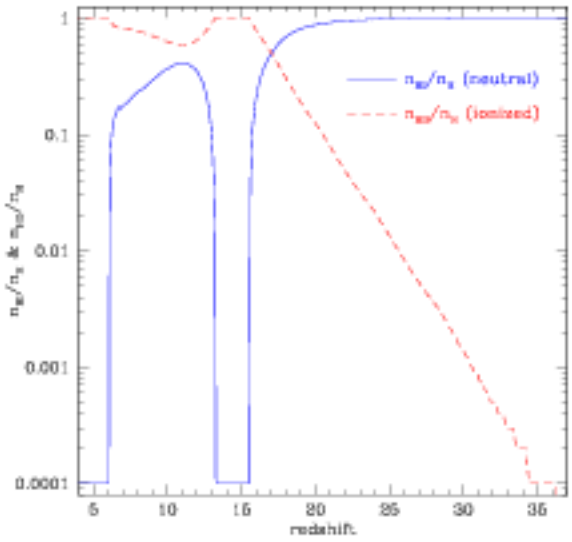

Figure 3.4: Redshift evolution of the neutral (solid) and ionized (dashed) Hydrogen fraction in a model with double reionization (from Cen 2003.

However the balance between UV photodissociation and X–ray production of molecular Hydrogen depends on the spectrum of the earliest sources (see Haiman & Abe 2000). Under suitable assumptions, PopIII star formation can end, due to complete destruction of H_2, before the Universe is completely reionized. PopII star formation, being tied to atomic line cooling, happens efficiently only in halos with virial temperature $T_{vir} \gtrsim 10^4$K, which collapse at lower redshift. In the intermediate period, lasting from $z \sim 15$ to $z \sim 7$–8, the Universe is left in a state of partial reionization, for suitable choices of efficiency and IMF parameters. At variance with double reionization models, the ionized fraction x_e steadily increases during the PopIII phase, reaching levels ~ 0.5, and then remains approximately stable until PopII stars begin forming at high rates. In this case, the Universe undergoes a single reionization event, achieved in two steps (Haiman and Holder 2003).

Alternative models of two–steps reionization, involve more *exotic* sources, like decaying heavy sterile neutrinos (Hansen and Haiman). Decay products include highly energetic electrons and positrons, which could ionize the neutral Hydrogen through direct collisions or interact with CMB photons via inverse Compton scattering. In turn, the scattered photons could gain sufficient energy to photoionize additional atoms. In the end, a significant fraction ($\sim 1/3$) of the energy produced by the decay is available to Hydrogen ionization, resulting in a partial reionization ($x_e \sim 0.5$) at redshifts $z \sim 25$. Again, reionization is completed by stellar emission around $z \sim 6$–7. In this scenario, reionization is

only partially related to structure formation.

3.3.1 Effects on CMB

The models discussed in the previous section, even when corresponding to the same optical depth, are characterized by widely different reionization histories. It is commonly stated that APS are dependent on total optical depth. While it is true that τ is the main reionization parameter shaping the CMB spectra, differences in the reionization history may leave their imprint on APS, particularly on $C_{E,l}$. In fact, the evolution of the radiation field due to Thomson scattering can be written as (see Zaldarriaga 1996), also see Sec. 2.6.1):

$$\frac{d}{d\eta}\hat{I}(\vec{n})|_{Thomson} = -a\sigma_{Th}n_e\, x_e\left[\hat{I}(\vec{n}) + \int d\Omega' \delta\hat{I}(\vec{n}', \vec{n})\right] . \qquad (3.2)$$

Here $\delta\hat{I}(\vec{n}', \vec{n})$ represents the contribution to radiation scattered into direction $\vec{n}$ due to radiation from direction $\vec{n}'$; the explicit dependence of all quantities on the conformal time, η, has been omitted. Similar expressions hold for the Stokes parameters.

Equation 3.2 show then, that evolution of temperature and polarization anisotropies depends not only on integrated optical depth, but also on the function $x_e(z)$. In more exotic models, like the decaying heavy neutrinos, additional degrees of freedom could be provided by a non–trivial scaling $n_e(z)$.

Before studying in detail the effects of complex reionization histories on APS, let us outline some general considerations. CMB features are sensitive to details of reionization only through $x_e(z)$. CMB measurements then allow to constrain reionization's parameters (i.e., N_γ, f_*, f_{esc}) only in an indirect and *model dependent* fashion. Furthermore, different reionization processes with same evolution of $x_e(z)$ cannot be distinguished at all.

Moreover, in Eq. 3.2 the spatial dependence of both the electron density and ionization fraction has been neglected. From the above discussion of reionization processes, it is evident that ionization proceeds in a non–homogeneous way, with regions surrounding star forming halos becoming ionized earlier than regions in the deep IGM. Once HII regions begin overlapping, reionization completes very quickly and patchiness is no longer relevant. It can then be expected that a non–homogeneous reionization produces additional features on APS at multipoles corresponding to the average separation between ionizing sources. Typical star formation models predict ~ 1 very massive PopIII star per DM halo; separation between sources is then simply the inverse cubic root of the DM halo number density, $d_s \sim n_{DM}^{-1/3}$. For PopIII stars forming in $10^{6-7}M_\odot$ halos, the Press

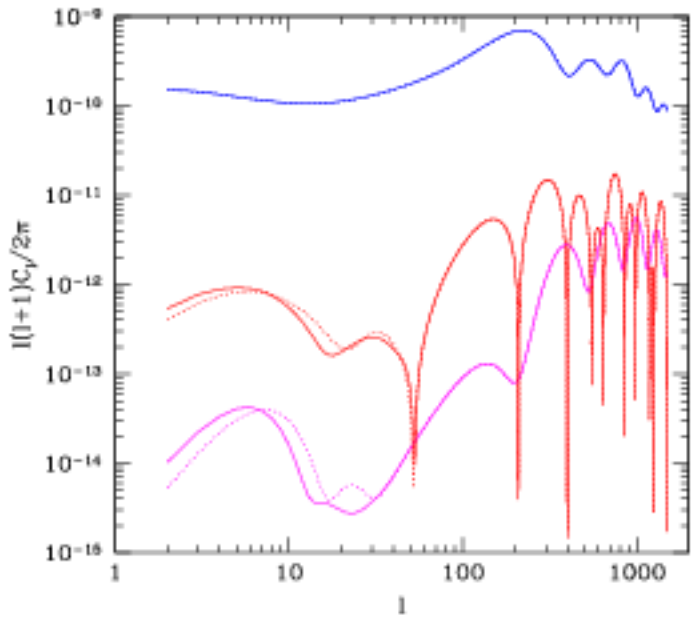

Figure 3.5: APS for different reionization histories corresponding to a sharp reionization model with $\tau = 0.17$ (solid lines) and to a partial reionization with $x_e = 0.60$ and same τ (dotted lines). The main difference is in the position of the first peak in $C_{E,l}$, which shifts to higher l's for the partial reionization model.

& Schecter formalism (Press and Schecter 1974) leads to average comoving separation of $d_* \sim 1\,h^{-1}$Mpc, in a concordance ΛCDM Universe. In turn this corresponds to multipoles $l \sim 5000$. More in general, we expect patchiness features on scales $l \gtrsim 2000$. In this thesis, we are interested in large angular scales; thus, we do not consider patchiness further. However, it must be noticed that even models with similar evolution of the spatially averaged $x_e(z)$ could differ in homogeneity and predict different features at high CMB multipoles.

In order to understand how different reionization histories with the same optical depth mark the APS's, it is useful to compare a sharp reionization model with $\tau = 0.17$ to a partial reionization model in which $x_e = 0.60$ (see Fig. 3.5). Differences between the two models are restricted mainly to the low multipoles ($l \lesssim 40$-50) of $C_{E,l}$ spectra. The position of the reionization peak in harmonic space is fixed by the redshift at which x_e changes rapidly to from the post–recombination level, $x_e \sim 10^{-4}$, to the final value, either 0.60 or 1.00. Such redshifts define the positions of the maxima of the visibility function (see Fig. 3.6):

$$g(z) = \dot{\tau}(z) \exp\left[\int_0^z dz' \dot{\tau}(z')\right] , \tag{3.3}$$

where $\dot{\tau}(z) = -\sigma_{Th}\, a(z)\, n_e(z)\, x_e(z)$ is the derivative of the optical depth with

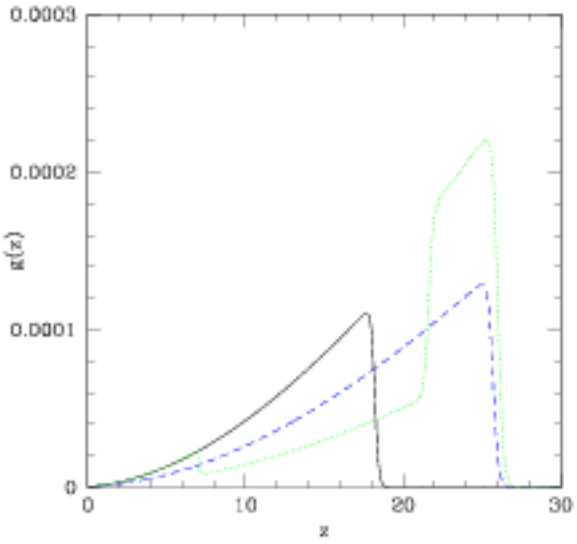

Figure 3.6: Visibility function for the three models with $\tau = 0.17$ and sharp reionization (solid line), partial reionization with $x_e = 0.6$ (dashed line) and double reionization (dotted line); only the low–z evolution is shown. In the double reionization model, maximum scattering rate correspond to the redshift of first reionization, which then defines the angular position of the first polarization peak.

respect to conformal time. The visibility function expresses the probability that a CMB photon reaching an observer at $z = 0$ last scattered between redshifts z and $z + dz$. Maxima of the visibility function then mark the epochs of maximum Thomson scattering: the redshift of the low–z maximum fixes then the angular position of the reionization peak. As in the partial reionization model the change in $x_e(z)$ must occur earlier than in sharp reionization model, in the former case the peak is shifted to higher multipoles. The peak's height, depending mainly on τ, is instead unchanged.

At variance with E–mode APS, $\hat{T}$ spectra show almost no dependence on the additional detail of reionization history, while the features in $C_{TE,l}$ can be understood in terms of temperature and polarization spectra (under perfect correlation, it is simply $C_{TE,l} = \sqrt{C_{T,l} C_{E,l}}$). It is then clear that most information about reionization history encoded in APS is carried by (E–mode) polarization.

The full assessment of the impact of complex reionization histories on APS requires suitably modified linear codes. Great care must be taken in order to ensure stability in numerical integration when $x_e(z)$ varies rapidly (Colombo et al 2005, Bruscoli Ferrara and Scannapieco 2002, Naselsky & Chiang 2004, Holder at al 2003).

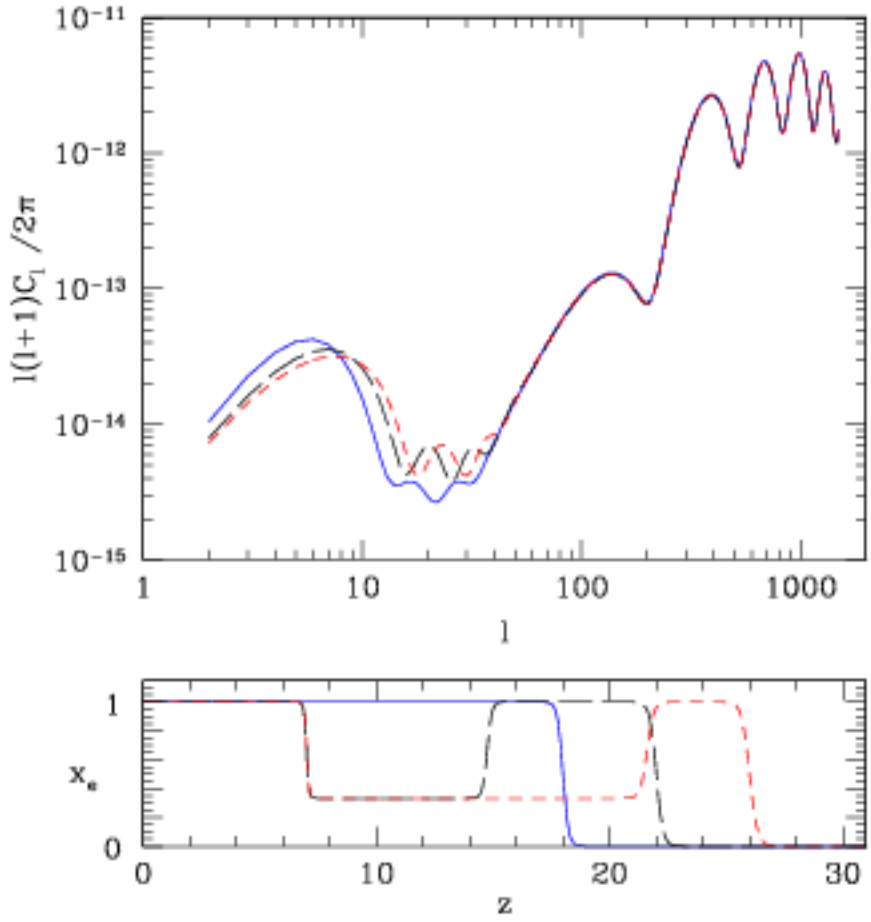

Figure 3.7: E-mode angular power spectra (top panel) and ionization history (bottom panel) for three different models considered in our analysis with $\tau = 0.17$. Solid line represent a ionization profile with $z_r = 18$, long–dashed line has $z_r = 20$ and short–dashed line $z_r = 22$. Different ionization levels are connected by smooth transition in order to guarantee stability in numerical integration.

Results shown in this section are obtained by modifying the public code CMBFAST.

As an example of more complicated behaviour of $x_e(z)$, we consider here double reionization models similar to those discussed in the previous section. In order to reduce the number of free parameters, we assume that the universe is completely reionized a first time at a redshift z_{ri} and then again at $z = 7$, while in the intermediate low–ionization period the fraction of free electrons is fixed at $x_e = 1/3$. The length of the first reionization epoch is fixed by the total optical depth; each model is then specified by two free parameters: τ and z_{ri}.

Figure 3.7 shows the effects of changing the redshift of first reionization, while keeping $\tau = 0.17$ fixed; only C_{El} spectra are plotted. Again, the key dif-

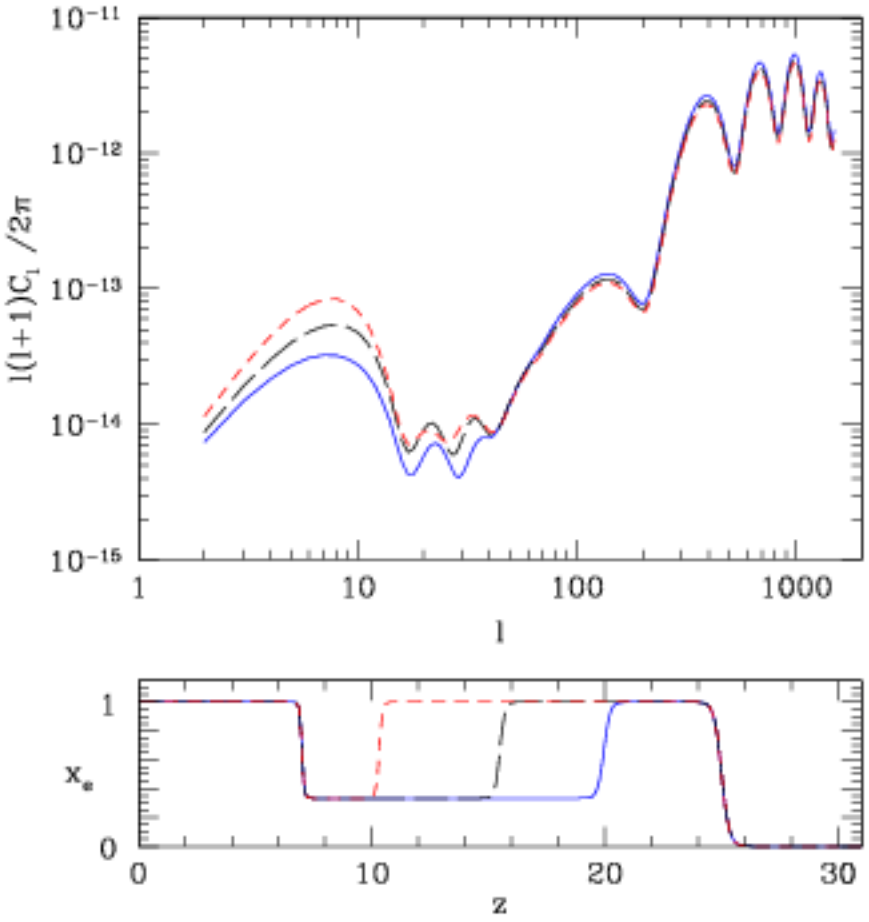

Figure 3.8: $C_{E,l}$ power spectra and ionization histories for three models with $z_r = 25$ and $\tau = 0.17$ (solid line), $\tau = 0.21$ (long-dashed line), $\tau = 0.25$ (short-dashed line).

ference between models consists in the position of the first peak, which depends mostly on z_{ri}, and the APS actually coincide for $l \gtrsim 40$. The increase in x_e at $z = 7$ present in the double reionization models produces an additional maximum in the visibility function, as shown in Fig. 3.6. As all models considered have equal τ, the height of the peaks is almost the same.

In Fig. 3.8, instead, we plot APS for models with same z_r but different τ. Position of the first peak is unchanged, while the peaks' height increases with increasing optical depth. In this case, differences between APS extend to high multipoles and are found also in $C_{T,l}$. This follows from the different values of τ, and does not carry significant information on the evolution of the reionization history. In fact, in each model, the acoustic peaks structure corresponds to that of a sharp reionization model with equal τ.

Barring patchiness effects, then, almost all information on the details of the reionization history encoded in CMB radiation is carried by the low–multipoles of polarization spectra.

3.4 Measuring the optical depth with SPOrt

As discussed in Cha. 5, the SPOrt experiment is optimized to measure polarization on scales of $\sim 7°$, thus exploring multipoles up to $l \lesssim 30$, while keeping under strict control possible leakages from the much higher temperature signal. In the present configuration, the instrumental sensitivity allows for clean Q and U maps for $\tau \gtrsim 0.25$, while for lower optical depths only a measurement of the rms polarization level is expected. In both cases, SPOrt will be able to provide serious checks on reionization, in particular regarding the value of the optical depth and the $\tau - n_s$ degeneracy.

However, on the explored angular scales CV is significant, and the same cosmological models can yield skies with significantly different statistical properties. Parameter estimation from CMB data usually follows a Bayesian approach (Zaldarriaga 1998). However, when dealing with situations in which poor statistics can lead to misleading results, it is preferable to adopt a frequentist approach. For each fiducial model to be tested, a large number of sky realizations are generated. Each realization includes both polarization and anisotropy data, in order to assess the effects of correlating SPOrt's data with temperature measurements from other experiments, e.g. WMAP[2]. To each simulated map a white noise map is added; polarization pixel noise, σ_P is varied within the range expected for SPOrt (i.e., $2\mu\mathrm{K} \leq \sigma_P \leq 4\mu\mathrm{K}$), while temperature sensitivity is kept fixed at a reference level similar to that expected for WMAP's 4–years measures, $\sigma_T = 2\mu\mathrm{K}$. The likelihood function is evaluated in the $\tau - n_s$ for each realization, assuming other parameters to be known, e.g. through analysis of high multipoles of $C_{T,l}$, Large Scale Structure, Supernovae.

In Fig. 3.9, we show joint confidence regions in the $\tau - n_s$ plane, for four random realizations of a fiducial model having $\tau = 0.15$, $n_s = 1.00$ and concordance values of the remaining parameters. Polarization noise holds $\sigma_P = 4\mu\mathrm{K}$, corresponding to 1–year of SPOrt's measurements. The plot clearly show how the degeneracy between optical depth and spectral index affects observational constraints. Comparison of Fig. 3.9 with WMAP results (Spergel 2003), shows that SPOrt can constrain the optical depth with a precision comparable or bet-

[2]While WMAP instruments are sensitive to linear polarization, combining T and Q, U data from different experiments allows to avoid spurious correlations due to systematics.

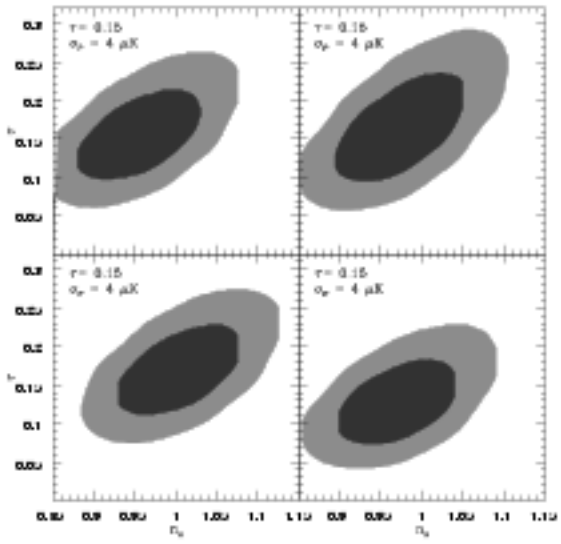

Figure 3.9: Likelihood contours from the analysis of both polarization (Q and U) and anisotropy data, with $\sigma_P = 4\,\mu$K and $\sigma_T = 2\,\mu$K, for $\tau = 0.15$. We assumed a flat model with DE due to cosmological constant, $\Omega_m = 0.3$, $h = 0.65$, $\Omega_b h^2 = 0.22, n_s = 1$. Four independent realizations of the model are shown (see text). More or less heavily shaded areas indicate 1 or 2–σ confidence regions, on the n_s–τ plane.

ter than that achievable by WMAP after similar amount of data taking. Our simulations include contributions by multipoles up to $l \sim 40$, while WMAP results take into account TT correlations for $l \lesssim 900$ and TE cross–correlations up to $l \sim 450$. It is then clear the weight carried by low $C_{E,l}$ multipoles in determination of τ, as confirmed by analyzing only the polarization signal of the maps. In this case, estimates of the optical depth marginally worsen, while n_s is practically unconstrained.

Reducing polarization noise then greatly affects τ estimates, while leaving constraints on n_s mostly unchanged. Fig. 3.10 shows random realizations of the same fiducial model as above, but for $\sigma_P = 2\mu$K (4–years SPOrt's measurements). Confidence regions are now strongly elongated along the n_s axis. The width of the marginalized optical depth distribution is much tighter; determination of the spectral index, instead, only slightly improves, mostly due to improvements in τ estimates.

Fig.s 3.9 and 3.10 also illustrate the variance between different realizations. In most realizations shown, the fiducial model lies inside the 68% confidence level (c.l.) region, but this is not always true. In particular, in one of the realizations of 3.10 the fiducial model is *excluded* at more than 95%c.l. This is not

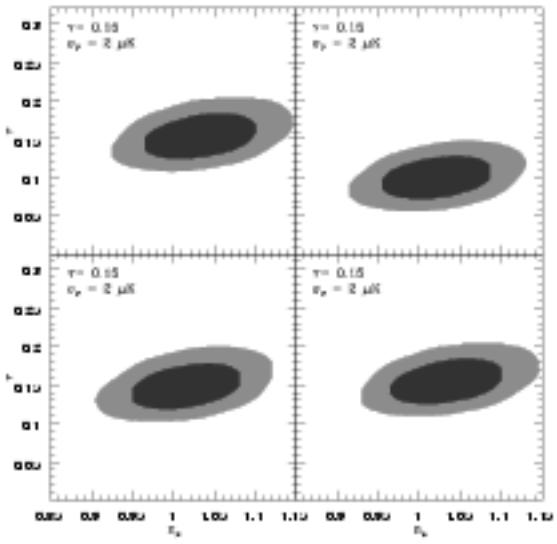

Figure 3.10: Same as Fig. 3.9 but for $\sigma_P = 2\,\mu$K.

surprising. In fact, not counting systematics, we would *expect* the fiducial model to lie outside the 1σ region $\sim 32\%$ of the times, if statystics were Gaussian. For *real* distributions, such figures are higher. In this case, discrepancies between normal and actual distributions become relevant when considering fiducial models with $\tau \lesssim 0.10$, and high level of noise, as proximity of the boundary begins is noticeable in this cases.

Under these circumstances, estimating the likelihood of detecting τ on the basis of the expected errors can lead to misleading results, and a more accurate assessment of cosmic and noise variance is needed. In Fig. 3.11 the fraction of realizations in which a non–vanishing optical depth is found with given c.l., is plotted as a function of the optical depth of the fiducial model. The three panels illustrate results corresponding to (top to bottom), 4, 2 and 1 year mission lifetime. Solid vertical line corresponds to WMAP best estimate, $\tau = 0.17$. A confirmation of this result at a 3σ c.l. within a two–year mission lifetime shall be achieved by SPOrt in $\sim 95\%$ of cases. Conversely, an estimate compatible with vanishing τ at 2σ level, allows to rule out $\tau = 0.17$ with more than 99% accuracy, regardless of the actual value found. Let us also notice that even for very low optical depths, $\tau \lesssim 0.05$, SPOrt obtains a marginal (1σ) detection of the optical depth in 60% of realizations; such figure drops to $\sim 25\%$ if a 3σ detection is required.

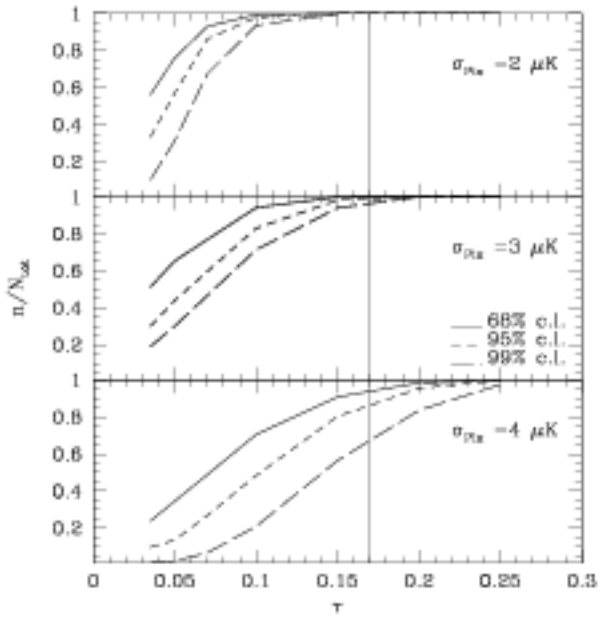

Figure 3.11: Fraction of realization in which a lower limit on the optical depth, ad different confidence levels, is found, as a function of fiducial value of τ and for three different polarization sensitivities.

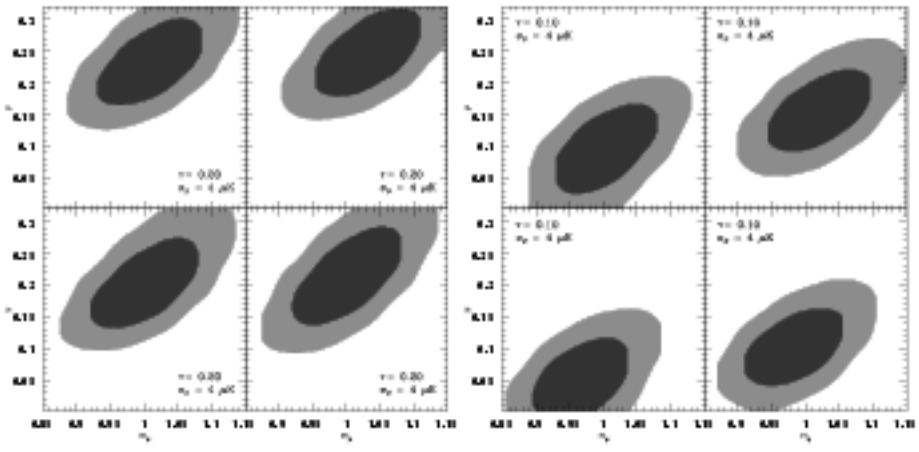

Figure 3.12: Likelihood contours from the analysis of both polarization (Q and U) and anisotropy data, with $\sigma_P = 4\,\mu$K and $\sigma_T = 2\,\mu$K, for $\tau = 0.20$ (left) and $\tau = 0.10$ (right). See caption of Fig. 3.9 for details.

3.5 Constraints on complex reionization histories

Complex reionization histories depend on additional parameters, besides of τ. In principle, all these parameters leave a characteristic imprint on APS's multipoles up to $l \sim 40 - 50$, as discussed in Secs. 3.1.1 and 3.3.1; however the actual detectability of such features by current or near future experiments is not obvious. In this section we debate what constraints can be put on a second reionization parameter, through large angle CMB measurements.

We consider an instrumental design similar to that of SPOrt, in particular assuming that the microwave sky is observed with 7° FWHM instruments, but allow for increasing levels of sensitivity and take into account two different kinds of complex reionization histories. First, we study a toy model of partial reionization, in which the Universe reionizes abruptly at redshift z_{ri}, but the ionized fraction, x_e, can be lower than unity. Then we analyze double reionization models.

3.5.1 Partial reionization histories[3]

In this class of models, reionization history is specified by pairs $z_{ri} - x_e$; alternatively one of the parameters can be replaced by τ. The different descriptions are equivalent; however, as τ is generally regarded as the most influencing, and easily determinable, reionization parameter, it is convenient to specify models by τ and, e.g., x_e pairs. For fixed τ values, a lower x_e is reflected by the reionization peak shifting toward higher-l's (see Fig. 3.5), while different τ's correspond to different peak's heights.

Current measurements are sensitive mainly to total optical depth, while additional parameters are difficult to determine. As an example, in Fig. 3.13 confidence regions in the $z_{ri} - x_e$ plane are shown for two fiducial models with equal $\tau = 0.17$, but with $x_e = 1.0$ or $x_e = 0.6$. Polarization sensitivity holds $\sigma_p = 2\mu$K. These confidence regions are obtained by considering the distribution of best-fit estimates for a large number of realizations of each fiducial model, and delimiting the portion of the plane containing the required fraction of results. Therefore, they represent *exclusion regions*, i.e., they define the portion of parameter space outside of which models can be ruled out with a given degree of confidence. In this way, both CV and instrumental noise are accounted for. As we are concerned with detectability of reionization parameters, we assume the other parameters to be known and fix them to their true

[3]Partly based on Colombo 2004

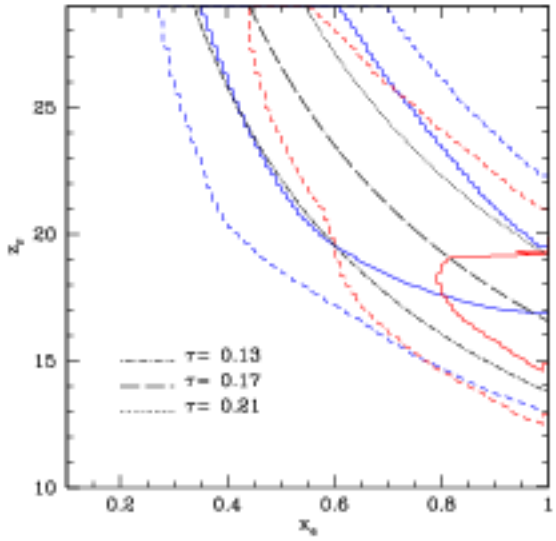

Figure 3.13: Expected likelihood contours in the $x_e - z_r$ plane for models with $\tau = 0.17$ and two different reionization histories; $\sigma_P = 2\mu$K. Solid and short-dashed lines trace the boundary of the 68% and 95% confidence level regions, respectively. In red we plot results for a model in which reionization is complete, while blue lines refer to a model in which $x_e = 0.6$. Likelihood contours are elongated along direction of constant optical depth end do not allow to distinguish between the two models.

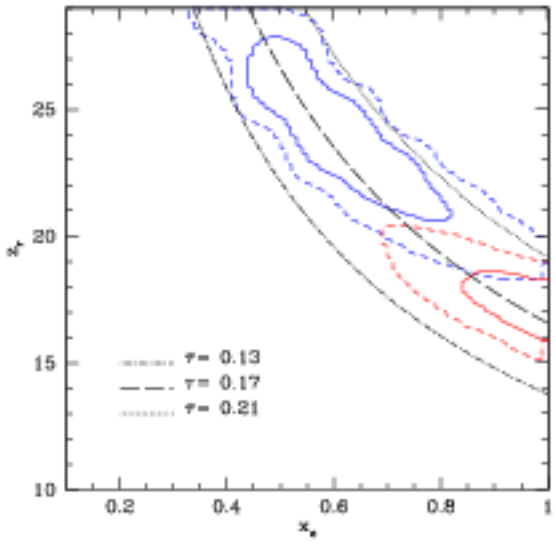

Figure 3.14: Same as fig:s2, but with $\sigma_{pix} = 0.5\mu$K. Likelihood function are elongated along lines of constant τ, it is possible to distinguish between the two models at least at 68% c.l.

value.

The resulting regions are strongly elongated along curves of equal τ. Moreover distributions for the two different models strongly overlap, even at 1σ level, and it is not possible to discriminate between the different reionization histories. It is then clear why it is convenient to parametrize the models using, e.g., $\tau - x_e$ rather than $z_{ri} - x_e$. Lowering noise by a factor ~ 4 allows to constrain the additional parameter with 68% c.l., as shown in Fig. 3.14. The optical depth is again the best constrained parameter. Although the joint 2D constraints show slight tendency in overestimating τ, the distribution of the optical depth is not biased (see Fig. 3.15).

Marginalization over z_{ri} provides the p.d.f for x_e, plotted in Fig. 3.16, for both noise levels considered. At noise level expected for SPOrt, the distributions for the two fiducial models overlap considerably. Both distributions have fairly long tails, which include the value corresponding to the other fiducial model. For instance, a value $x_e = 0.6$ resulted in about $\sim 35\%$ realizations of the partial reionization fiducial model, and $\sim 7\%$ of realizations of the complete reionization model. These figures then provide the degree of confidence with which a given fiducial model can be excluded by an observation. For $\sigma_P = 0.5\mu$K, the overlap is greatly reduced, and some clean conclusions can be reached; e.g., detection of $x_e = 0.6$ allows to reject $x_e = 1.0$ at almost 3σ level.

Complete separation between the two distribution is achieved by a further

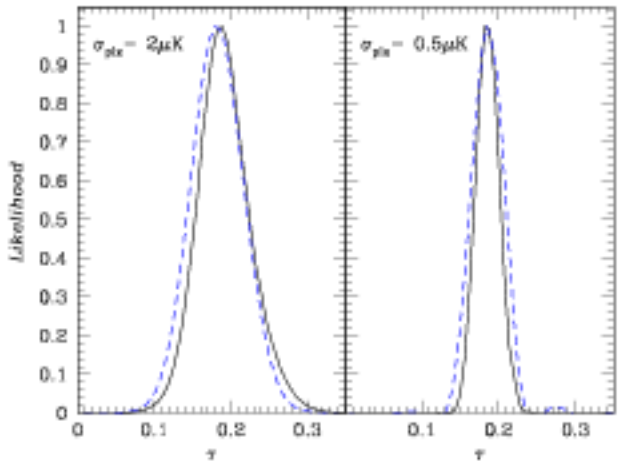

Figure 3.15: Probability distribution for the optical depth for the models of 3.13. Solid lines refer to complete reionization, dashed lines to $x_e = 0.6$. No significant bias in the determination of the optical depth is introduced by the reionization histories considered here.

reduction of polarization noise by a factor $\sim 2-3$, which should be within the capabilities of the PLANCK experiment. However, at these noise levels contribution from B–modes should no longer be ignored, and could provide additional constraints on reionization.

These results depend slightly on the value of the optical depth of the fiducial models. For fixed σ_P, lower τ's correspond to worse signal–to–noise ratios, and discriminating between two models analogous to those discussed above is slightly harder. Variations of other parameters, instead do not significantly alter the above considerations. However, simultaneously estimating additional parameters, instead of assuming them to be known, would lead to a small widening of the distributions of reionization parameters due to the increased number of degrees of freedom.

3.5.2 Double reionization histories[4]

The toy model discussed in the previous section provide an order of magnitude estimate of the sensitivity level required to strongly constrain an additional reionization parameter. The double reionization histories considered in this section, based on physical models of double reionization, provide an example of more complicated $x_e(z)$, which can lead to several interesting consequences for τ estimates.

[4]This section resumes the results of Colombo et al. 2004

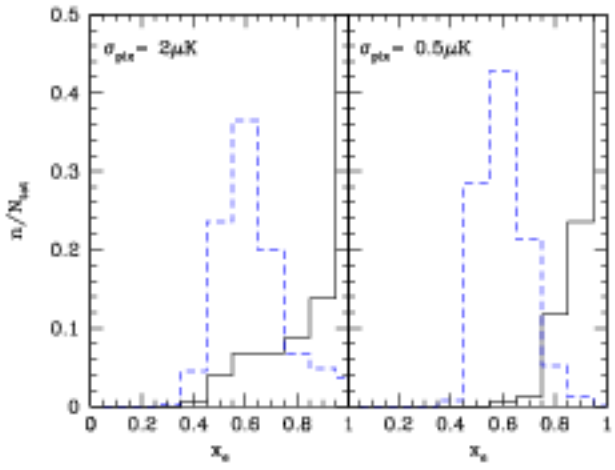

Figure 3.16: Distribution of best–fit ionization fractions, after marginalizing over z_{ri}. Solid lines refer to complete reionization, dashed lines to $x_e = 0.6$. These distribution provide the probability with which one or the other fiducial model can be excluded by available data, instead of telling us the likelihood of a given model being the correct one.

In order to be consistent with observations of high–z IGM, the Universe is required to be completely ionized for $z \lesssim 7$, and to further reduce the number of free parameters the value of x_e between the two reionization periods is fixed at the constant value $x_e = 1/3$. Each model is then defined by two parameters: τ and the redshift of first reionization z_{ri}. Observational and technical considerations lead to consider the part of parameter plane delimited by $0.07 \lesssim \tau \lesssim 0.30$ and $10 \lesssim z_{ri} \lesssim 35$. Not all point falling into this region are however allowed, e.g., for $\tau = 0.17$, viable models must satisfy $18 \lesssim z_{ri} \lesssim 32$ in a concordance ΛCDM cosmology, while for $z_{ri} = 25$ we have $0.12 \lesssim \tau \lesssim 0.27$. Examples of these reionization histories, together with corresponding $C_{E,l}$ are plotted in Figs. 3.7 and 3.8.

Parameters' estimation often assumes a sharp reionization prior; however, CMB spectra depend directly on $x_e(z)$, rather than on τ, and for the class of models considered here, a wrong prior leads to strong bias in τ estimates.

In fact, if prior on the reionization history did not introduce any bias in τ estimates, the distribution of best–fit τ values for a large set of realizations of the same cosmological model should not depend on the prior. Notice that this in not necessarily true for a single realization. Comparing then the probability distribution obtained by fitting sharp reionization model to simulated data, with that obtained by analyzing them as double reionization models, provides a check of the priors.

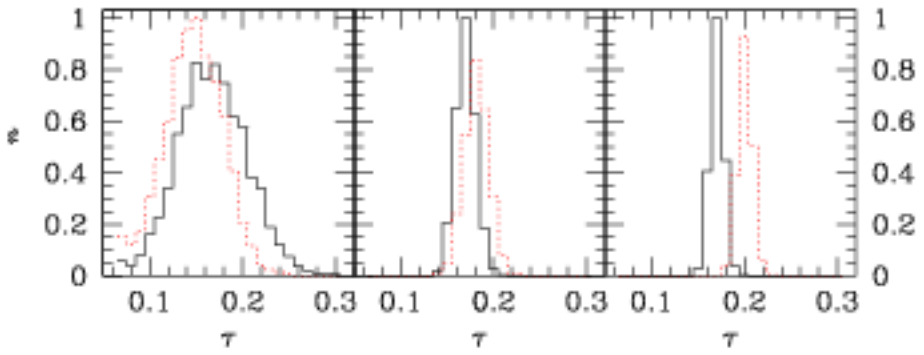

Figure 3.17: Distribution of τ for a with $\tau = 0.17$ and $z_{ri} = 22$, at different noise sensitivity (left to right, $\sigma_P = 3.0, 0.9, 0.3\,\mu$K). Solid lines show results obtained marginalizing over z_r, dotted lines refer to results of checking the same realizations against single reionization models. At high sensitivity, the latter prior give rise to a noticeable bias.

In Fig. 3.17, results of this comparison are shown for a double reionization model with $\tau = 0.17$, $z_{ri} = 22$, analyzed at three increasing sensitivity levels for polarization, left to right, $\sigma_P = 3.0, 0.9, 0.3\mu$K. Dotted lines represent the distribution of τ under sharp reionization prior, while solid lines are obtained by marginalizing over z_r the joint distribution resulting from a double reionization analysis. At each sensitivity level, no significant difference between the width of the two distributions is apparent. However, while all marginalized distributions suitably peak on the *true* value $\tau = 0.17$, the single reionization distributions show a noise–dependent bias. For $\sigma_P = 3.0\,\mu$K, a single reionization prior leads to underestimating the optical depth. However, the statistical error is fairly wide and surpasses the bias. Decreasing σ_P, however, leads to an increase of the peak's τ value and, at the highest sensitivity considered, τ is overestimated by more than two standard deviations.

This behavior is easily explained considering how angular spectra respond to τ and z_r variations. As mentioned in Sec. 3.1.1, τ accounts for the number of CMB photons which undergo a scattering and directly affects the total amount of large scale polarization. Therefore, E–polarization (and TE–correlation) spectra corresponding to models with a different τ but the same z_r (and other relevant parameters) differ mainly in the height of the first reionization peak; on the other hand, a variation of z_r at fixed value of the optical depth also shifts the peak in l's. Fig. 3.5.2 shows the E-mode power spectra for a set of models with $\tau = 0.17$, including both single and double reionization histories, and two sharp reionization models corresponding to different τ (see

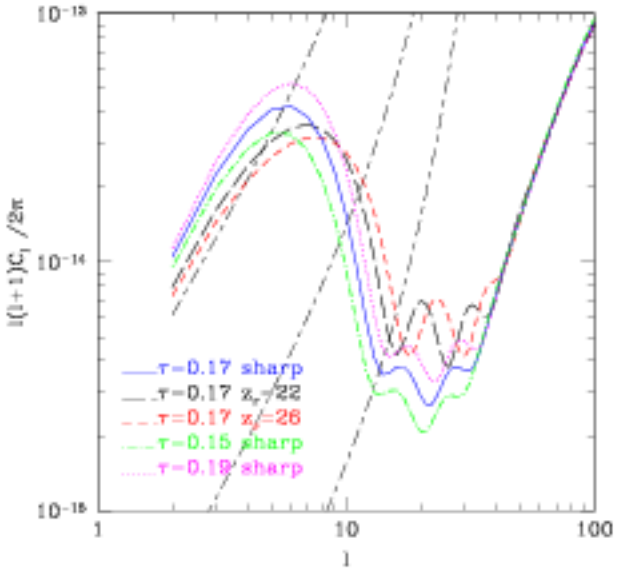

Figure 3.18: E–mode angular power spectra for three models with sharp reionization and $\tau = 0.15$, 0.17, 0.19 (dot–dashed, solid and dotted lines respectively)and two double reionization models with $\tau = 0.17$, $z_{ri} = 22$ (long–dashed lines), or $\tau = 0.17$, $z_{ri} = 26$ (short–dashed). At given value of the optical depth, spectra of models with double reionization fall below the APS of a sharp reionization with same τ for $l \lesssim$ 8–10 and above for $10 \lesssim l \lesssim 40$. The long–short dashed lines, instead, show the noise spectra for different pixel noises on polarization (top to bottom $\sigma_P = 3., 0.9, 0.3\,\mu$K), corrected for pixelization and beam smoothing.

figure's caption for details). As z_r increases, the first reionization peak for the models with $\tau = 0.17$ moves to higher l's and its height slightly decreases. The first multipoles of the double reionization models then approach those of a single reionization history with a lower optical depth, while in the range $8 \lesssim l \lesssim 20$ the same models resemble a sharp reionization with higher τ. At multipoles higher than ~ 30–40 differences between $C_{E,l}$ spectra for different reionization histories become negligible.

At SPOrt's noise level, the main contribution to determination of reionization parameters is provided by the first $7 - 8$ multipoles of the E–mode polarization spectrum (see Fig. 3.5.2). Trying to fit a single reionization history to a double reionization scenario therefore leads to underestimating τ. As noise decreases and multipoles in the range $10 \lesssim l \lesssim 20$ acquire greater weight, a double reionization history is misinterpreted as single reionization with a higher τ. This noise dependent bias is confirmed by quantitative results. In general, the bias has a greater impact for higher τ values and, at fixed τ, it increases with z_r. At noise levels accessible to current experiments the statistical error mostly exceeds the bias, and current τ estimates are reasonably safe, although would be systematically smaller than real values if the Universe had a double reionization. However, correctness of priors has greater weight for future experiments; wrong assumptions can lead to a τ overestimate exceeding 2–3 standard deviations.

Analyzing sharp reionization models assuming a two–reionization history produces an opposite behaviour. The same arguments as above shows that τ estimate becomes lower than the true value as sensitivity increases. In this case, however, the bias is less severe. In fact, a single reionization history can be thought as the limiting case of a double reionization model.

It must be stressed that these results concern the probability distribution of τ; analysis of a single map at fixed noise level may well result in τ estimates depending on priors, but this does not give any information on which prior is correct. In principle, the above shift can be used to test the nature of reionization by analyzing early and late outputs of a long lived experiment. This point requires two major remarks. Detection of a clear trend requires an increase in sensitivity between outputs by at least a factor of 3; such an improvement is unlikely within the planned lifetime of current experiments, but could be suggested as an option for future missions. Moreover, the observed trend is a global process; however only one realization of the Universe is accessible to current experiments. A diagnostic criteria for real maps is then required. We

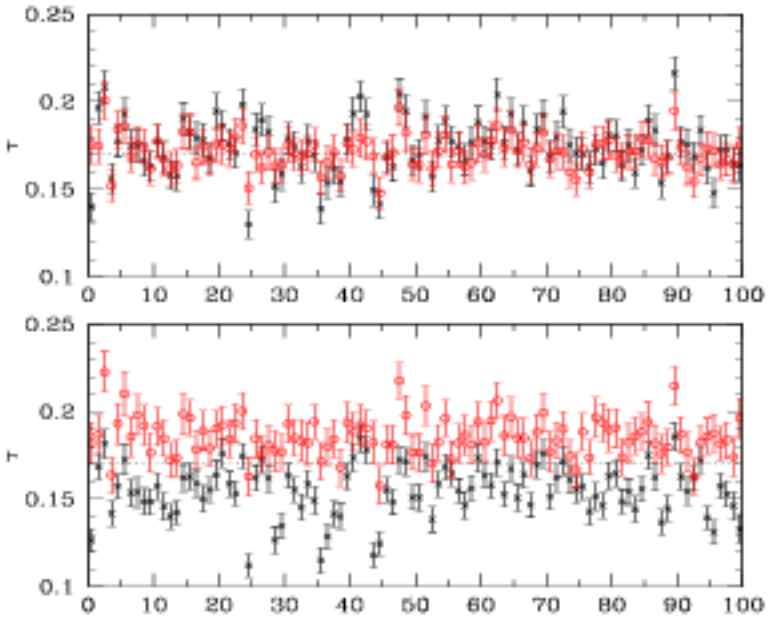

Figure 3.19: Top. Open circles: τ's from a WMAP+SPOrt–like experiment, with $\sigma_P = 0.80\mu$K in 5 years, for 100 realizations of model with $\tau = 0.17$ and $z_{ri} = 22$, assuming a double reionization prior. Crosses: average τ's obtained by dividing the whole data set into 10 subsets (6 months observation time). Error bars indicate the 1–σ c.l. Bottom. Same as Top panel but assuming a sharp reionization prior. Global (averaged) estimates are shifted up(down)–ward in respect to the actual τ value.

performed some more detailed tests on the latter point

(i) For each realization, the estimated optical depth at the three different sensitivities, under single (double) reionization prior, were labeled $\tau^s_{3.0}$, $\tau^s_{0.9}$ $\tau^s_{0.3}$, respectively ($\tau^d_{3.0}$, $\tau^d_{0.9}$ $\tau^d_{0.3}$).

(ii) Among all realizations, we selected only those in which the τ estimates, under single reionization prior, steadily increased at both reductions in noise level, i.e. $\tau^s_{3.0} < \tau^s_{0.9} < \tau^s_{0.3}$

(iii) The selected realizations were further pruned by requiring that the difference $\tau^s_{0.3} - \tau^s_{3.0}$ was greater than twice $\tau^d_{0.3} - \tau^d_{3.0}$.

The residual fraction, averaged over different fiducial models, holds $\sim 65\%$; although varying from $\sim 20\%$ in models with low optical depth and high reionization redshift, i.e. $\tau = 0.12$, $z_{ri} = 17$, to more than 90% in models with high optical depth ($\tau = 0.22$). Therefore, while this is not a definitive check, a progressive shift to higher values in τ estimates, when sensitivity increases and double reionization estimates remain $\sim$ stable, can be considered as a serious clue that a more refined description of reionization is needed.

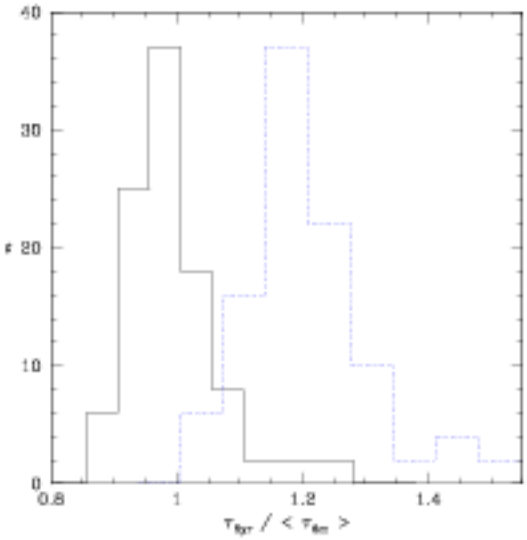

Figure 3.20: Distribution of the ratio between global and averaged τ estimates in 100 realizations of model $\mathcal{D}$, assuming either double realizations (solid line) or sharp reionization (dotted line) priors.

An additional test, for long lived experiments, is provided by dividing the global dataset into subsets corresponding to shorter observation periods, and comparing the τ value estimated by the analysis of the full dataset with the weighted average of the estimates in the smaller subsets. For reference purposes, we considered a SPOrt–like experiment lasting 5 years, and achieving a polarization pixel sensitivity $\sigma_P = 0.80\mu$K). Neglecting correlated noise effects and assuming that a full sky coverage requires 6 months of observations, the global data can be divided into 10 smaller subsets, characterized by $\sigma_P \sim 2.50\mu$K. We then compared the global τ estimate with the average of the estimates in the smaller subset. Repeating this analysis for 100 random realizations of model $\mathcal{D}$, we found global and averaged estimates to be consistent with each other and with the actual τ, when correct priors are made (top panel in Fig. 6). On the contrary, when sharp reionization is assumed, averaged estimates are systematically lower than the correct value, while global measurements overestimate it (bottom panel in Fig. 6). In these plots the effect is shown for 100 realizations of model, averaging among 10 noise realization for each model. Then, in Fig. 3.20, we plot the distribution of the ratio between the full 5–years estimate and the averaged 6–months estimates. Assuming a correct prior, such ratio averages $\tau_{6yr}/\langle\tau_{6m}\rangle = 0.99 \pm 0.07$, while for sharp reionization $\tau_{6yr}/\langle\tau_{6m}\rangle = 1.20 \pm 0.10$.

Focusing now on a double reionization prior, it is interesting to discuss the precision with which τ and z_r can be recovered. Probability distribution

Table 3.1: Average statistical errors and percent accuracy for the recovered parameters as a function of polarization sensitivity σ_P.

σ_P	Δ_τ	Δ_τ/τ	$\Delta_{z_{r1}}$	$\Delta_{z_{r1}}/z_{ri}$
3.0	0.037	.17	5.0	.19
0.9	0.012	.06	2.6	.08
0.3	0.008	.03	1.4	.04

for one parameter are obtained by marginalizing the joint probability density in the $\tau - z_r$ over the other parameter. Averaging over fiducial models the variances of these distribution provides a rough estimate of the capability of distinguishing different models, as a function of noise level and taking into account CV. Results are displayed in Table 3.1, together with estimates of relative accuracy, again averaged over fiducial models. For instance, two equal–τ models can be distinguished if their z_{ri} are farther apart than $\sim$ twice the value of $\Delta_{z_{r1}}$ shown.

Relative accuracy on τ is marginally better than that on z_{ri}, however the shape of the allowed region of $\tau - z_{ri}$ plane is typically *wider* in the τ direction, with respect to the precision with which each parameter can be fixed. In this sense, optical depth is determined with an higher accuracy than z_{ri}, *if priors on reionization history are adequate*.

Besides averages figures, some additional considerations can be made. At fixed noise level, models with higher τ generally allow for a better estimation of both parameters, due to their higher S/N ratio; among models with the same optical depth those with lower z_r have slightly sharper redshift distributions, as discrepancies between spectra tend to *saturate* for $z_{ri} \gtrsim 30 - 35$.

More in detail, Fig. 3.21 shows the distribution of z_{ri} for models with $\tau = 0.17$ (see caption for details). For $\sigma_P = 3.0\mu$K (left panel), the probability distributions overlap significantly, and z_{ri} cannot be recovered, while for $\sigma_P = 0.3\mu$K (right panel) they are almost completely distinguished. The middle panel displays an intermediate situation where models with single reionization can be distinguished from double reionization models with z_{ri} in the upper half of the allowed range (i.e. $z_{ri} \gtrsim 25$ for $\tau = 0.17$). Moreover, distributions for z_{ri} in double reionization models are wider by a factor ~ 2 than in single reionization models. Figure 3.22 shows that probability densities for τ in models with double reionization are indistinguishable at all sensitivities; thus, differences in z_{ri} do not greatly affect the capabilities of recovering τ, if correct priors are used. The

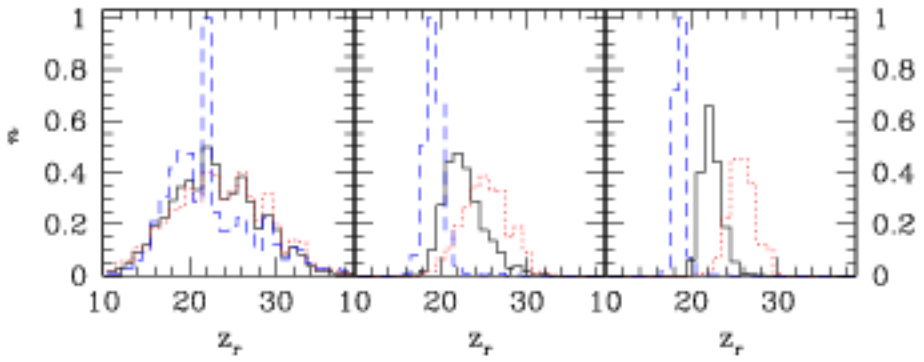

Figure 3.21: Distribution of maximum likelihood z_r, after marginalizing over τ, for 5000 realizations of models with $\tau = 0.17$ and sharp reionization (dashed lines), $z_{ri} = 22$ (solid lines) or $z_{ri} = 26$ (dotted lines). From left to right, panels refer to $\sigma_p = 3.0, 0.9, 0.3\,\mu$K, respectively.

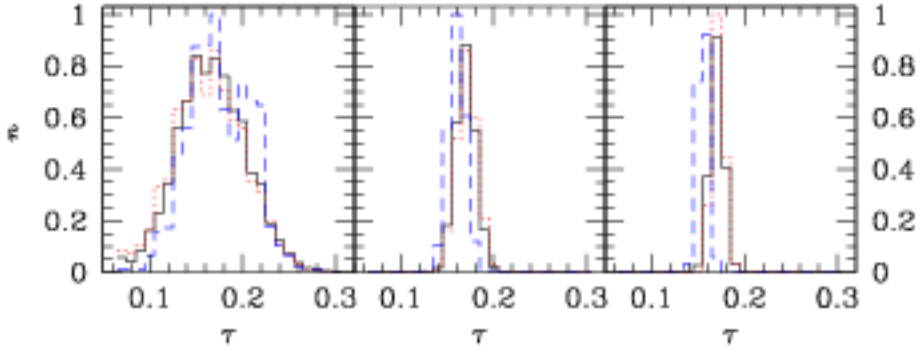

Figure 3.22: Same as Fig. 3.21, but for τ after marginalization over z_r.

sharp reionization model, instead, displays a bias, as discussed above. In this case, τ is progressively underestimated for decreasing σ_p, as a single reionization model is analyzed assuming a double reionization prior.

In Fig. 3.23 distributions of the optical depth for models with same z_{ri} but different τ are plotted. Even at the highest noise, some differences can be seen and for $\sigma_p = 0.9\,\mu$K the two distributions are clearly separated. In both cases, the correct τ is recovered. Figure 3.24, instead, shows results for z_{ri}. The probability functions of both models significantly overlap and correctly peak at the true value of the reionization redshift. Model with higher τ, however, is characterized by a sharper and better defined distribution, due to its higher S/N.

The discussion of this section can be summarized as follows. Wrong priors on reionization history may bias τ's estimates. This bias is particularly relevant when sharp reionization histories are fitted to simulated data corresponding

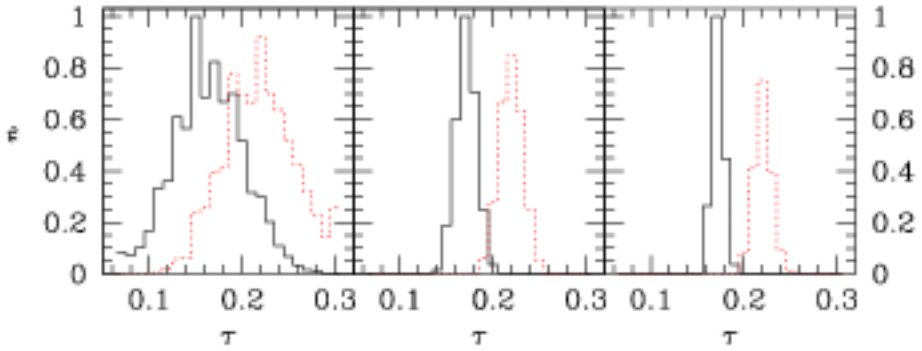

Figure 3.23: Same as Fig. 3.22, but for models with same $z_{ri} = 26$ and $\tau = 0.17$ or $\tau = 0.22$ (dotted lines).

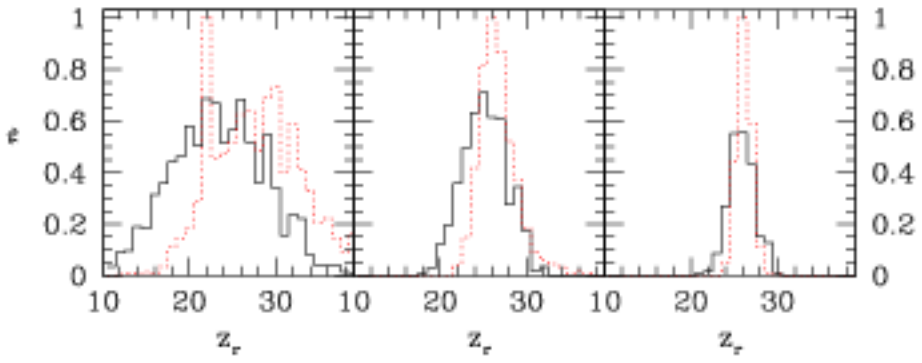

Figure 3.24: Same as Fig. 3.23, but for z_r.

to double reionization models. At current noise levels, statistical uncertainty exceeds the bias. As sensitivity increase, so does the relevance of the bias; if noise is decreased by an order of magnitude, discrepancy between estimated and true value of the optical depth can exceed 3 standard deviations.

If correct priors are assumed, a polarization sensitivity of $\sigma_P = 3.0\,\mu$K allows to constrain the total optical depth with average accuracy of $\sim 17\%$; no further parameter can be simultaneously constrained. Increasing the sensitivity by an order of magnitude allows for a simultaneous detection of τ and z_{ri}, while intermediate noise level allows to discriminate a single reionization history from double reionization with high z_{ri} (e.g., $z_{ri} \gtrsim 25$ for $\tau = 0.17$). Moreover, the actual z_{ri} value only slightly affects the estimate of τ. On the contrary, capability of determining z_{ri} depends on the actual τ value.

3.6 Discussion

Cosmic Microwave Background measurements provide a complementary window to infrared observations of the reionization epoch. In particular, both single and complex reionization histories leave a clear imprint on the low–multipoles of $C_{E,l}$ spectra, which can be inspected through large angle polarization measures.

Before the last year, several observational and theoretical works lead to conclude that the Thomson optical depth to reionization $\tau \lesssim 0.05$. Large angle polarization would then be difficult to detect. This fairly established picture was drastically changed by release of first year–measurements by the WMAP satellite, which estimated $\tau = 0.16 \pm 0.04$ in a *model independent* way, from TE–correlations (kogut 2003).

However, alternative analysis methods (Spergel 2003) gave different values, such as $\tau = 0.17 \pm 0.07$ or even $\tau = 0.12 \pm 0.06$, when data on Large Scale Structure and the Lyα forest were taken into account. WMAP's data, then, clearly showed that the optical depth is higher than expected, however the actual value of τ is still uncertain. This picture has been further muddled by recent results (Hansen et al. 2004) indicating significant, i.e. at more than 2σ level, discrepancies between parameter estimates in Southern and Northern hemispheres. In particular, in Southern hemisphere $\tau = 0.24 \pm 0.07$, while in Northern one only an upper limit $\tau < 0.08$ (95 % c.l.) is found.

Considering also results on high–z QSO's, indicating the presence of neutral Inter Galactic Medium at $z \sim 6-7$, confirmation of WMAP's results acquires a critical significance. With its high accuracy measurements of large angle CMB polarization, the SPOrt experiment will play a relevant role in further investi-

gations of reionization history (Colombo and Bonometto 2003). Assuming an optical depth $\tau = 0.17$, SPOrt will provide an high significance (3σ) detection of τ with a probability of 95%. On the contrary, finding a value compatible with vanishing optical depth at 2σ level, would allow to rule out $\tau \geq 0.17$ with 99% accuracy. In any case, correlation of SPOrt and WMAP measurements allows for measurements of $C_{TE,l}$ free from spurious instrumental correlations.

If the high value of τ is eventually confirmed, reconciling CMB and QSO's observations requires to abandon simple models of sharp reionization in favour of more complex reionization histories. Current measurements, however, do not reach sensitivities allowing to reconstruct the additional details characterizing these models. An order of magnitude increase in sensitivity is required in order to constrain reionization history defined by 2–3 parameters, while a further increase by a factor of ~ 10 allows to fully assess the effect of generic reionization history on E–mode polarization. At this sensitivity, $C_{E,l}$ estimates are dominated by CV up to multipoles $l \sim 50$, while reionization histories affect multipoles $l \lesssim 40$, barring patchiness effects relevant on scales $l \gtrsim 2000$. Further increases in sensitivity would not strongly affect the quality of constraints on reionization models.

However, with better accuracy, a careful modeling of reionization acquires a critical relevance. Wrong priors, in particular assuming a sharp reionization in the analysis of double, or complex, reionization histories, bias τ estimates. For current measurements, the bias is expected to be smaller that the statistical uncertainty (Colombo et al. 2005), and results can be considered safe. As sensitivity increases, however, the bias becomes stronger, and correct and estimated values of the optical depth may disagree at more than 3σ level. Working around such bias may prove difficult: for some models of double reionization, wrong priors are reflected by well defined trend of τ estimates as sensitivity increases. Detection of this trend in experimental data is a strong hint that a more accurate modeling of reionization is in order.

Chapter 4

Dynamical and coupled Dark Energy vs. CMB data

In this chapter we perform a systematic fit of WMAP data to these different cosmologies: dDE, ccDE, vcDE, and ΛCDM. For the first 3 of them a SUGRA self-interaction potential will be taken (Brax & Martin 1999, 2000; Brax, Martin & Riazuelo 2000); its expression is given in Sec. 2, together with essential information on coupled and uncoupled DE models. Further information on coupled models can be found, *e.g.*, in Colombo et al. (2004).

The fit is performed by using a MCMC (MonteCarlo Markov Chain) algorithm, in the same way as the WMAP team fit the ΛCDM model. In Sec. 3, we describe the fitting procedure. In the case of that model we re–obtain their results.

The number of parameters to be fitted depends on the nature of the model. ΛCDM and vcDE models have the same number of parameters. In dDE models there is one extra parameter and ccDE models have a further parameter in respect to the previous cathegory. In evaluating the success of a fit, however, the number of parameters is taken into account. In Sec. 4 we perform sich comparison and in Sec. 5 we draw some conclusions.

4.1 Comparison with WMAP data through a MCMC algorithm

WMAP data have been extensively used to constrain cosmological parameters. They are high precision estimates of the anisotropy power spectrum C_l^T up to $l \sim 900$, as well of the TE correlation power spectrum C_l^{TE} up to $l \sim 450$. We shall fit these data to possible cosmologies, by considering a parameter space of 6 to 8 dimensions. A grid-based likelihood analysis would require a huge

CPU time and we use a Markov Chain Monte Carlo (MCMC) approach, as it has become customary for CMB analysis (Christensen et al. 2001, Knox et al. 2001, Lewis et al. 2002, Kosowski et al. 2002, Dunkley et al. 2004).

To this aim, as in any attempt to fit CMB data to models, a linear code providing C_l's is needed. Here we use our optimized extension of CMBFAST (Seljak and Zaldarriaga 1996), able to inspect also ccDE and vcDE cosmologies. The likelihood of each model is then evaluated through the publicly available code by the WMAP team (Verde et al. 2003) and accompanying data (Hinshaw et al. 2003, Kogut et al. 2003).

A MCMC algorithm samples a known distribution $\mathcal{L}(\mathrm{x})$ by means of an arbitrary trial distribution $p(\mathrm{x})$. Here $\mathcal{L}$ is a likelihood and x is a point in the parameter space. The chain is started from a random position x and moves to a new position x', according to the trial distribution. The probability of accepting the new point is given by $\mathcal{L}(\mathrm{x}')/\mathcal{L}(\mathrm{x})$; if the new point is accepted, it is added to the chain and used as the starting position for a new step. If x' is rejected, a replica of x is added to the chain and a new x' is tested.

In the limit of infinitely long chains, the distribution of points sampled by a MCMC describes the underlying statistical process. Real chains, however, are finite and convergence criteria are critical. Moreover, a chain must be required to fully explore the high probability region in the parameter space. Statistical properties estimated using a chain which has yet to achieve good convergence or mixing may be misleading. Several methods exist to diagnose mixing and convergence, involving either single long chains or multiple chains starting from well separated points in the parameter space, as the one used here. Once a chain passes convergence tests, it is an accurate representation of the underlying distribution.

In order to ensure mixing, we run six chains of ~ 30000 points each, for each model category. We diagnose convergence by requiring that, for each parameter, the variances both of the single chains and of the whole set of chains (W and B, respectively) satisfy the Gelman & Rubin test (Gelaman & Rubin 1992), $R < 1.1$ with:

$$R = \frac{[(N-1)/N]W + (1+1/M)B}{W} \quad . \tag{4.1}$$

Here each chain has $2N$ points, but only the last N points are used to estimate variances, and M is the total number of chains. In most model categories considered, we find that the slowest parameter to converge is λ.

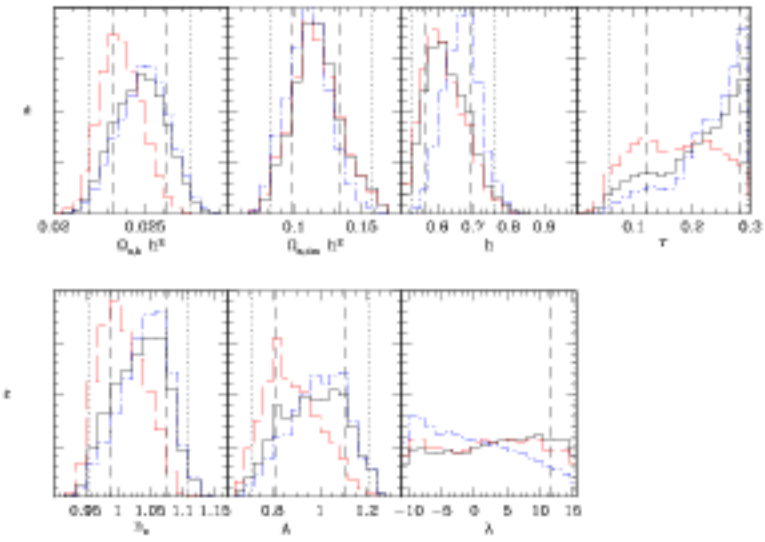

Figure 4.1: Marginalized distributions for the 7–parameters SUGRA model with no priors (solid lines), BBNS prior (long dashed) or HST prior (dot–dashed). Short dashed (dotted) vertical lines show the boundaries of 68.3 % c.l. (95.4 % c.l.) interval; for λ only upper limits are shown.

4.2 Results

The basic results of this work are shown in the Tables 4.1–4.3. For each model category we provide the expectation values and the variance of each parameter, as well as the values of the parameters of the best fitting models. The corresponding marginalized distributions are plotted in figures 4.1–4.3, while joint 2D confidence regions are shown in figures 4.4–4.6.

The values of χ^2 can also be compared, taking into account the number of degrees of freedom. This is shown in Table 4.4. The smallest χ^2 is obtained for the uncoupled SUGRA model, which performs slightly better than ΛCDM.

Tables 1 and 2 and the corresponding figures, *concerning uncoupled or constant–coupling* SUGRA models, show that WMAP data scarcely constrain $\lambda = \log(\Lambda/\mathrm{GeV})$, allowed to vary from ~ -12 to 16. On the contrary, in the case of a ϕ^{-1} coupling, loose but precise limitations on λ are set, as is shown in Table 3. In the presence of this coupling, the 2–σ Λ–interval ranges from ~ 10 to $\sim 3 \cdot 10^{10}$GeV.

These constraints apparently arise from polarization data.: when DE begins to affect cosmic expansion, the ϕ evolution acts on DE density and pressure, as well as on its coupling, and requires an l–dependence of multipole amplitudes ablt to meet data only for a limited range of Λ values. This can be noticed in Figures 4.7 and 4.8, where the best–fit C_l^T and C_l^{TE} spectra for all best–fit

Table 4.1: SUGRA parameters for dDE models: for each parameter x, the expectation value $\langle x \rangle$, its variance σ_x, and its maximum likelihood value x_{max}, in the 7–dimensional parameter space, are shown.

x	$\langle x \rangle$	σ_x	x_{max}
$\Omega_{o}_b h^2$	0.025	0.001	0.026
$\Omega_{o}_{dm} h^2$	0.12	0.02	0.11
h	0.63	0.06	0.58
τ	0.21	0.07	0.28
n_s	1.04	0.04	1.08
A	0.97	0.13	1.11
λ	3.0	7.7	13.7

Table 4.2: SUGRA parameters for ccDE models; the parameter space is 7–dimensional and parameter are shown as in the previous Table.

x	$\langle x \rangle$	σ_x	x_{max}
$\Omega_{o}_b h^2$	0.024	0.001	0.024
$\Omega_{o}_{dm} h^2$	0.11	0.02	0.12
h	0.74	0.11	0.57
τ	0.18	0.07	0.17
n_s	1.03	0.04	1.02
A	0.92	0.14	0.93
λ	-0.5	7.6	8.3
β	0.10	0.07	0.07

Table 4.3: SUGRA parameters for vcDE models. At variance from other model categories, λ here is constrained. Parameter values are shown as in Table 1.

x	$\langle x \rangle$	σ_x	x_{max}
$\Omega_{o}_b h^2$	0.025	0.001	0.026
$\Omega_{o}_{dm} h^2$	0.11	0.02	0.09
h	0.93	0.05	0.98
τ	0.26	0.04	0.29
n_s	1.23	0.04	1.23
A	1.17	0.10	1.20
λ	4.8	2.4	5.7

Table 4.4: Goodness of fit. We lists the number of degrees of freedom (d.o.f.), the reduced χ^2_{eff}, and the corresponding probability of the best–fit model. ΛCDM models have 1342 degrees of freedom, uncoupled and vcDE models have 1341, while ccDE models have 1340.

	χ^2_{eff}	prob.
dDE	1.062	5.2 %
ccDE	1.066	4.7 %
vcDE	1.074	2.9 %
ΛCDM	1.066	4.7 %

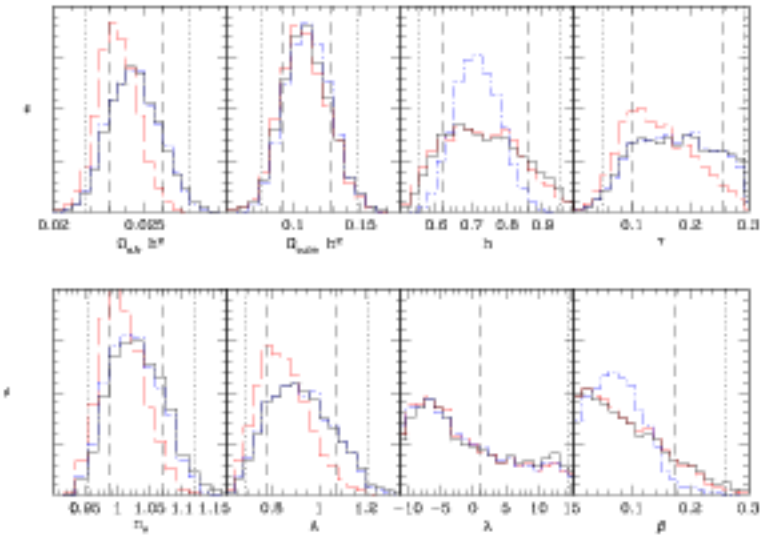

Figure 4.2: As Fig. 4.1 but for the 8–parameters ccDE model. For λ and β only the upper c.l. boundaries are shown.

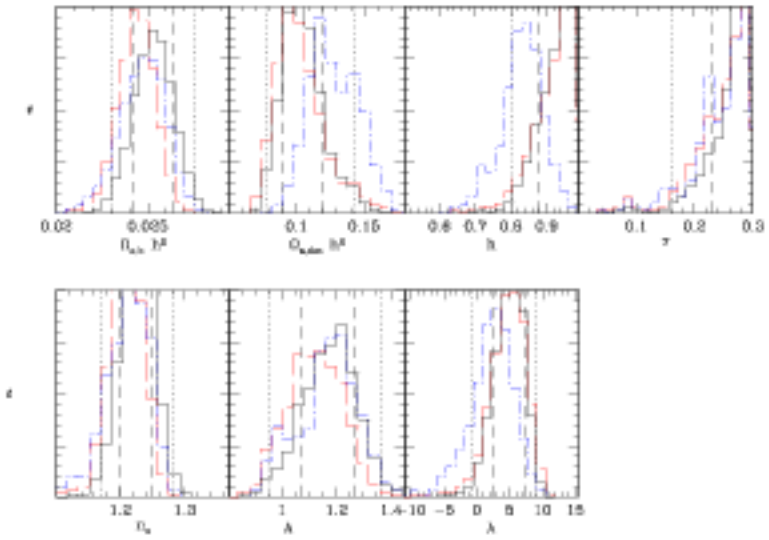

Figure 4.3: As Fig. 4.1 but for the 7–parameters vcDE model.

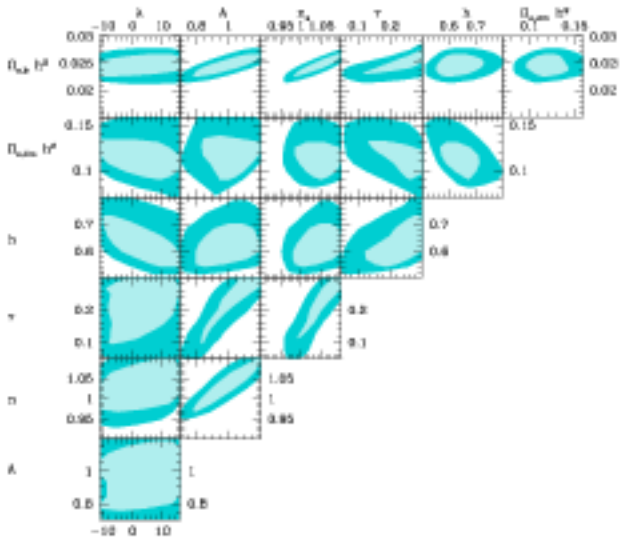

Figure 4.4: Joint 2D constraints for SUGRA models. Light (dark) shaded areas delimit the region enclosing 68.3 % (95.4 %) of the total points.

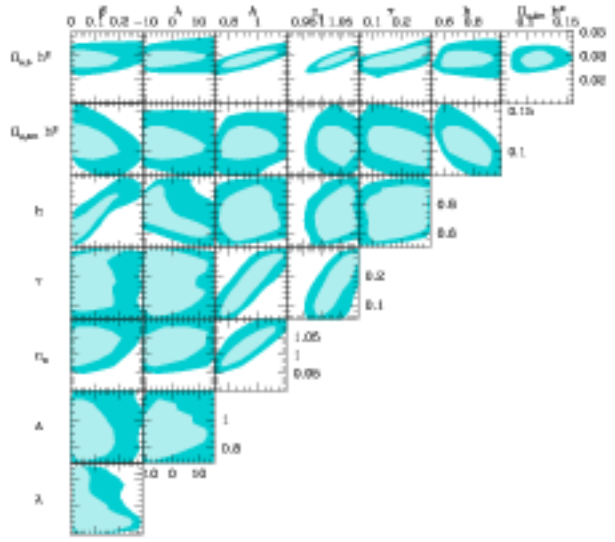

Figure 4.5: As Fig. 4.4 but for ccDE models.

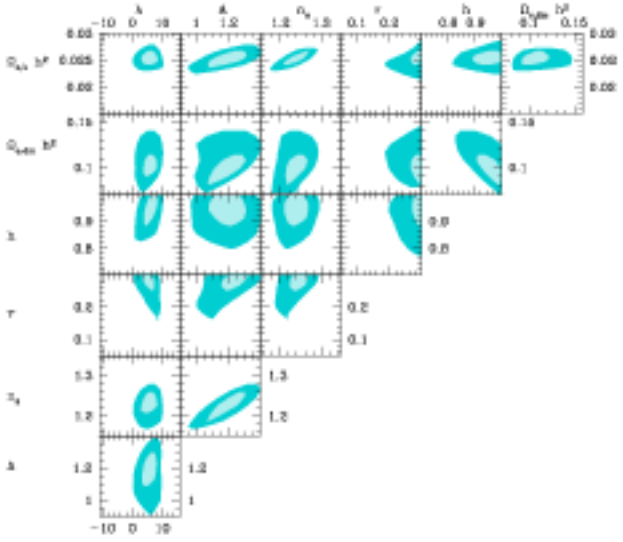

Figure 4.6: As Fig. 4.4 but for vcDE models. Here, cosmological parameters are more stringently constrained than in other models.

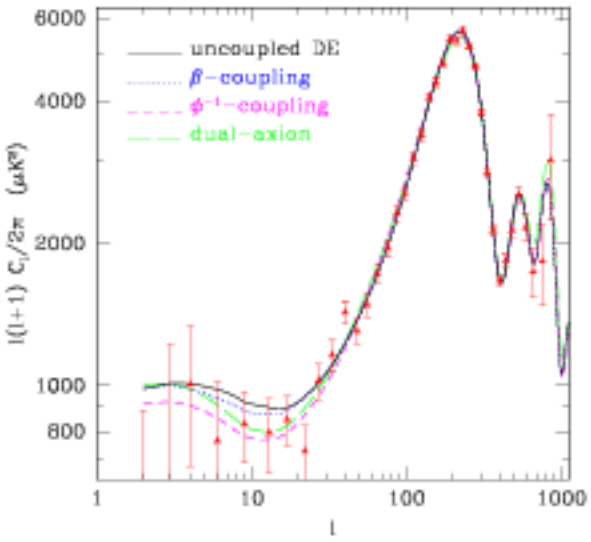

Figure 4.7: C_l^T spectra for the best fit SUGRA (solid line), ccDE (dotted line) and vcDE (dashed). Dual-axion (dot-dashed) models are also shown; they can be considered a particular case within vcDE models, for which $10 \leq \lambda \leq 10.5$ (see text). The binned first-year WMAP data are also plotted.

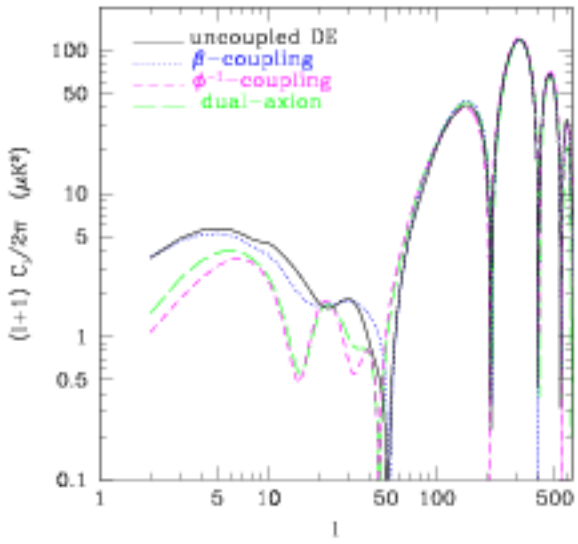

Figure 4.8: Best fit C_l^{TE} spectra.

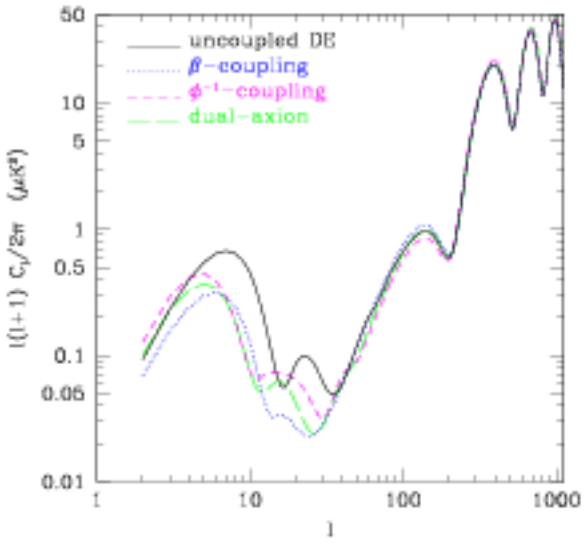

Figure 4.9: Best fit C_l^{EE} spectra.

models (apart of ΛCDM) are compared.

Fig. 4.7 also shows why no model neatly prevails. At large l all best–fit models yield similar behaviors. Discrimination could be improved only through better large angular scale observations, especially for polarization, able to reduce errors on small–l harmonics.

4.3 Discussion

4.3.1 Uncoupled SUGRA models

SUGRA *uncoupled* models are found to be consistent with WMAP data. The ratio $w = p/\rho$, for these models is typically -0.80 at $z = 0$. However, they exhibit a fast variation of w, which is already ~ -0.6 at $z \sim 1$–2. Such a decrease, however, does not cause a conflict with data and *these models perform even better than ΛCDM.*

We also considered the effect of adding some priors. For uncoupled or constant–coupling SUGRA models, the analysis in the presence of priors leads to analogous conclusions. There are however variations in the estimate of cosmological parameters. First, the opacity τ is pushed to values exceeding the ΛCDM estimates (see also Corasaniti at al. 2004). This can be understood in two complementary ways: (i) ISW effect is stronger for dDE than for ΛCDM, as the field ϕ evolves during the expansion; hence, DE effects extend to a greater redshift, increasing C_l^{TT} values in the low–l plateau. To compensate this effect the fit tends to shift n_s greater values. Owing to the τ–n degeneracy, this is

then balanced by increasing τ. (ii) It must also be reminded that the expected TE correlation for dDE, at low l, is smaller (Colombo et al. 2003). Then, when TE correlation data is included, a given correlation level is fit by a greater τ. In any case, however, $\tau \sim 0.07$ keeps consistent with data within less than 2–σ's.

Greater τ's affect also $\Omega_b h^2$ estimates, whose best–fit value is then greater, although consistent with ΛCDM within 1–σ. Adding a prior on $\Omega_b h^2 = 0.0214 \pm 0.0020$ lowers h, slightly below HST findings, but still well within 1–σ. We therefore consider the effect of adding a prior also on h.

The effects of these priors are shown in Figures 4.1 and 4.2. The new distributions are given by the dashed red line (prior on $\Omega_b h^2$) and the dot–dashed blue line (prior on h). The former prior affects mainly τ and n_s: τ and n_s are lowered to match WMAP's findings, the high tail of τ distribution is partly suppressed. The physical analysis of primeval objects causing reionization (Ciardi et al. 2003, Ricotti et al. 2004). which are still allowed but certainly not *required*.

4.3.2 cc**DE SUGRA** models

The latter prior favors greater h values. In the absence of coupling, this favors low–λ models, closer to ΛCDM. In fact, the sound horizon at decoupling is not affected by the energy scale Λ, while the comoving distance to last scattering band is smaller for greater λ's. Then, for greater λ's lower h values are favored, so to meet the first peak. In the presence of coupling, there is a simultaneous effect on β: greater β's yield a smaller sound horizon at recombination, so that the distribution on h is smoother.

A previous analysis of WMAP limits on constant coupling models had been carried on by Amendola & Quercellini (2003). Their analysis concerned potentials V fulfilling the relation $dV/d\phi = BV^N$, with suitable B and N. Furthermore, they assume that $\tau \equiv 0.17$. Our analysis deals with a different potential and allows more general parameter variations. The constraints on β we find are less severe. It must be however outlined that $\beta 0.1$–0.2 seem however forbidden by a non–linear analysis of structure formation (Macciò et al. 2004).

4.3.3 vc**DE SUGRA** models

The main peculiarity of ϕ^{-1}–models is that, although the ξ^2 value is not much worsened in respect to other cases, parameters are more strongly constrained in this caseq. This is evident in Fig. 4.6. In particular, at variance from the former case, the energy scale Λ is significantly constrained.

Several other parameters are constrained, similarly to coupled or uncoupled SUGRA models. What is peculiar of ϕ^{-1}–models is the range of h values which turn out to be favored. The best–fit 2–σ interval does not extend much below 0.85.

This is a problem for these models in their present form. Should new data support a greater h value, vcDE models would however be favored. Quite in general, however, we must remind that vcDE models were considered here only in association with a SUGRA potential; vcDE models with different potentials can possibly agree with a smaller h.

4.3.4 Dual axion models

A particular but significant case, among vcDE models, are dual axion models (DAM; for a detailed analysis see Mainini & Bonometto 2004, Colombo et al 2004).

These models arise from a generalization of the PQ solution of the strong–CP problem (Peccei & Quinn 1977), obtained by replacing the NG potential acting on a complex scalar field Φ with a quintessence potential admitting a tracker solution. While, in the usual PQ approach and its generalization, only the phase θ of the Φ field is physically sgnificant, in the DAM also its modulus ϕ is physically observable. In both cases, quanta of the θ field are axions and, if DM is made of axions, its density parameter $\Omega_{a,m}$ is set either by the F_{PQ} parameter, in the NG potential, or by the energy scale Λ, in the quintessence potential. In the latter case, therefore, both DM and DE features follow from fixing the single parameter Λ.

A detailed analysis of DAM shows that it belongs to the set of vcDE cosmologies; its main peculiarity is that λ and $\Omega_{a,m}$ are no longer independent degrees of freedom. Henceforth, this model is strongly constrained and depends on the same number of parameters as SCDM. By varying $\Omega_{a,m}$ in its physical range, λ keeps however close to 10. This great value of λ therefore causes a conflict with the observed h range. All previous comments on vcDE models however hold, while it is also possible that extra contribution to DM, arising from topological singularities expected in axion theories, can ease the h problem.

4.4 Conclusions

The first evidences of DM are fairly old; they date some 70 years ago. However, only in the late Seventies limits on CMB anisotropies showed that non–baryonic

DM had to be dominant. DE can also be dated back to Einstein's *cosmological constant*, although only SN Ia data revived it, soon followed by data on CMB and deep galaxy samples.

The main topic of this chapter is the fit of WMAP data with various DE models: ΛCDM, SUGRA dynamical and constant coupling DE models, as well as variable coupling DE models. In the last model DM and DE are coupled in a non–parametric way, with $C = \phi^{-1}$.

The fits of WMAP data to these models yield similar χ^2's. At variance from other model categories, however, in vcDE models, CMB data constrain Λ. This is due to the stronger effects of ϕ variations on the detailed ISW effect, as they affect both DE pressure and energy density, as well as DE–DM coupling. In principle, this strong impact of ϕ variation could badly disrupt the fit and make vcDE models significantly farther from data. It is noticeable that this does not occur.

The success of vcDE models would be complete if the favored range of values of the Hubble parameter ($h \sim 0.8$–1) could be slightly lowered. This range is however obtained just for a SUGRA potential. Furthermore, primeval fluctuations were assumed to be strictly adiabatic while, in axion models, a contribution from isocurvature modes can be expected. This could legitimately affect the apparent position of the first peak in the anisotropy spectrum, so completing the success of the model, in a fully self–consistent way.

Chapter 5

The Sky Polarization Observatory

This chapter is a sort of parenthesis in this thesis. It concerns an experiment to which we took part, dubbed SPOrt (Cortiglioni et al. 2004 [34], which was suspended when ASI (the Italian Space Agency) unmotivately stopped its financial support. The experiment had been selected by ESA, in 1997, to be flown on board the International Space Station (ISS) during the Early Utilization Phase. The research team was based on an international collaboration of Institutes, headed by the IASF–CNR in Bologna, to whom ASI initially offered its finantial support.

The payload, shown in Fig. 5.1, was built to house four corrugated feed horns feeding a 22, a 32, and a pair of 90 GHz channels providing direct measurements of the Q and U Stokes parameters.

The experiment took into account that the ISS orbit is tilted by 51.6°, with respect to the Celestial equator, and is characterized by a period of about 5400 s and a precession of about 70 days. This allowed a sky coverage of $\sim 80\%$, with a sky scanning pattern shown in Fig. 5.2. Full coverage of the accessible region required 70 days. In Fig. 5.2 a map of the time spent over each pixel, of about 7° (HEALPix[1] parameter $N_{side} = 8$), is also shown.

SPOrt primary goals initially consisted in the detection of CMB polarization on large angular scales, and in the mapping of Galactic synchrotron emission. The former task asked for both a nearly all-sky survey and a multifrequency approach to control possible contaminations from Galactic foregrounds; the latter was expected from the channels at 22 and 32 GHz. The experiment's main features, summarized in Table 5.1, had been accurately chosen to allow the accomplishment of these objectives.

[1] http://www.eso.org/science/healpix

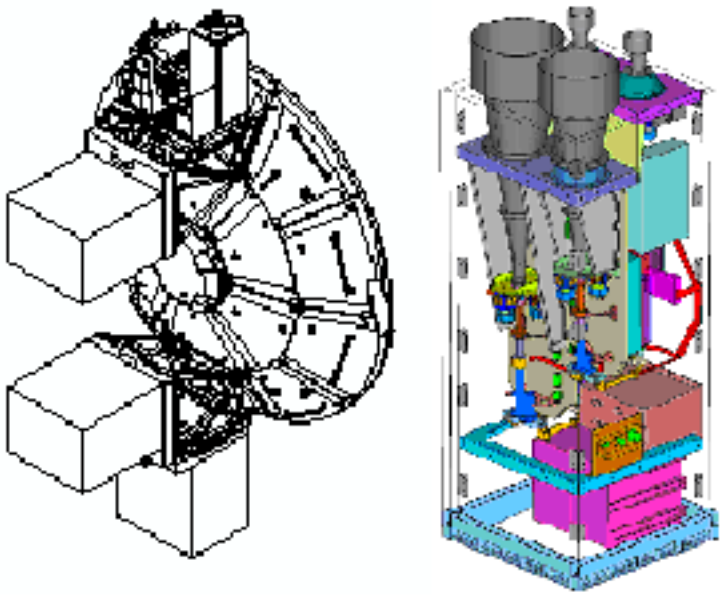

Figure 5.1: Left: The SPOrt position on the Columbus External Payload Facility, onboard the ISS (courtesy by Alenia Spazio). Right: Expansion of the SPOrt payload. (From Cortiglioni et al. 2004 [34])

After WMAP first year release, apparently indicating a high value of the cosmic opacity to CMB photons, τ, the detection of a polarization signal appeared almost granted. In principle, SPOrt could not only be the first independent confirm of WMAP findings, but, being expressely build to detect polarization, was also free of quite a few biases, which made (and still make) WMAP detection somehow questionable.

From this point of view it could successfully rival even with the PLANCK project, which will also detect the polarization signal, but whose design was only lately modified to this aim.

In particular, SPOrt aimed at the direct and simultaneous measurement of both Stokes parameters Q and U, optimizing the observing time efficiency, a remarkable improvement compared to other schemes providing either Q or U and thus reducing it by a factor 2.

The SPOrt expected sensitivity to CMB, resulting from the combination of the four channels and taking into account the worsening due to foreground subtraction [42], is reported in Table 5.2.

In the following section we shall provide further details on SPOrt planned features, refraining to add any further comment on the reasons leading to its suppression, which should be trasparent from what we outlined here above.

Table 5.1: SPOrt main features: N_{pix} is the number of FWHM pixels covered by SPOrt (80% sky coverage), σ_{1s} is the instantaneous sensitivity (1 second), and σ_{pix} is the pixel sensitivity for a two–year mission.

ν (GHz)	channels (#)	BW	FWHM (°)	Orbit Time (s)	N_{pix}	σ_{1s} (mK $s^{1/2}$)	σ_{pix} (μK)
22	1					0.5	1.6
32	1	10%	7	5400	660	0.5	1.6
90	2					0.57	1.8

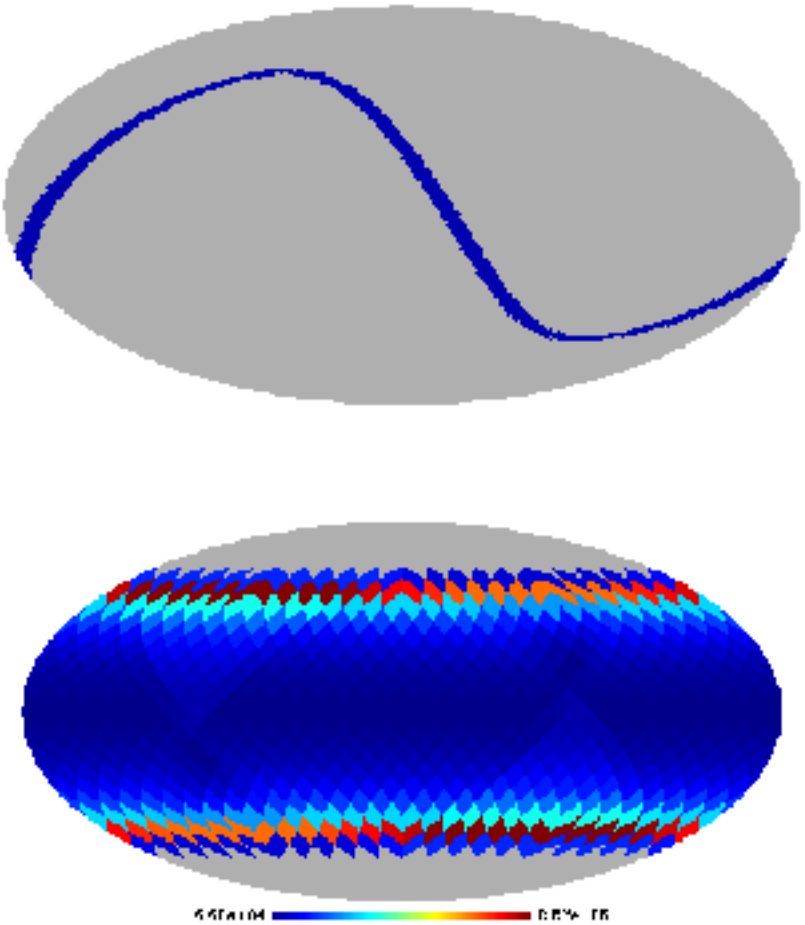

Figure 5.2: Top: The sky, in Celestial coordinates, as scanned by SPOrt in few orbits. Bottom: Pixel observing time (seconds) for two years of data taking. The pixel size is about 7° (HEALPix resolution $Nside = 8$).(From Cortiglioni et al. 2004 [34])

Table 5.2: SPOrt sensitivity to CMB, in thermodynamic temperature, combining the four channels and including Galactic synchrotron subtraction, for a two–year mission.

σ_{1s} ($\mathrm{mKs}^{1/2}$)	σ_{pix} (μK)	$\sigma(\mathrm{P}_{1ms})$ (μK)
0.53	1.7	0.15

5.1 Instrument Design and Analysis

The main concern in designing an experiment to measure CMB polarization is the low level of the expected signal (1–10% of the already tiny temperature anisotropies, depending on the scale), requiring specific instrumentation.

SPOrt design had been optimized with respect to systematics generation, long term stability and observing time efficiency.

The following solutions were implemented while designing the polarimeter:

- correlation architecture to improve stability;
- correlation of the two circularly polarized components E_L and E_R to directly and simultaneously measure both Q and U from the real and imaginary parts of the correlation, respectively,

$$Q \propto \Re(E_R E_L^*); \qquad U \propto \Im(E_R E_L^*) \tag{5.1}$$

  while keeping 100% efficiency;
- detailed analysis of the correlation scheme to identify *critical* components and set their specifications in order to keep the systematics at a level suitable to measure CMB polarization;
- on axis simple optics (corrugated feed horns) to minimize the spurious polarization induced by both the f pattern (see [23] for its definition) and the CMB temperature anisotropy on the beam scale.

Implementing these features involved the custom development of components when state–of–the–art was not compliant with SPOrt requirements.

Radiometer sensitivity was governed by the equation [154]

$$\Delta T_{1ms} = \sqrt{\frac{k^2 T_{sys}^2}{\Delta\nu\, t} + T_{offset}^2 \left(\frac{\Delta G}{G}\right)^2 + \Delta T_{offset}^2}\,, \tag{5.2}$$

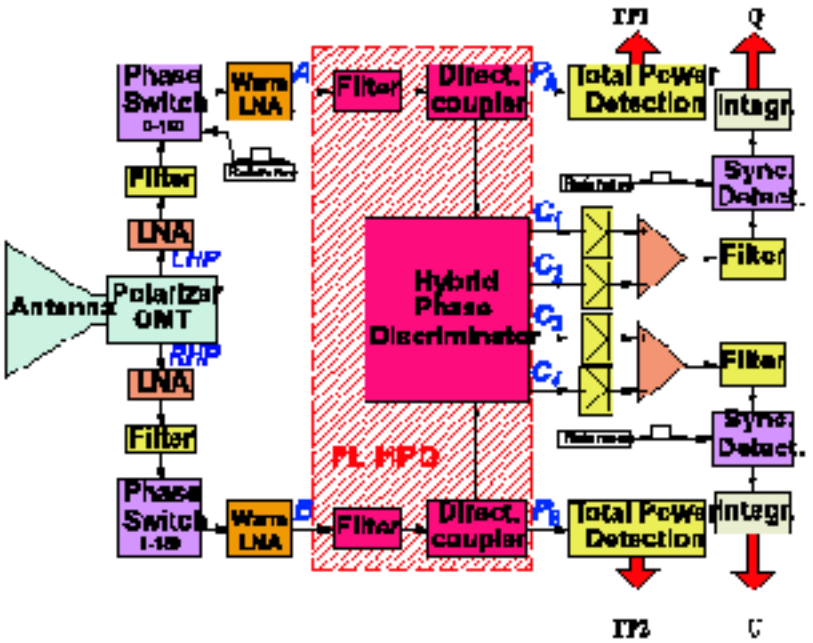

Figure 5.3: Schematic block diagram of the SPOrt radiometers. Polarizer and OMT extract the two circularly polarized components LHP and RHP collected by the horn. After amplification, the correlation unit (based on a Hybrid Phase Discriminator [?]) provides directly both Q and U.(From Cortiglioni et al. 2004 [34])

which provides hints on parameters critical to systematics minimization. Here T_{sys}, T_{offset} and ΔT_{offset} represent the system temperature, the offset equivalent temperature and its fluctuation, respectively; G is the radiometer gain, t the integration time, $\Delta\nu$ the radiofrequency bandwidth and $k \simeq 1$ a constant depending on the radiometer type.

The first term in eq. 5.2 represents the white noise of an ideal and stable radiometer, while the second and the third term represent the contributions of gain and offset fluctuations generated by instrument instabilities. It is clear that the noise behaviour can be kept close to the ideal (white) case provided the offset is kept under due control.

A scheme of the SPOrt radiometers is shown in Fig. 5.3. The Polarizer and the OMT extract the two circularly polarized components E_L and E_R collected by the dual–polarization feed horn. After amplification, the two components are correlated by the Correlation Unit (CU), consisting of an Hybrid Phase Discriminator (HPD), four diodes and two differential amplifiers. In details,

the HPD generates the four outputs:

$$C_1 \propto E_L + E_R \tag{5.3}$$
$$C_2 \propto E_L - E_R \tag{5.4}$$
$$C_3 \propto E_L + j\,E_R \tag{5.5}$$
$$C_4 \propto E_L - j\,E_R \tag{5.6}$$

which are square–law detected by the four diodes

$$|C_1|^2 \propto |E_L|^2 + |E_R|^2 + 2\Re(E_R E_L^*) \tag{5.7}$$
$$|C_2|^2 \propto |E_L|^2 - |E_R|^2 - 2\Re(E_R E_L^*) \tag{5.8}$$
$$|C_3|^2 \propto |E_L|^2 + |E_R|^2 + 2\Im(E_R E_L^*) \tag{5.9}$$
$$|C_4|^2 \propto |E_L|^2 - |E_R|^2 - 2\Im(E_R E_L^*). \tag{5.10}$$

The differences performed by the two differential amplifiers provide

$$\begin{array}{rcccl} |C_1|^2 - |C_2|^2 & \propto & \Re(E_R E_L^*) & \propto & Q \\ |C_3|^2 - |C_4|^2 & \propto & \Im(E_R E_L^*) & \propto & U \end{array} \tag{5.11}$$

allowing the simultaneous measurement of the two Stokes parameters Q & U. With this implementation, an error on the difference between E_R and E_L during signal propagation within the instruments, simply results in a polarization angle rotation, well recoverable in the calibration procedure. On the contrary, measuring linear polarization by correlating the two linear polarizations E_x, E_y would only provide one Stokes parameter (U). Moreover, errors in the phase difference lead to a combination of U and V in the output. Therefore, great care was needed in equalizing the path of the two components.

The analysis of radiometers had shown that the prominent sources for offset generations are found in CU and the antenna system (horn, polarizer and OMT). In turn, antenna details were critical for a successful destriping.

The contribution to the offset coming from the antenna system is given by [23]:

$$T_{\rm offset} = SP_{\rm OMT}\left(T_{\rm sky} + T_{\rm noise}^{\rm Ant}\right) + SP_{\rm pol}\left(T_{\rm sky} + T_{\rm noise}^{\rm horn} - \frac{T_{\rm ph}^{\rm pol}}{\eta}\right), \tag{5.12}$$

where $T_{\rm sky}$ is the signal coming from the sky, $T_{\rm noise}^{\rm horn}$ is the noise generated by the horn alone, $T_{\rm noise}^{\rm Ant}$ is the noise temperature of the whole antenna system, η is the efficiency of the feed horn and $T_{\rm ph}^{\rm pol}$ is the physical temperature of the

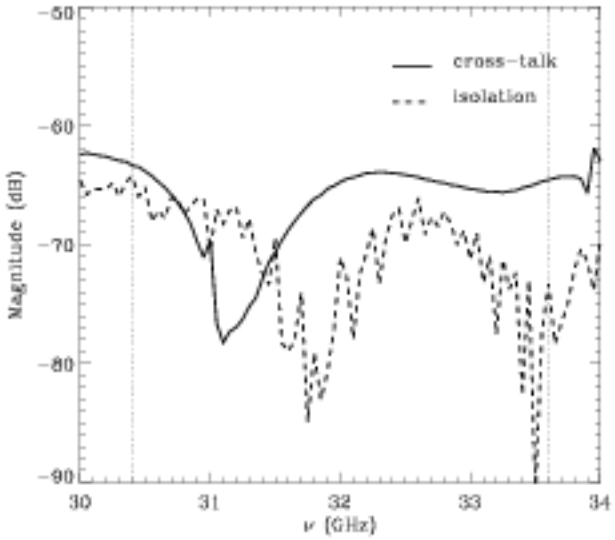

Figure 5.4: Magnitude of both the isolation between the two rectangular ports and the cross–talk between the two polarization states for the 32 GHz OMT of SPOrt. The vertical dotted lines define the 10% band.(From Cortiglioni et al. 2004 [34])

polarizer. The two quantities

$$SP_{\rm OMT} = 2\frac{\Re(S_{A1}S^*_{B1})}{|S_{A1}|^2}, \tag{5.13}$$

$$SP_{\rm pol} = \frac{1}{2}\left(1-\frac{|S_\perp|^2}{|S_\parallel|^2}\right), \tag{5.14}$$

describe the performances of the OMT and the polarizer, respectively, in terms of offset generation. Uncorrelated signals like noise and sky emission are partially detected as correlated because of the OMT cross–talk (S_{A1} and S_{B1} representing the transmission and cross–talk coefficients of the OMT, respectively) and the polarizer attenuation difference ($S_\parallel$ and $S_\perp$ giving the transmissions of the two polarization states).

Specification requirements for OMT and polarizer are then set by considering the radiometer knee frequency, $f_{\rm knee}$, which is defined by the time scale at which the low frequency component of the noise, also known as $1/f$, prevails over the white one.

The $1/f$ noise component give rise to correlated noise patterns (see Sect. 5.2), which may be greatly removed through destriping techniques. However, successful destriping requires that the radiometer knee frequency be lower than the signal modulation frequency, $f_{\rm knee} < f_o$ (with an ideal goal of $f_{\rm knee} < 0.1 f_o$). For SPOrt, the latter corresponds to the orbit frequency

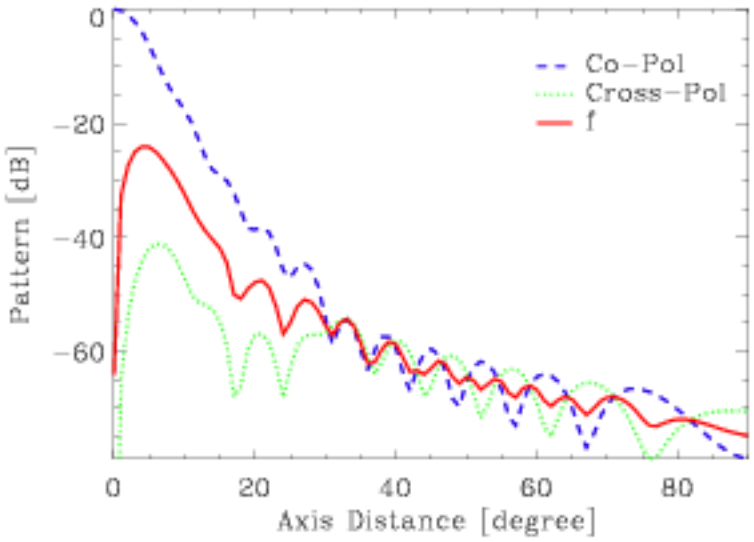

Figure 5.5: Co–polar, cross–polar and f patterns, with respect to the axis distance θ, for the 90 GHz feed horns of SPOrt . The spurious polarization coming from the horn is generated by the anisotropy distribution $\Delta T(\theta\phi)$ in combination with the f pattern (see text).(From Cortiglioni et al. 2004 [34])

$f_o = 0.18$ mHz.

The knee frequency of a correlation receiver is related to that of its amplifiers by the formula:

$$f_{\rm knee} = \left(\frac{T_{\rm offset}}{T_{\rm sys}}\right)^{2/\alpha} f_{\rm knee}^{\rm hm} \tag{5.15}$$

where $T_{\rm sys}$ the system temperature and $\alpha \sim 1$ [154] is the power–law index of the amplifiers' $1/f$ noise behaviour, and typical frequencies are $f_{\rm knee^{hm}} \sim 100 - 1000$Hz.

SPOrt design guaranteed that $T_{\rm offset} \sim 50$ mK, while $T_{\rm sys} \sim 100$ K. Together these values translate into:

$$f_{\rm knee} \sim 2.5 \times 10^{-7} f_{\rm knee}^{\rm hm} \tag{5.16}$$

fully satisfying the requirements for an efficient destriping.

Besides the offset generation, the spurious polarization generated by the optics introduced further systematics effects which must be put under control [23]. This is due to the anisotropy distribution of the unpolarized radiation, modulated by the f pattern:

$$\begin{aligned} \Delta T^{\rm horn} &= \frac{1}{\Omega_A}\int_0^{\pi} \sin\theta\, d\theta \int_0^{\pi/2} [\Delta T_b(\theta,\phi) \\ &- \Delta T_b(\theta,\phi+\pi/2) + \Delta T_b(\theta,\phi+\pi) \\ &- \Delta T_b(\theta,\phi+3/2\pi)]\ f(\theta,\phi)\, d\phi\,, \end{aligned} \tag{5.17}$$

$$f(\theta,\phi) = -P(\theta,\phi)\chi^*(\theta,\phi+\pi/2) + \chi(\theta,\phi)P^*(\theta,\phi+\pi/2)\,, \tag{5.18}$$

where P and χ are the co–polar and cross–polar patterns, normalized to the P maximum, respectively, and Ω_A is the antenna beam. The f pattern consists of a 4–lobe structure, with lobe size close to the FWHM of the instrument. A worst–case analysis of the contamination gives

$$\Delta T^{\rm horn} = SP_{\rm horn}\ \Delta T_{\rm rms}({\rm FWHM})\,, \tag{5.19}$$

with

$$SP_{\rm horn} = 2\,\frac{1}{\Omega_A}\int_0^{\pi}\sin\theta\,d\theta\int_0^{\pi/2}d\phi\,f(\theta,\phi) \tag{5.20}$$

and $\Delta T_{\rm rms}({\rm FWHM})$ the rms temperature anisotropy on FWHM scale. As shown in Fig. 5.5, in case of the SPOrt feed horns the contribution of the f pattern is $SP_{\rm horn} \sim -24$ dB and the rms contamination due to the 30 μK–CMB anisotropy is thus lower than 0.2 μK.

5.1.1 Calibration procedure

The accuracy needed for CMB polarization measuring requires a very efficient calibration of the instrumental response to small polarized signals. Laking well–characterized astrophysical sources, calibration occurs through measurements of predefined signals, *the markers*, which must be inserted directly into the radiometer. Moreover, as polarization is a tensor quantity, standard marker injectors can not be used and a new concept calibrator, valid for any radio–polarimeter and based on the insertion of three signals at different position angles, has thus been developed.

The entire radiometer may be schematically represented as a system connecting two input signals A and B, representing the high frequency signals in the circular polarization base (E_L and E_R), to two low–frequency outputs Q_m and U_m corresponding to the Stokes parameters directly measured by the radiometer. The output of the radiometer can be thus described by the expression:

$$\begin{bmatrix} Q_m \\ U_m \end{bmatrix} = \begin{bmatrix} H_{qq} & H_{qu} \\ H_{uq} & H_{uu} \end{bmatrix}\begin{bmatrix} Q \\ U \end{bmatrix} + \begin{bmatrix} T_{qa} & T_{qb} \\ T_{ua} & T_{ub} \end{bmatrix}\begin{bmatrix} |A|^2 \\ |B|^2 \end{bmatrix} \tag{5.21}$$

where Q and U are the input Stokes parameters, while H and T are generic real matrices; they transform polarization circles in the QU–plane into rotated and translated ellipses. Assuming that the intensities of the total signals A and B

are equal ($|A|^2 = |B|^2 \propto P$), eq. 5.21 can be rewritten as $Y = H\,X + C\,P$, where C is a two–element vector. The calibration procedure consist then in the evaluation of the matrices H and the vector C and can be accomplished by directly measuring the quantities Q_m and U_m in presence of markers. In SPOrt case, three markers consist with known polarization angles θ_i, each corresponding to a linearly polarized field, are injected. The matrix H is then given by:

$$H\,[\,\tfrac{\Delta X_2}{\Delta P_2} - \tfrac{\Delta X_1}{\Delta P_1}\;\tfrac{\Delta X_2}{\Delta P_2} - \tfrac{\Delta X_1}{\Delta P_1}\,] = [\,\tfrac{\Delta Y_2}{\Delta P_2} - \tfrac{\Delta Y_1}{\Delta P_1}\;,\quad \tfrac{\Delta Y_2}{\Delta P_2} - \tfrac{\Delta Y_1}{\Delta P_1}\,] \tag{5.22}$$

where ΔX_i, ΔY_i and ΔP_i are the variations of the input and output Stokes parameters and of the total power, respectively. To obtain a well–conditioned matrix the markers should correspond to signals with a relative rotation of either 45° or 60°.

5.2 Destriping and Map Making

Low frequency noise introduces correlations among successive samples of the measured signal and leads to typical striping effects when producing sky maps.

However, when data are taken from spinning spacecrafts, most of the low frequency noise can be removed by software, provided the radiometer knee frequency is lower than the satellite spin frequency. The low frequency noise of the SPOrt radiometers is expected to have a $1/f$–like spectrum dominated by transistor gain fluctuations [34]. The present state of the instrument already guarantees a knee frequency $f_{\rm knee}$ lower than the ISS orbit frequency f_o.

Various destriping algorithms have been proposed in recent years to clean CMB anisotropy data, e.g., [95], together with a first algorithm specifically designed for the polarization case [118]. They are generally based on χ^2 minimizations and involve large matrix inversions.

A different technique had been implemented for SPOrt, consisting of a simple but effective iterative algorithm relying upon minimal assumptions: the radiometer must be stable during the signal modulation period (the time needed to complete one orbit in case of SPOrt), so that the instrumental offset can be assumed to be constant over the same period, and there must be enough overlap between different orbits. In such situations, noise could be split into two parts: for time scales shorter than the orbit period it is essentially white, whereas for longer timescales the $1/f$ component can be modeled as a different constant offset for each orbit. A simple iterative procedure can then be applied to remove these offsets from the Time Ordered Data (TOD) before map–making. No assumptions need to be made about the statistical properties of the noise.

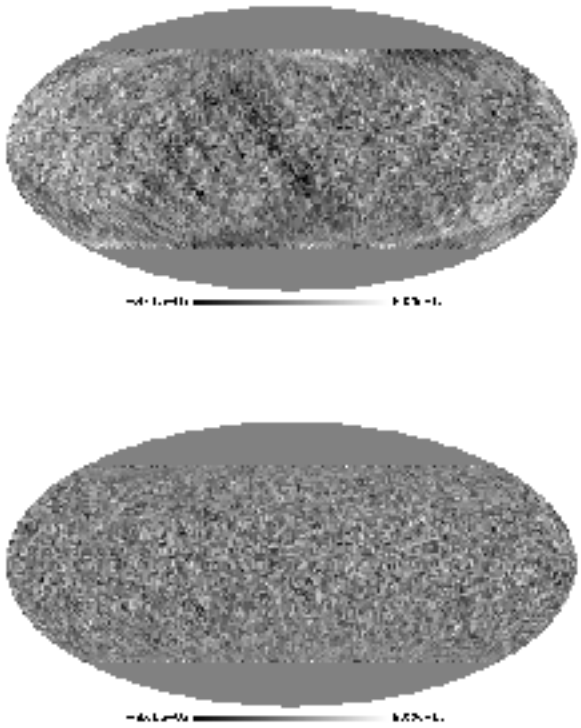

Figure 5.6: Noise simulated maps before (top) and after (bottom) destriping, for the case $f_{\rm knee} = 1.8 \cdot 10^{-4}$, in Kelvin. The HEALPix parameter $Nside$ is 32 (From Cortiglioni et al. 2004 [34]).

The map–making itself consists of a simple average of the measurements corresponding to the same pixel, which is the optimal method once only white noise is left [143].

Although the algorithm had been studied to destripe Q and U data., it can be easily simplified to deal with scalar quantities. However, the average of the measured signal is lost in the latter case. On the contrary, for Q and U maps the average signal can be recovered provided the polarimeter reference frame rotates about the standard reference frame (i.e., polar basis [10]) while running along each orbit, as in case of SPOrt. This feature is especially useful when measuring foreground contributions.

Table 5.3: Excess rms noise due to low–frequency contributions, with respect to the white noise level, for pixels of $\simeq 7^{\circ}$.

$f_{\rm knee}$ (Hz)	Before Destriping	After Destriping
1.8×10^{-4}	310%	6%
1.8×10^{-5}	35%	$< 1\%$

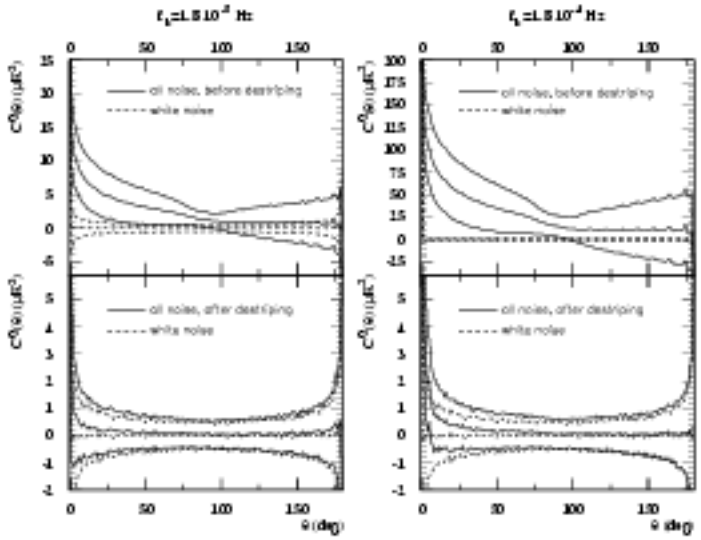

Figure 5.7: Average and 1σ band of correlation functions $C^{Q}(\theta)$ measured from 500 noise maps, before and after destriping, for two values of the knee frequency f_{knee}. Before destriping the y scale is not the same for the two f_{knee} values. Each simulation corresponds to about one year of SPOrt realistic data taking. The case of purely white noise is shown for comparison (From Cortiglioni et al. 2004 [34]).

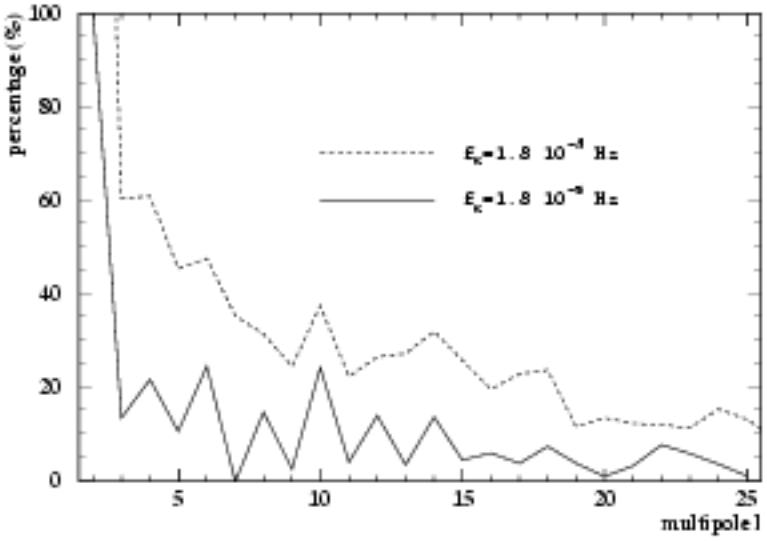

Figure 5.8: Increment, due to the presence of residual correlated noise, in the rms of measured noise power spectra, after destriping, as a function of the multipole, in percentage of the rms of purely white–noise power spectra. (From Cortiglioni et al. 2004 [34]).

Figure 5.6 shows a simulated noise map (both $1/f$ and white) before and after destriping. A possible way to quantify the quality of the destriping is measuring the fractional excess pixel noise with respect to the case of purely white noise. Results are shown in Table 5.3 for two different values of the knee frequency, corresponding to the SPOrt goal knee frequency, $f_{\rm knee} = 1.8 \times 10^{-5}$ Hz, and the SPOrt orbit frequency, $f_{\circ} = 1.8 \times 10^{-4}$ Hz, the latter representing a conservative case.

Another way to quantify the residual correlated noise is measuring and inspecting the two–point correlation functions $C^{Q}(\theta) = \langle Q(1)Q(2)\rangle$ and $C^{U}(\theta) = \langle U(1)U(2)\rangle$ (see Sec. 2.3) of simulated Q and U noise maps. Averages and 1σ bands of 500 correlation functions $C^{Q}(\theta)$ measured from maps containing both white and $1/f$ noise, before and after destriping, are compared to the purely white noise case in Fig. 5.7 for the same knee frequencies as in the previous test. As expected, the correlated noise is strongly reduced by the destriping procedure, the residuals falling within the statistical error of the white noise case for $f_{\rm knee} = f_{\rm knee}^{\rm goal}$.

The polarization power spectra C_{El} and C_{Bl} can be obtained from the measured correlation functions by inverting eqs. 2.21 [67, 156, 109]. If the correlation functions are measured directly on Q and U maps via $O(N_{\rm pix}^2)$ operations ($N_{\rm pix}$ being the number of pixels in the measured map), this method has the advantage of avoiding edge problems arising when using fast spherical transforms [26].

The region of low multipoles is the most sensitive to low frequency residuals, some contributions being always found here even after the application of other destriping techniques [95]. Even though residual noise correlations can be modeled and subtracted from the measured $C^{Q,U}(\theta)$ functions before integration, their presence translates into an increment of the rms of the measured power spectra. A rough estimate for the case of SPOrt is shown in Fig. 5.8.

Chapter 6

Linear & post–linear fluctuation growth

A completely different approach to detecting DE nature can be based on the study of structure formation. From this chapter we begin to describe our work in this direction.

According to the gravitational instability theory of structure formation, the initial density field $\rho(x)$ is homogeneous, apart of small fluctuations described by the density contrast

$$\delta = \frac{\rho - \langle\rho\rangle}{\langle\rho\rangle},$$

that, under the effect of gravity, shall grow into the present structures of the world, over all scales, up to galaxies, groups and clusters.

The growth of density perturbation under their self–gravity can be treated in the linear theory until $\delta << 1$, but linear theory is inadequate when gravity itself takes density fluctuations above unity, into the strongly non-linear regime. Overdensities characterized by $\delta >> 1$ are known to exist, in the present world: e.g., clusters of galaxies, the largest bound structures in the sky, are characterized by values of δ of order of several hundreds, although being, among cosmic systems, those for which δ keeps smallest, because of the difficulty they have to dispose of the heath produced by gravitational contraction.

To follow structure formation we therefore need techniques or approximations able to deal with the non linear evolution of perturbations. In this chapter we shall deal with some *semi*–analytical approaches, studying the growth of a spherical density enhancement and using the results of this study to work out mass functions and their evolutions within the *Press & Schechter* approach.

We shall refer to these treatments as *post–linear*, as they concern a regime when linearity is certainly overcome, but, thanks to suitable geometrical restric-

tions, can still lead to results whose validity is not restricted by probabilistic arguments. From this point of view, their significance is similar to linear outputs.

In particular, we shall report in this chapter the post–linear treatment of DDE models (Mainini, Macciò & Bonometto 2003a; Mainini et al. 2003), while the numerical approach based on N-body simulations will be deepened in the next chapter.

6.1 Linear growth

As discussed in the previous chapter, when approaching the present epoch, DDE pressure (p_{DE}) and energy density (ρ_{DE}) have a ratio (w) comprised between -1 and 0, but typically close to -1.

In the equation

$$\ddot{\delta} + 2\frac{\dot{a}}{a}\dot{\delta} - 4\pi G\rho\delta = 0 \tag{6.1}$$

ruling fluctuation linear evolution (here dots yield differentiation with respect to ordinary time), the ratio $\dot{a}/a \propto 1/t$ with a proportionality coefficient which depends on w and its time evolution, while also the dependence of ρ on t is fixed by the solution of the Friedmann equation, linked to w. Eq. (6.1), however, has analytical integrals, both in the case of a flat model with $\Omega_m = 1$ (SCDM) and in a few other cases. For instance, Carrol et al (1992) and Lahav et al (1993) found analytical expression of the increasing mode of (6.1), in the cases of $w = -1$ and $w = -1/3$, reading

$$\delta(a) = \frac{5\Omega_0}{2af(a)} \int_0^a f^3(a')da' \tag{6.2}$$

where $f(a) = \frac{da}{dt}$ is to be viewed as known function of a or a'.

On the contrary, in the case of DDE, no analytical expression for $\delta(a)$ is available and eq. (6.1) is to be integrated numerically once $a(t)$ is known. In Fig. 6.2, we report the behavior of the increasing mode for RP and SUGRA models. For the sake of comparison the behavior of $\delta(a)$ for SCDM is also shown.

The results of eq. (6.1), which is linear, do not depend on the initial normalization of δ. Once such normalization is fixed, the values $t_{nl.}$ or $a_{nl.}$, above which linearity is lost can be easily seeken. The initial value of δ depends, first of all, on the length scale of the fluctuation, usually determined by the wave–number k. However, until linearity holds, the generic assumption is that

the distribution of initial amplitudes, around the average value characterizing a given scale, is Gaussian. This however means that, even once an initial fluctuation spectrum, suitably normalized, has been assigned and the length scale is fixed, there are no single values for $t_{n.l.}$ and $a_{n.l.}$.

In spite of that, the solution of eq. (6.1) does matter until $z = 0$, even on scales which have surely gained non–linearity well before the present epoch. In fact, instead of giving an initial value of δ at an initial reference time to be suitably agreed, we can avoid to refer to such time, simply telling which value δ should have today, if it obeyed linear evolution, even though such value exceeds unity. This criterion will be followed, e.g., to build the so–called *Press & Schechter* mass function.

6.2 Non–linear growth: analytical approach

Another preliminary step, to construct such expression, amounts to studying the non–linear evolution of a spherical density enhancement. Real density enhancements are expected to be highly irregular and random. *A–priori*, a requirement of sphericity has no motivation apart of reducing the number of variables in dynamical equations. Much work has been however done in this line, starting with Gunn & Gott (1972), Gott & Rees (1975) and Peebles (1980), who studied the problem in SCDM. Then, Lahav et al. (1991), Eke et al. (1996), Brian & Norman (1998) and others generalized the results to ΛCDM models. In spite of the lack of cogent physical motivations, results obtained under the restriction of sphericity were extremely useful to predict physical features.

The reason of this success is only partially understood. As a matter of fact, the standard fluctuations will have an asymmetrical growth, even when, initially, they are approximately spherical, giving place to typical *pancakes*. This is expected on a theoretical basis and has been verified since early simulations. In spite of that, when an individual system is formed, it undergoes a phase dubbed *violent relaxation*, after which it approaches virial equilibrium. During this phase, an approximate spherical shape is regained.

Besides of the complete loss of sphericity in intermediate states, which can even cause a full disruption of the system in sub–entities, there is a further point which should be taken into account: the fact that no system is fully isolated during its growth.

The discussion on these points could be extended to discuss the scale dependence of various effects (Sheth et al. 2001), the actual size of the virialized region (Macciò, Murante & Bonometto 2003), etc.. Here we want just to out-

line that problems exist and have been considered, although the relevance of spherical dynamics is however mostly linked to the concordance between its results and the real world.

In this thesis we shall discuss, in particular, the spherical growth of a density enhancement when the cosmological model comprises DDE, reporting and widening the results, for RP and SUGRA models, obtained by Mainini, Macciò & Bonometto (2003a) and Mainini et al. (2003b).

Let us therefore consider a spherical perturbation, with uniform inner density within an initial radius R_i, whose initial amplitude, at an initial time $t_i \simeq t_{rec}$, is

$$\Delta_i = 1 + \delta_i \ . \tag{6.3}$$

The radius $R = rR_i$ of the perturbation, at later times, can be found using an equation which is formally identical the Friedmann equations yielding cosmic acceleration and reads

$$\frac{\ddot{r}}{r} = -H_i^2 \left[\frac{\Omega_{m,i}\Delta_i}{2r^3} + \Omega_{r,i}\left(\frac{a_i}{a}\right)^4 + \frac{(1+3w)\rho_{DE}}{2\rho_{cr,i}} \right] \ . \tag{6.4}$$

Here all quantities with subscript i refer to the initial time. In particular $\Omega_{m,i}$ and $\Omega_{r,i}$ are the density parameters for non–relativistic and relativistic matter at that time.

If $\Delta_i > 1$ the fluctuation will eventually stop its growth and start to recontract at a time t_{ta} (*turn–around*), when its radius is R_{ta}. Ignoring pressure and assuming that the configuration remains spherically symmetric, at a later time t_{col} (corresponding to a redshift z_{col}) of order $2\,t_{ta}$ the recontraction will lead to full recollapse and fluctuation density would be infinite, because the radius R formally goes to zero. The value of z_{col} depends on the amplitude of the initial fluctuation δ_i and, to give its value, we should first agree on the exact time t_i.

As above outlined, it is simpler and model independent to use, instead of δ_i, the amplitude δ_c that the fluctuation would reach at z_{col} in the linear theory, even though such value is obviously $\gg 1$. For SCDM, independently of the scale size and z_{col},

$$\delta_c^{SCDM} \simeq 1.68 \tag{6.5}$$

(see, e.g., Coles & Lucchin 1995). For any other model, δ_c does depend on z_{col}.

The process of recollapse down to nil is obviously unphysical. In the contraction stages, potential energy turns into heat and, unless microscopic kinetic energy can be successfully radiated away, contraction will stop when virial equilibrium is attained and the fluctuation size is R_v. Requiring energy conserva-

figure=fig/rad.ps,angle=0.,height=8.0truecm

Figure 6.1: Time dependence of the radius of a density fluctuation in various models; horizontal lines, at the right, indicate the R_{vir}/R_i attained at t_0. Similar plots can be given when full recollapse is expected at $t < t_0$.

tion and virial equilibrium we obtain the following algebric cubic equation for $x = R_v/R_{ta}$:

$$x^3 - \frac{1+y(a_{ta})}{2y(a_{col})}x + \frac{1}{4y(a_{col})} = 0, \tag{6.6}$$

where

$$y(a) = \frac{1-\Omega_m(a)}{\Delta_i \Omega_m(a)} \left(\frac{R_{ta}}{R_i}\right)^3 \left(\frac{a_i}{a}\right)^3 . \tag{6.7}$$

These equations can be applied to the case when the underlying model comprises DDE. We can use, in particular, the expression of $y(a)$ of the model assigned and the dependence of Ω_m on the scale factor a, obtained for such model.

Results of such approach are shown in figure 6.1, where we plot $R(t)$ for two RP potentials ($\Lambda/\mathrm{GeV} = 10^2$ and 10^8) and ΛCDM. SUGRA potentials yield curves intermediate between RP and ΛCDM models and just slightly dependent on the energy scale Λ. A careful inspection of the figures shows that, at variance form SCDM and ΛCDM, RP models have a slight asymmetry between expansion and recontraction, due to the evolution of DE density. In Fig. 6.1, the virialization radius R_{vir}, from which Δ_c is computed, is also shown (short horizontal lines).

The actual radius of the final virialized halo is often larger than R_v, owing to deviations from spherical growth in the real world (Macciò, Murante & Bonometto 2003). However, R_v is a good starting point for statistical analysis. Multiplying eq. (6.6) by $2y$ and taking then $y = 0$ (i.e. $\Omega_m \equiv 1$: SCDM), we recover that $x = 1/2$. In general, the root x lays slightly below this value.

Figure 6.2 shows the linear and non–linear growth of a density contrast, for SCDM, ΛCDM and a RP models normalized to have $z_{col} = 0$. Similar plots can be made for any redshift of collapse. The Figure can be used to find the initial amplitude Δ_i at any given redshift z_i and the value of δ_c for a perturbation collapsing at present. Using the final value of Δ we obtain the virial density contrast

$$\Delta_c = \Omega_m \Delta. \tag{6.8}$$

In the linear and non–linear cases, deviations from the SCDM behavior often compensate and the final values of δ_c are just slightly model dependent: in figure 6.3 we report the dependence of δ_c on the matter density parameter

figure=fig/lin.ps,angle=0.,height=8.0truecm

Figure 6.2: Normalized linear (bottom curves) and non-linear (top curves) amplitude of density fluctuations for SCDM (dotted), (dashed), and RP (full) models. The amplitude of fluctuation was normalized to have collapse the perturbation at $z_{col} = 0$. Similar plots can be given for collapse at any other redshift. The density contrast $\Delta = \Delta_c/\Omega_m$. w_0 is the value of w at $z = 0$

figure=fig/deltac.ps,angle=0.,height=8.0truecm

Figure 6.3: The dependence of δ_c on the matter density parameter Ω_m at $z = 0$ for 4 RP ($\Lambda/\mathrm{GeV} = 10^2$, 10^4, 10^6 and 10^8) and 2 SUGRA models ($\Lambda/\mathrm{GeV} = 10^2$ and 10^8). Λ values increase from top to bottom curves.

Ω_m at $z = 0$, for 4 RP and 2 SUGRA models and in figure 6.4 its dependence on redshift for $\Omega_m = 0.3$ for the same models.

On the contrary, the spread among the virial density contrasts Δ_c, is large as indicated by figure 6.6, which shows Δ_c as function of Ω_m for different models. The evolution of Δ_c with redshift is also model dependent, as shown by Figure 6.7.

For practical uses it is important to provide an analytical approximation for Δ_c. The expression we shall give is valid at any redshift z, provided that we know the matter density parameter Ω_m at that redshift, and reads

$$\Delta_c = 178\ \Omega_m^{\mu(\Omega_m,\Lambda)}, \tag{6.9}$$

so that the essential quantity is $\mu(\Omega_m,\Lambda)$, for which the general expression $a + b\Omega_m^c$ holds, with $c = 1\,(2)$ for RP (SUGRA) models. The parameters a and b are given by

$$a = a_1\lambda + a_2, \quad b = b_1\lambda + b_2, \tag{6.10}$$

where

$$\lambda = \log(\Lambda/\mathrm{GeV}) \tag{6.11}$$

and the coefficients are given in Table 1. Figure 5 shows the dependence on λ of the differences $|\Delta_c^{num}/\Delta_c^{an} - 1|$, at $z = 0$, for models with $h = 0.7$ and different values of λ, as a function of Ω_m. (Here Δ_c^{num} is obtained from the full numerical treatment, while Δ_c^{an} is the expression (6.9)) Discrepancies stay below 0.5 % for any $\Omega_m > 0.15$. However, for large λ, the approximation is even better: $\simeq 0.2$ %, for any Ω_m.

figure=fig/deltac2.ps,angle=0.,height=8.0truecm

Figure 6.4: The dependence of δ_c on the redshift z is shown for $\Omega_m = 0.3$ and $h = 0.7$. Λ values are the same as in fig. 6.3

figure=fig/Ddif.ps,angle=0.,height=8.0truecm

Figure 6.5: Fractional discrepancy between numerical and analytical results on Δ_c.

Table 6.1: Interpolation coefficients for Δ_c

Model	a_1	a_2	b_1	b_2
RP	-1.45×10^{-2}	0.186	−0.011	0.22
SUGRA	-2.25×10^{-3}	0.3545	−0.01875	−0.1225

6.3 The mass functions and their evolution

One of the most frequent applications of the spherical collapse model is to predict the mass function of bound objects using the Press & Schechter (Press & Schechter 1974) formalism. According to their arguments, the cumulative mass function (the comoving number density of objects of mass greater then M)

$$N(>M) = \int_M^\infty n(\mathrm{M}) d\mathrm{M} \tag{6.12}$$

is obtainable from

$$n(M) = \left(\frac{2}{\pi}\right) \frac{\langle\rho\rangle}{M} \frac{\delta_c}{\sigma_M^2} \left|\frac{d\sigma_M}{dM}\right| \exp\left(-\frac{\delta_c^2}{2\sigma_M^2}\right) , \tag{6.13}$$

$n(M)$ being, therefore, the number density of objects with mass between M and $M + dM$:

In the above expression, holding at any redshift z, $\langle\rho_m\rangle$ is the background matter density at such z. Then, according to the previous section, δ_c is the amplitude attained by a fluctuation at such redshift z according to the linear equation (6.1), if its initial amplitude is such that it would fully recollapse at that z, in the spherical non–linear approximation. Finally σ_M is the rms fluctuation amplitude, at that z, over a comoving smoothing scale $R = (3M/4\pi\langle\rho_m\rangle)^{1/3}$. In the expression of

$$\sigma_M^2 = \frac{1}{(2\pi)^3} \int d^3k\, P(k,z)\, W_{TH}^2(kR) \tag{6.14}$$

figure=fig/DelOm.ps,angle=0.,height=8.0truecm

Figure 6.6: Ω_m dependence of Δ_c for different cosmologies. RP and SUGRA models, at $z = 0$, have a pressure/density ratio $w_o = w$ of the constant w models shown. The full curve is for ΛCDM.

figure=fig/Delz.ps,angle=0.,height=8.0truecm

Figure 6.7: Redshift dependence of Δ_c for different cosmologies. RP and SUGRA models, at $z = 0$, have a pressure/density ratio $w_o = w$ of the constant w models shown. Solid curves are for SCDM (upper horizontal line) and ΛCDM.

figure=fig/pk.ps,angle=0.,height=8.0truecm

Figure 6.8: Power spectrum at $z = 40$ for and DE models, all power spectrum are normalized to have the same σ_8 at $z = 0$.

the main quantity to be specified is the filter $W_{TH}(x)$: in most applications, a top–hat filter, whose Fourier transform reads

$$W_{TH}(x) = \frac{3}{x^2}\left(\frac{\sin x}{x} - \cos x\right) \ , \tag{6.15}$$

is suitable. The power spectrum of density fluctuations $P(k, z)$ is obtained from the primeval spectrum Ak^n and the transfer function $T(k, z)$:

$$P(k,a) = Ak^n T^2(k, z) \ . \tag{6.16}$$

Here below a Harrison–Zel'dovich primordial power spectrum ($n = 1$) has been however assumed.

In order to work out the mass function at ant z, therefore, the essential ingredients are: (i) The spectrum normalization. (ii) The transfer function T. Accordingly, the mass function and its evolution can be evaluated, also for DDE models, as soon as a linear program yielding $T(k, z)$ is available and a normalization is assigned, e.g. through a value of σ on a given scale, at $z = 0$. As is usual, the normalization length scale considered in our work is $8\,h^{-1}$Mpc.

Quite in general, σ_M^2 and $N > M$ were calculated for DDE models, using the transfer function obtained from a suitable generalization of the public program CMBFAST, obtained in our research group. Initial conditions for density fluctuations in DDE were set according to the tracker solution in radiation dominated era (Steinhardt, Wang & Zlatev 1999; Zlatev, Wang, & Steinhardt 1999). DDE fluctuations, taken into account in primeval fluctuation evolution, are damped soon after a scale enters the horizon and, therefore, are not important in further fluctuation evolution. Accordingly, in our problem, their relevance amounts to causing some modification of the transfer function. (On the contrary, they cause major modifications of CMB anisotropy and polarization). In figure 6.8 is shown an example of the power spectrum for RP, SUGRA and models. The first finding of our analysis is that the difference between the mass functions for RP or SUGRA models and the mass function of a ΛCDM

figure=fig/MF1.ps,angle=0.,height=8.0truecm

Figure 6.9: The number density of clusters is shown for standard CDM (lowest curve), OCDM (long–short dashed upper curve), ΛCDM (solid intermediate curve), 2 RP (long dashed curves) and 2 SUGRA (dotted curves) models. The values of Λ/GeV are 10^2, 10^6 for RP and 10^6, 10^{10} for SUGRA, starting from the lower curves.

figure=fig/MF2.ps,angle=0.,height=8.0truecm

Figure 6.10: The number densities of the previous plot normalized to the values in OCDM are shown.

model, at $z = 0$, bear quite a scarce significance, being smaller than the difference due to a shift by 0.05 in the primeval spectral index. The intrinsic noise of data is then a serious obstacle to any attempt to determine the nature of DE using cumulative mass functions at $z = 0$.

On the contrary, we found a clear imprint of the nature of DE in the evolution of the number density of clusters above a suitable mass scale M. In fig. 6.9, we give the number N of the cluster with $M > 6.9 \cdot 10^{14} h^{-1} M_\odot$ expected in a box of side $L = 100\, h^{-1}$Mpc, as a function of redshift. The numbers at $z > 0$ are normalized to an identical number of clusters at $z = 0$, for all models ($N(z = 0) = 0.13$). In figure 6.9 we give the ratio between the number of clusters expected in various models and the number expected in an open CDM model with the same value of Ω_m. The mass here is selected so to correspond to a cluster whose virial radius is an Abell radius in a standard CDM model. A similar plot, for a slightly smaller mass, was given by Bahcall, Fan & Cen (1997), for standard CDM, ΛCDM and OCDM only (for a recent analysis of the constraints that cluster number counts set to the cosmological model, see, e.g., Holder, Haiman & Mohr, 2001).

The main results of this analysis (Mainini Macciò and Bonometto 2003a, see also Mainini et al 2003b) is that the cluster evolution depends on the nature of DE in a significant way. Models with RP potentials approach the evolution of open CDM models as the energy scale Λ increases. On the contrary, the evolution of SUGRA models is intermediate between open CDM and ΛCDM models.

Chapter 7

Nbody Simulations

When fluctuations enter in a strongly non linear regime (i.e. $\delta >> 1$) the only way to follow their evolution is via numerical techniques.

Structures formation models attempt to reduce cosmology to an initial conditions problem. Given the initial conditions (a background cosmological model with specified composition of matter, radiation and fields, such as cosmological constant or DDE, and primordial fluctuations for all these components) the goal is to compute, using well-known laws of physics, the evolution of structures from the Big Bang to the present day.

Numerical simulations play a very significant role in cosmology. The first simulation of interacting galaxies was performed in 1947 by Holmberg, using an analog optical computer. Gravity was represented by the flux from 37 lighbulbs, with photocells and galvanometers used to measure and display the square inverse law force. The first astronomical *N-body* computations using digital computers were made in the early 1960s (Aarseth 1963). These early simulations were limited to at most about 100 particles (now simulations are able to handle billions of particles).

In this chapter we first summarized the equations of motion that it needs to integrate in an N–body simulation, and their modification in the presence of DE. Than we describe in detail the N–body code ART (Kravtsov et al 1997) and its new versions able to deal with dynamical dark energy and coupled dark energy (Macciò et al. 2003). For a more general discussion on the different aspects of the simulations, including history of the subject, see the review by Bertschinger (1998).

7.1 Particles Dynamics

Usually the problem of the formation and dynamics of cosmological objects is formulated as N-body problem: for N point-like objects with given initial positions and velocities find their positions and velocities at any later moment.

The correct approach to follow the motion of particles is to start with the Vlasov equation:

$$\delta_t f_i + \left(\frac{\mathbf{p}}{\mathrm{m}}\right) \nabla_x f - m\nabla\varphi(\mathrm{x},\mathrm{t})\nabla_{\mathrm{p}}\mathrm{f} = \mathbf{0} \tag{7.1}$$

where f_i are the distribution functions of the different clustered components i (here we neglect the baryonic component, which of course is very interesting, but would complicate our situation even more) and φ is the gravitational potential. This equation for the evolution of f_i must be considered together with the poission equation in comoving coordinates:

$$\begin{aligned} \nabla^2\varphi &= 4\pi G a^2(\rho(\mathrm{x},t) - \langle\rho_{\mathrm{m}}(t)\rangle) = 4\pi G a^2 \Omega_{\mathrm{m}} \delta_{\mathrm{m}} \rho_{\mathrm{cr}}, \\ \delta_{\mathrm{m}}(\mathrm{x},t) &= (\rho_{\mathrm{m}} - \langle\rho_{\mathrm{m}}\rangle)/\langle\rho_{\mathrm{m}}\rangle), \\ \rho_{\mathrm{m}}(\mathrm{x},t) &= a^{-3}\sum_i m_i \int d^3\mathbf{p} f_i(\mathrm{x},\mathrm{x},t) \end{aligned} \tag{7.2}$$

Here $a = (1+z)^{-1}$ is the expansion parameter, $\mathbf{p} = a^2\dot{\mathrm{x}}$ is the momentum, Ω_{m} is the contribution of the clustered dark matter to the mean density of the Universe, m_i is the mass of a particle of $i-$th component of the dark matter. From eqs. (7.1) (7.3) it is possible to work out the equation of motion in an expanding universe:

$$\frac{d\mathbf{p}}{dt} = -\nabla_x\varphi, \quad \frac{d\mathrm{x}}{dt} = \frac{\mathbf{p}}{a^2}. \tag{7.3}$$

It is convenient to use the expansion factor a as time variable instead of t:

$$\begin{aligned} \frac{d\mathbf{p}}{da} &= -g(\Omega_m, \Omega_{DE}, a) \ \nabla_x\varphi \\ \frac{d\mathrm{x}}{da} &= g(\Omega_m, \Omega_{DE}, a) \ \frac{\mathbf{p}}{a^2} \\ \nabla^2\varphi &= 4\pi G\Omega_m \delta_{\mathrm{m}} \rho_{\mathrm{cr},0}/a, \end{aligned} \tag{7.4}$$

In these equations $\rho_{\mathrm{cr},0}$ is the critical density at $z = 0$ and $g = dt/da$. If there is no coupling g can be written as:

$$g = \frac{dt}{da} = \left(aH_0\sqrt{\frac{\Omega_{m,0}}{a^3\Omega_m(a)}}\right)^{-1} \tag{7.5}$$

where $\Omega_{m,0}$ is the present day dark matter density parameter. In this case (no coupling) the different cosmological models contribute to the motion of particles only trough eq (7.5), so to include dynamical dark energy we just need to compute g, this means that we need to know the time evolution of Ω_m. Unfortunately for DDE models no analytical expression of $\Omega_m(a)$ is readily available, in section 7.5 we provide an accurate approximate expression of Ω_m, for various redshifts and for different Dark Energy models. To solve numerically the above equations different techniques can be applied, they are briefly describes in the next section.

7.2 Codes

There are many different numerical techniques to follow the evolution of a system of many particles (Bertshinger 1998). Most of the methods for cosmological applications can be divided in three main categories: Particle–Mesh (PM) code, direct summation or Particle-Particle (PP) code and TREE code. All methods have their advantages and their disadvantages.

- **PP**: Particles Particles approach is the simplest way to compute the force among particles: the force experimented by one particle is obtained by a direct summation of the force due to all the other N particles:

$$F_i = \sum_{j=1,N} -\frac{Gm_i m_j(\mathbf{x}_1 - \mathbf{x}_j)}{(\epsilon^2 + |\mathbf{x}_1 - \mathbf{x}_j|^2)^{3/2}} \tag{7.6}$$

  where ϵ is the softening parameter used to suppress forces on scale $< \epsilon$. Because of the number of operation to be done at each step is $O(N^2)$ this approach becomes prohibitively expensive once $N > 10^4$.

- **PM**: It uses a mesh to compute density and potential. The equation of motion are the solved on the mesh using a FFT (Fast Fourier Transform) algorithm. The main advantages of this method are: i) it is faster than PP, the number of operation is linked with the number of cells of the mesh (N_g) and it scales as $(N_g \log_2 N_g)$ ii) it permits to use a large number of particles. The problem is that the grid method is only able to produce reliable inter particles forces down to a minimum of at least two grid cells.

- **TREE code**: particles are divided in groups and subgroups in a sort of tree–like hierarchy. The basic idea to compute the force on a particles is to treat the groups of particles far from it as a single big particles with

position in the baricenter of the group and total mass equal to the sum of the masses of all the particles belonging to the group (Barnes & Hu 1986; Herquist 1987). This is the most flexible code to but it is more time expensive than a PM.

.

7.3 ART CODE

Multigrid methods were introduced long ago, but only recently they started to show a potential to produce real results. An example of a fully adaptive multi grid code is the Adaptative Refinement Tree code (ART). The ART code starts with a uniform grid, which covers the whole computational box. This grid defines the lowest (zeroth) level of resolution of the simulation. The standard Particles-Mesh algorithms are used to compute density and gravitational potential on the zeroth-level mesh. The ART code reaches high force resolution by refining all high density regions using an automated refinement algorithm. The refinements are recursive: the refined regions can also be refined, each subsequent refinement having half of the previous level's cell size. This creates a hierarchy of refinement meshes of different resolution, size, and geometry covering regions of interest. Because each individual cubic cell can be refined (or de–refined), the shape of the refinement mesh can be arbitrary and match effectively the geometry of the region of interest.

The criterion for refinement is the local density of particles: if the number of particles in a mesh cell (as estimated by the Cloud-In-Cell method) exceeds the level $n_{\rm thresh}$, the cell is split ("refined") into 8 cells of the next refinement level. The refinement threshold depends on the refinement level. For the zero's level it is $n_{\rm thresh} = 2$. For the higher levels it is set to $n_{\rm thresh} = 4$. The Poisson equation on the hierarchy of meshes is solved first on the base grid using FFT technique and then on the subsequent refinement levels. There is no particle-particle summation in the ART code and the actual force resolution is equal to ~ 2 cells of the finest refinement mesh covering a particular region. The code uses the expansion parameter a as the time variable. During the integration, spatial refinement is accompanied by temporal refinement. Namely, each level of refinement, l, is integrated with its own time step $\Delta a_l = \Delta a_0/2^l$, where $\Delta a_0 = 3 \times 10^{-3}$ is the global time step of the zeroth refinement level. When a particle moves from one level to another, the time step changes and its position and velocity are interpolated to appropriate time moments. This

figure=fig/Omegafit.ps,angle=0.,height=8.0truecm

Figure 7.1: Fractional discrepancies between the approximated expression (7.9) and numerical data.

variable time stepping is very important for accuracy of the results. As the force resolution increases, more steps are needed to integrate the trajectories accurately. The code adopt a standard second order leapfrog integration scheme of advancing particles to the next time step. For a step n, corresponding to time step $a_n = a_{init} + n\Delta a$, the momenta and position of particles (see eqs (7.5)) are updated as follows:

$$\mathbf{p}_{n+\frac{1}{2}} = \mathbf{p}_{n-\frac{1}{2}} - g(\Omega_m, \Omega_{DE}, a) \quad \nabla\varphi_n \Delta a \tag{7.7}$$

$$\mathbf{x}_{n+1} = \mathbf{x}_n - g(\Omega_m, \Omega_{DE}, a) \quad \frac{\mathbf{v}_{n+\frac{1}{2}}}{a^2_{n+\frac{1}{2}}} \Delta a \tag{7.8}$$

Here the indices $n, n+1$ and $n \pm \frac{1}{2}$ refer to quantities evaluated at a_n, a_{n+1} and $a_n \pm \Delta a/2$ respectively. Extensive tests of the code and comparisons with other numerical N-body codes can be found in Kravtsov (1999) and Knebe et al. (2000).

7.4 ART CODE modifications for DE

For what regards DDE model the cosmological model enter into the code only in the g expression (eq 7.5) through the $\Omega_m(a)$ evolution. In RP and SUGRA models, at variance from models with w = const, no analytical expression of $\Omega_m(a)$ is readily available, the only way is to solve numerically the Fredmann equations. This approach is very time consuming for the code, because we need to re–calculate it at every time step. An accurate approximate expression of Ω_m, for various redshifts and for different models is then useful. We found the following fitting formula (Mainini et al. 2003b):

$$\Omega_m(a) = 1 - (1 - \Omega_{m,0})/(1+z)^{\alpha(z,\lambda)}, \tag{7.9}$$

where $\alpha(z,\lambda) = a + bz^c + d/(1+z)$ with $d = 0$ for RP models. Parameters a, b, c and d have the same structure as eq. 6.10. The coefficients are given in table (7.1).

Figure (7.1) shows the errors of approximation $|\Omega_m^{num}/\Omega_m^{an} - 1|$ as a function of the redshift z for two RP and for two SUGRA models with $\Omega_m = 0.3$ and $h = 0.7$.

Table 7.1: Coefficients for $\Omega_{rm}(z)$

Parameter	$\Omega_{rm} = 0.2$	$\Omega_{rm} = 0.3$	$\Omega_{rm} = 0.4$
RP			
a_1	-5.638×10^{-3}	-2.119×10^{-2}	-3.365×10^{-2}
a_2	-0.813	-0.259	0.207
b_1	-2.460×10^{-2}	-1.833×10^{-2}	-1.384×10^{-2}
b_2	1.382	0.975	0.628
c_1	-5.960×10^{-3}	-6.975×10^{-3}	-8.394×10^{-3}
c_2	8.460×10^{-2}	9.771×10^{-2}	0.119
SUGRA			
a_1	-8.466×10^{-3}	-9.161×10^{-3}	-2.035×10^{-2}
a_2	1.383	1.415	1.427
b_1	-1.386×10^{-2}	-1.753×10^{-2}	-1.336×10^{-2}
b_2	-8.521×10^{-3}	-6.890×10^{-3}	-1.289×10^{-2}
c_1	-3.935×10^{-2}	-4.421×10^{-2}	-4.203×10^{-2}
c_2	0.710	0.688	0.682
d_1	2.088×10^{-2}	1.875×10^{-2}	2.212×10^{-2}
d_2	-0.883	-0.621	-0.416

7.5 ART: combining openMP MPI

The reasons to design a hybrid MPI+OMP code is to combat two issues: (i) OMP parallelization is not very efficient. Scaling depends on particular computer architecture. (ii) Memory is very substantial to run the code. OMP provides a way to access a larger memory. When we use OpenMP all memory of a node is accessible for the code. When using 4 processors, the memory accessible for a task quadruples.

We use rectangular domains for MPI parallelization. The whole simulation volume - a cube - is split into non-overlapping fully covering parallelepipeds. Each domain is handled by one MPI task and can spawn OpenMP threads. Boundaries of the parallelepipeds can move as time goes on in order to equalize the load of different MPI tasks. Figure on the right gives an example of possible splitting of the computational volume in 2d case. Note that boundaries in x-direction are alligned, but they are not alligned in y- (and z-) directions. Each boundary can move but only at the beginning of a zero-level time-step. Once the zero-level time-step is completed, information on cpu consumed by different MPI tasks is used to adjust the boundaries to improve the load balance. Boundaries of the domains can have only discrete positions: they can only be

placed at boundaries of the zero-level mesh. The number of degrees of freedom can be very large. It depends on the number and the configuration of the domains. For the division of the volume by n_x domans in x-direction and n_y, n_z in y- and z-directions, the number of degrees of freedom is $(n_x n_y n_z - 1)$.

Even if ART provides two routine for two different ways of using this large number of degrees of freedom to improve the load balance, the problem of time scaling is reduced but not eliminated. When it is not needed a large number of particles you can simulate separately a lot of boxes simultaneously, and the openMP code inserted in a simple MPI driver is very appropriate. In this case, every similation is indipendent, there is not communications between processors, the time scaling is the best (scaling with the number of processors) and time tail of singles jobs is missed.

As we will see this program is utilized to produce many boxes of $60 Mpch^{-1}$ in short time to build power spectrum, bispectrum, trispectrum in nonlinear region under the $10 Mpch^{-1}$, in fact the contribution from scale bigger than $60 Mpch^{-1}$ is unimportant, so to increase the statistics in shorter time as possible this solution is the most rewarding.

Chapter 8

Open Physical Problems and N-Body Simulations

In this chapter we aim to interface some open physical questions against the potentiality of n–body codes in general, and ART in particular, when used on available supercomputers.

The critical issue, in this respect, is the available *dynamical range*, *i.e.*, the ratio between the size of the box we plan to simulate and the resolution we can achieve. Limitations on the dynamical range are set by the available supercomputer memory.

Using a n–body code based on adaptive PM, it is possible to predict the memory requirements needed to define initial conditions, but it is harder to set a priori the actual memory request during the run. In particular, there will be a further dependence on the size of the box itself, as wider boxes deal with scales where non–linearities are less developed and therefore require not so many refinement levels as smaller boxes.

An indicative request, however, is that, if we run a simulation with N^3 cells, N^3 particles and $N = 512$, we approximately need 10 GB of memory. As memory requirements scale approximately as N^3, a memory limitation $\sim$ 13–14 GB, forbids dealing with any greater dynamical range.

We can however get partially rid of this limitation by running first a simulation with a smaller resolution. This can allow us to inspect where clusters are. Then we shall magnificate the environments of clusters, with a resolution corresponding to $N = 1024$. In a single run we may be unable to magnify all interesting clusters, but we have no *a–priori* limitation on the number of runs.

In Fig. ?? we show how this technique works in a case where it was pushed to its extreme.

figure=fig/magnif.eps,angle=0.,height=10.0truecm

Figure 8.1: A cluster selected in a $300\,h^{-1}$Mpc simulation box is gradually magnified, to be finally shown in a box enclosing just its virial radius. When magnifiaction is operated, the resolution of the simulation is increased in the restricted frame, but the whole simulation still runs, although with a smaller resolution, in the whole box, so that the formation process correctly feels also all external gravitational actions.

8.1 Concentration Distribution Analysis

Let us then discuss which result we can achieve if we simulate a box of the Universe whose side is $L \simeq 60\,h^{-1}$Mpc . In terms of wavenumbers

$$k = 2\pi/L \ , \tag{8.1}$$

this correspondes to $k \simeq 0.105\,h\mathrm{Mpc}^{-1}$. Non–linearities, in the present epoch, extend up to $\sim 10\,h^{-1}$Mpc and then to $k \sim 0.6\,h\mathrm{Mpc}^{-1}$. Accordingly, on the boundary of this box, the cosmic evolution is still widely linear and, even neglecting longer wavelengths, we run little risks to neglect important physical features.

The minimal scale resolved by a similar run is then $\sim 2 \times 60/1024 \simeq 0.11\,h^{-1}$Mpc. The virial radius of a galaxy cluster of mass M, in the present epoch, reads

$$\frac{R_v}{h^{-1}\mathrm{Mpc}} \simeq 1.68 \left(\frac{M}{10^{15} h^{-1} M_\odot} \, \frac{180}{\Delta_v} \right)^{1/3} \ , \tag{8.2}$$

where Δ_v is the virial density contrast of the model considered. For instance, a cluster of $4 \cdot 10^{14} h^{-1} M_\odot$ in a ΛCDM model with $\Delta_v = 100$, has a virial radius $R_v \simeq 1.5\,\mathrm{h}^{-1}\ Mpc\ h^{-1}$.

If we are able to solve $\sim 0.11\,h^{-1}$Mpc, this means that we can test the shape of its radial concentration down to $\sim 1/14$ of its radius. The expected concentration, in this range of masses, is ~ 5 and we are therefore able to study the concentrations of such clusters.

However, when we inspect smaller mass systems, their virial radius decreases as $\sim M^{1/3}$, while the expected concentrations increase. Hence, if we study objects with $M \sim 8 \cdot 10^{13} h^{-1} M_\odot$, their virial radius is $R_v \sim 0.75\,h^{-1}$Mpc, and a resolution of $0.11\,h^{-1}$Mpc allows to inspect their concentration only if it is $<\sim 7$. This is just a little more than the expected average concentration on this mass scale and, therefore, we can hardly study concentration distributions for clusters below $M \sim 8 \cdot 10^{13} h^{-1} M_\odot$.

In order to push our study to lower mass scales, we need considering a smaller box and/or using a higher dynamical range. The former option is risky, as we exclude more and more long wave lengths; the latter one clashes against computer features.

Accordingly, the optimal choice with the available numerical facilities amounts to dealing with $\sim 60h^{-1}$Mpc boxes.

Another important question concerns the number of clusters we can expect, in a given mass range, in such a box. This is fixed by data and spectral normalization must be such to produce the observational numbers.

For the above scale of $4 \cdot 10^{14} h^{-1} M_{\odot}$, in a $100\,h^{-1}$Mpc cube, we can expect ~ 3 cluster. No significant statistics can be however done with less than ~ 10 clusters. Hence we need a total volume ~ 3–$4 \times 100^3\,h^{-3}$Mpc^3 $\sim (150\,h^{-1}$Mpc$)^3$. Accordingly, we need to run, at least, $\sim$16 boxes with a side of $60\,h^{-1}$Mpc.

Our computer facility does however allow us to run up to 32 simultanous boxes, making use of MPI parallelization. Hence, we can test 2 different choices of parameters with a single run.

8.2 Non Linear Spectra Analysis

A $60\,h^{-1}$Mpc box can however be also an optimal choice to study non–linear spectra.

In the present epoch, non–linearity extends up to $k \sim 0.6\,h$Mpc^{-1}, but, at a greater redshift, it gradually concerns only greater and greater wavenumbers.

The comoving length reached by non–linearity, in a SCDM model increases with the scale factor a. In this model, therefore, we can soon indicate at which redshift non linear features will no longer be visible within our dynamical range. It must however be clear that such inspection does not only require that non–linearity can be noticed; we do need to see a wide spectral interval where it is developped. Accordingly, at $z = 0$, where non–linearity extends up to $\sim 10\,h^{-1}$Mpc, we need to inspect ~ 2–$3\,h^{-1}$Mpc. In order to reach a redshift ~ 4, we need a resolution $\sim 0.5\,h^{-1}$Mpc.

Let us however outline that this aim must be achieved before applying the magnification device, as we need to use whole box harmonics. With a 256^3 resolution, we can expect to study non–linearity up to this scale, in a SCDM model.

If the model comprises a DE component, however, the evolution is slower and we can tentatively plan to go up to a redshift $z \simeq 5$.

As a general conclusion we can now focus on the features of the simulations

to run: They should deal with ~ 16 boxes with side $L \simeq 60\,h^{-1}$Mpc. The whole boxes should then be run with a 256^3 mass and force resolution. This will unable us to inspect the spectra up to $z \sim 5$.

Later we shall perform further runs, aiming to magnify ~ 10 clusters for each mass interval we plan to use. For instance, if we plan to devide the mass interval $0.8\text{–}4 \cdot 10^{14} h^{-1} M_{\odot}$ in 8 intervals, we need magnifying 80 clusters, *i.e.* 5 clusters per node. Each cluster requires approximately a $5\,h^{-1}$Mpc box, a fraction $\sim 5.8 \cdot 10^{-4}$ of the whole box, where a 1024^3 resolution will be applied. In each computer node, a fraction $\sim 0.3 \cdot 10^{-2}$ of the whole box needs then to be pushed to maximum resolution.

If the whole box were to be pushed to such resolution the memory requirement would be ~ 80 GB. The requirement for the fraction considered is therefore quite accessible, ~ 0.23 GB and can be achieved in a single run.

Altogether we must therefore run twice the same 2 models, in order to obtain the numerical outputs we need to inspect.

8.3 Weak Lensing Analysis

In this final section we wish to outline that simulations performed with this criterion have an immediate use to study weak gravitational lensing and cosmic shear.

This phenomenon provides a unique method to directly map the distribution of mass in the Universe (for reviews see Bartelmann & Schneider 2001; Mellier et al. 2002; Hoekstra et al. 2002; Refregier 2003). The coherent distortions that lensing induces on the shape of background galaxies have now been firmly measured from the ground and from space. The amplitude and angular dependence of this 'cosmic shear' signal can be used to set strong constraints on cosmological parameters. Several surveys are now in progress to map larger areas and thus reduce the uncertainties in these parameters. However, future ground based surveys will eventually be limited by the systematics induced by atmospheric seeing. Space based observations do not suffer from this effect, but their statistics are currently limited by the small field of view of existing space telescopes.

The weak lensing power spectrum is given by (eg. Bartelmann & Schneider 1999; Hu & Tegmark 1999; see Bacon et al. 2001 for conventions)

$$C_\ell = \frac{9}{16} \left(\frac{H_0}{c}\right)^4 \Omega_m^2 \int_0^{\chi_h} d\chi \left[\frac{g(\chi)}{a r(\chi)}\right]^2 P\left(\frac{\ell}{r}, \chi\right), \tag{8.3}$$

where $r(\chi)$ is the comoving angular diameter distance, and χ_h corresponds to the comoving radius to the horizon. The radial weight function g is

$$g(\chi) = 2\int_{\chi}^{\chi_h} d\chi' \; n(\chi')\frac{r(\chi)r(\chi'-\chi)}{r(\chi')}, \tag{8.4}$$

$n(\chi)$ being the probability of finding a galaxy at comoving distance χ, normalised so that $\int d\chi \; n(\chi) = 1$. In eq. (8.3) the non linear power spectrum $P(k,z)$ play a key role.

Analytical expressions for it have been provided by various authors, but the basic pattern to build it amounts to perform adequate simulations. Up to now suitable simulations, reasonably spanning the parameter space, where only performed for ΛCDM models.

Figure 8.3 shows the lensing power spectrum for the ΛCDM model. Deviations from the model corresponding to variations in Ω_m and w are also shown, highlighting the importance of non-linear evolution for $\ell 100$.

Information on $P(k,\chi)$ is needed up to where $n(\chi)$ becomes negligibly small. In turn this depends on the depth of the sample wherefrom $n(\chi)$ is obtained. Reasonnably complete samples can be expected to peak around $z \sim 1$, and consequently we aim at building non linear power spectrum at least up to $z \sim 2.5$.

We however saw that our numerical approach enables us to arrive up to $z \sim 5$, so enabling us to exploit extremely faint samples of galaxies.

Chapter 9

Conclusions

This thesis is substantially a report on work in progress. We however believe that all scientifical texts belong to this cathegory, as any achievement is the starting point of further advancements and any reply to physical questions opens new problems.

The overall connection of the work reported here is the quest for the nature of cosmic dark components, and Dark Energy (DE) in particular. Its very presence, in cosmological models able to fit data., is a clear indication of the distance still running from a reasonable understanding of the nature and origin of the world. When Albert Einstein discovered the possibility to introduce a DE term in his gravity equations, he first wrote a paper on it, then stated that it was *the worst blunder* in his scientifical life; as though he had *evocated* an evil, which should have been kept hidden in ignorance.

We are however confident that, when DE nature will become clear and its role will be fully perceived, the *ugliness* feeling will be completely erased by the self consistency of the general picture. In our opinion, however, this step is still far and much work is still needed.

Difficulties in understanding DE nature essentially arise from the weakness of signals. Laboratory esperiments on DE seem completely unimaginable. We must therefore refer to large scale analysis, and accept those data the Universe serves us, being unable to forge experimental devices to put ourselves in more favorable conditions.

In this thesis we considered two frameworks where DE nature affects observational materials: The anisotropies and polarization of the Cosmic Microwave Background (CMB) and the formation of cosmic structures.

As far as CMB is concerned, we also took part to the preparation of an experiment, aimed at measuring polarization on (fairly) large angular scales ($\theta >\sim 7^0$, as in the COBE experiment). This was the basic aim of our re-

search work until the finantial support of ASI faded and the SPOrt experiment, selected by ESA to fly on the ISS in 2007, was substantially closed.

CMB data are directly affected by DE nature. On large angular scales, the integrated Sachs & Wolfe (ISW) effect bends the C_ℓ curves and does so differently, according to DE state equations. It must be however acknowledged that using this effect is not simple, because of two main reasons: (i) On small scales cosmic variance is still high: the observable Universe contains too little realizations of the process creating fluctuations, when angles comparable with 4π are considered. (ii) There is a wide interplay between DE parameters and other parameters; when compared with the expected errors, only a detailed analysis can allow to state how much DE parameter can be fixed.

A first part of this thesis is therefore dedicated to the patterns to be followed to obtain information on DE nature from CMB experiments, taking then also into account SPOrt expected features. This work led to significant results, collected in a number of papers.

Among them a particular mention is deserved by a work discussing the measure of a cosmic features, which deeply intereferes with the ISW effest, and lead do the cosmic opacity to CMB photons, τ. The large value of τ, suggested by WMAP1 results, had strongly strengthened the SPOrt case, which appeared as the best seller experiment, to confirm WMAP findings and detail their features. Within this framework, various models of cosmic reionization were analysed, not only finding the related τ value, but also discussing how τ measures would depend on the experiment sensitivity, in the presence of different forms of DE. WMAP3 release yielded a value of τ smaller by a factor ~ 0.7; but the whole argument stil keeps its full validity.

We concluded the first part of this thesis with a very description of the SPOrt experiment itself, whose cancellation we deeply regret.

DE nature however affects also structure formation. While CMB features are obtainable from linear analysis, however, the formation of cosmic structures, as galaxies, galaxies groups and galaxy clusters, is intrinsically a non linear precess, and there is little hope to inspect it, if we prescind from simulations of model realizations.

There can be however little doubts that the dynamics of these systems feels the effects of DE nature. In order to make this point, it is worth reminding that galactic bodies are the smallest systems whose formation is essentially ruled by gravity. Smaller systems, inside galaxies, are essentially shaped by dissipative dynamics. Even galaxy formation is partially affected by non–gravitational

phaenomena. However, galaxy distributions on mass and in space are essentially ruled by non–dissipative dynamics, which can still be approached by n–body simulations.

Then, on scales greater than galaxies, pure gravity is the main dynamical agent. This does not mean that dissipative phaenomena are unimportant in our understanding of galaxy systems. For instance, the main emmission from galaxy clusters is due to X–ray photons, emitted by accelerated charges in free–free encounters, within the hot gas which fills them. However, the overall energy emitted in the whole history of a single cluster is negligible in comparison with its potential and kinetic energies. Times scales for dynamical actions of dissipative phaenomena are therefore too long, and the whole dynamics is to be referred to gravity.

This is why purely gravitational n–body simulations are suitable to gain knowledge on super–galactic systems. DE affects gravitational phaenomena in various ways. The basic actions, however, amount to a change of the overall expansion rate of the Universe and to a deep modification of its geometry.

The former effect must be taken into account when performing simulations, while the latter one becomes essential when we aim at comparing simulation results with observational material.

We started our simulation work within the cosmology group of Milano–Bicocca University, where a numerical algorithm (ART), created by Klypin & Kravtsov, had been modified to account for expansion rate alterations in different DE models. The first simulations of dynamical DE models have been performed there in 2003 and only a couple of groups are still able to perform similar simulations, all over the world.

In this thesis we report the physical modifications to be included in the ART code, in order to perform DE n–body simulations. We then describe the structure of the ART program, a fully parallel program, simultaneously using openMP and MPI parallelization techniques. We finally describe our approach to implementing this program on the Sp5 machine of the CINECA consortium.

We did so in a innovative fashion, which takes into account the target of our whole research program, and exploits in an original way the MPI parallelization, to run separate realizations rather than to inspect separate areas of a unique wider realization. This choice speeds up the computational procedure by a factor $\simeq N^{-1/2}$, $N = 32$ being the number of the nodes used. Without this device, our research would require $\sim$ 3 months of computations, reduced to little more than 2 weeks by our implementation.

When this thesis is being written, the computational work is in progress. We are therefore unable to report its results. It should be however outlined that, also when the whole set of outputs will become available, so that an important step forward wil have been accomplished, there will still be much work to do, to insert our outputs within a precise observational program.

This program is aimed at inspecting DE nature through *cosmic shear* analysis. Cosmic shear essentially arises from the *weak lensing* effect. Week lensing does not produce astonishing pictures, with multiple images, as strong lensing does. However, while strong lensing requires suitable geometrical settings of cosmic bodies, weak lensing is a systematic effect, difficult to analyse, but widespread.

Quite a few experimenal proposals were formulated to improve the analysis of weak lensing. Among them a particular mention is deserved by the DUNE experiment, which will be submitted to the ESA call issued om March 5, 2007. The results of the simulations in progress bear a significant weight in supporting such proposal, although their role is much farther reaching, and cannot be only connected with such important experimental program.

Let us therefore conclude this chapter by outlining once again that this thesis is a report on work in progress, which is inserted in far reaching research programs and will continue in the next few years.

Bibliography

[1] Aarseth, S.J., 1963, MNRAS, 126, 223

[2] Abel T., Mo H. 1998, ApJL, 494, 151

[3] Albrecht L. & Skordis R., 2000, Phys.Rev.Lett., 84, 2076

[4] Barnes J. & Hut P., 1986 Nature 324, 446

[5] Barreiro J., Copeland P. & Nunes F.G., 2000, Phys.Rev., D61, 127301

[6] Bartelmann M. et al. 1998, A&A 330, 1

[7] Bartelmann M., Perrotta F. & Baccigalupi C. 2002, A&A 396, 21

[8] R.H. Becker et al., AJ, 2001, 122:2850

[9] Benson, A. J. et al. 2002, MNRAS, 333, 156

[10] E.M. Berkhuijsen., 1975, A&A , 40:311

[11] Bertschinger, E., 1998, ARAA, 36, 599

[12] Brax P. & Martin J., 1999, Phys.Lett., B468, 40-45

[85] Brax P., Martin M. & Riazuelo A, 2000, Phys.Rev., D62, 103505

[14] Broadhurst, T. et al. 2000, ApJ, 534L, 15B

[15] Bullock J. et al. 2001, MNRAS, 321, 559

[16] J.S. Bullock, A.V. Kravtsov, and D.H. Weinberg. 2000, ApJ, 539:517

[17] M. Bucher, K. Moodley, and N. Turok., 1999, Phys. Rev. D, 62:083508

[85] Buchert T., 2000, Gen.Rel.Grav., 32, 105

[85] Buchert T., Kerscher M. & Sicka C., 2000, Phys.Rev., D62, 043525

[20] E.F. Bunn.2002 Phys. Rev. D, 65:043003.

[21] E.F. Bunn et al. 2003 Phys. Rev. D, 67:023501

[22] M. Bruscoli, A. Ferrara, and E. Scannapieco, 2002. MNRAS, 330:L43

[23] E. Carretti, R. Tascone, S. Cortiglioni, et al. 2001, NA, 6:173

[24] R. Cen. 2003, ApJ, 591:12

[25] R. Cen and P. McDonald, 2002, ApJ, 570:457

[26] G. Chon et al., 2004, MNRAS, 350:914

[27] B. Ciardi, A. Ferrara, and S.D.M. White, 2003. MNRAS, 344:L7

[28] Coles P. & Lucchin F., 1995, *Cosmology*, John Wiley & Sons.

[29] Colin, P., Avila-Reese, V., & Valenzuela, O. 2000, ApJ, 542, 622

[30] L.P.L. Colombo, 2004a., JCAP, 03:003

[31] L.P.L. Colombo and S.A. Bonometto, 2003, New Astr., 8:313

[32] L.P.L. Colombo and S.A. Bonometto, 2003, New Astr. Rev., 47:849

[33] L.P.L. Colombo, G. Bernardi and L. Casarini. 2005, A&A 435, 413C

[34] S. Cortiglioni et al. 2004, New Astr., 9:297.

[35] Dalal N.& Kochanek, C.S., 2002 572, 25D

[36] De Bernardis P., Ade P.A.R, Bock J.J. et al., 2000, Nature, 404

[37] de Blok, W.J.G. & McGaugh, S.S., 1997, MNRAS, 290, 533

[38] de Blok, W.J.G. et al., 2001, ApJ, 552. L23

[39] de Grandi et al., 1999, ApJ, 514, 148

[85] J. Delabrouille. 1998, A&A Suppl. Series, 127:555

[41] S.G. Djorgovski et al., 2001, ApJ, 560:L5

[42] S. Dodelson. 1997, ApJ, 482:577

[43] S. Dodelson, L. Knox, and E.W. Kolb, 1994, Phys. Rev. Lett., 72:3443

[44] Dressler A. et al 1999, ApJS, 122, 51D

[45] Ebeling H., 2000, MNRAS, 318, 333

[85] Ellis G.F.R., 1984, *General Relativity and Gravitastion*, Reidel Publishing

[47] X. Fan, R.L. White, M. Davis, et al., 2000, AJ, 120:1167

[48] X. Fan, V.K. Narayanan, M. Strauss, et al., 2002, AJ, 123:1247

[49] Ghigna et al., 2000, ApJ, 544, 616

[50] Gladders, M.D. & Yee, H.K.C., 2000, AJ, 120, 2148

[51] Gnedin, N. Y. 2000, ApJ, 535, 530

[52] N. Goldberg et al., 1967, *J.Math. Phys.*, 8:2155

[53] Gott R. & Rees M., 1975, A&A, 45, 365G

[54] Gunn J. & Gott J.R , 1972, ApJ, 176, 1G

[55] Guzzo L. et al 1999, The Messenger, 95, 27

[56] F.K. Hansen, A. Balbi, A.J. Banday, et al., 2004, MNRAS, 354, 905

[57] Z. Haiman, T. Abel, and M.J. Rees., 2000, ApJ, 534:11

[58] Z. Haiman and G.P. Holder., 2003, ApJ, 595:1

[59] Halverson, N.W. et al., 2002, ApJ 568 38

[60] Hanany S, Ade P., Balbi A. et al., 2000, ApJ, 545, L5

[61] S.H. Hansen and Z. Haiman., 2004, ApJ, 600:26

[62] Hernquist L., 1987, ApJ Suppl., 64 715

[85] Hinshaw G.et al. 2003, ApJ Suppl., 148, 135

[64] G.P. Holder, Z. Haiman, M. Kaplinghat, and L. Knox., 2003, ApJ, 595:13

[65] W. Hu and N. Sugiyama, 1996, ApJ, 471:542

[66] M. Kamionkowski and A. Loeb, 1997, Phys. Rev. D, 56:4511

[67] M. Kamionkowski, A. Kosowsky, and A. Stebbins., 1997, Phys. Rev. D, 55:7368

[68] Katz N., Weinberg D. H., Hernquist L., 1996, ApJS, 105, 19

[69] Kauffmann G., White, S. D. M., Guiderdoni, B., 1993, MNRAS, 264, 201

[70] Keeton C.R., Madau P., 2001 ApJ, 549, L25

[71] Kepner J. V., Babul A., Spergel D. N. 1997, ApJ, 487, 61

[85] Kim J.E., 1999, JHEP, 9905, 022

[73] W.H. Kinney. Phys. Rev. D, 58:123506, 1998.

[74] Klypin A. et al., 1999, ApJ 516, 530

[75] Klypin A. et al.. 2001, ApJ, 554, 903

[76] Klypin A. et al., 1999, ApJ, 522, 82

[77] Knebe A. et al., 2000, MNRAS, 317, 630

[85] Knebe A. et al., 2002, MNRAS, 329, 813

[79] A. Kogut, D.N. Spergel, C. Barnes, et al., 2003 ApJ Suppl. Series, 148:161

[85] Kolb E.W., Matarrese S. & Riotto A., 2005, astro-ph/0506534

[85] Kolb E.W. et al., 2005, Phys.Rev., D71, 023524

[82] L. Knox and M.S. Turner., 1996, Phys. Rev. Lett., 73:3347

[83] A. Kosowsky. Annals. Phys, 246:49, 1996.

[84] Kravtsov A., Klypin A. & Khokhlov A., 1997 ApJ, 111, 73 K

[85] Kristian J. & Sachs R.K., 1966, ApJ, 143, 379

[86] Lewis A., et al. 2003 ApJ, 586, 135

[87] Li L. & Ostriker J., 2002, AJ, 566, 652

[88] A. Loeb and R. Barkana., 2001, Ann. Rev. Astron. Astrophys., 39:19

[89] C. Ma and E. Bertschinger., 1995, ApJ, 455:7

[90] Maccio, A.V., Murante G. & Bonometto, S.A., 2003, ApJ, 588, 35M

[91] Macciò et al., 2004, Phys. Rev. D 69:123516

[92] P. Madau, M.J. Rees, M. Volonteri, et al. 2004. ApJ, 604:484

[93] Mainini R., Macciò A.V. & Bonometto S.A., 2003a NewA, 8, 173M

[94] Mainini R. et al., 2003b ApJ, December issue.

[95] D. Maino et al.1999, A&A. Suppl. Series, 140:383

[96] Mateo M. L., 1998, ARA&A, 36, 435

[97] McGaugh, S.S., de Blok, W.J.G., 1998, ApJ, 499, 41

[98] Meneghetti M.at al., 2000, MNRAS 314, 338M

[100] Metcalf, R.B. & Madau P., 2001 ApJ 563, 9

[100] Metcalf, R.B. & Zhao H., 2002 ApJ 567, 5M

[101] J. Miralda-Escudé. 2003, ApJ, 597:66

[102] Moore B. et al., 1999, ApJ, 524,19

[103] Moore B. et al., 1998, ApJ, 499, L5

[104] P. Naselsky and L.-Y. Chiang. 2004, MNRAS, 347:795

[105] Navarro, J. F., Frenk, C.S. & White S.D.M., 1996, MNRAS, 283, L72

[106] Navarro, J. F., Frenk, C.S. & White S.D.M., 1997, ApJ, 490, 493

[107] Nelson A.E. et al, 2002, ApJ, 566, 103

[108] Netterfield C.B. et al., 2002, ApJ 571 604

[109] K.W. Ng and G.C. Liu. 1999, Int. J.Mod. Phys., D8:61

[110] H.V. Peiris, E. Komatsu, L. Verde, et al. 2003, ApJ Suppl. Series, 148:213

[111] Peebles P.J.E., 1980, *The Large Scale Structure of the Universe*, Princeton University Press

[112] Percival W.J., Baugh C.M., Bland-H. J. et al., 2001, MNRAS, 327, 1297

[113] Perlmutter S. et al., 1999, ApJ 517, 565

[114] Power C. et al. 2003, MNRAS, 338, 14P

[115] W.H. Press and P. Schechter. 1974, ApJ, 187:425

[116] Quinn T., Katz N., Efstathiou G., 1996, MNRAS, 278, 49

[117] B. Ratra and P.J.E. Peebles. 1988, Phys. Rev. D, 37:3406.

[118] B. Revenu, A. Kim, R. Ansari, et al 2000, A&A Suppl. Series, 142:499.

[119] J. E. Rhoads and S. Malhotra. 2001, ApJ, 563:L5.

[120] M. Ricotti and J.P. Ostriker.2004, MNRAS, 350:539.

[121] A.G. Riess, A.V. Filippenko, P. Challis, et al. 1998, AJ, 116:1009

[122] R.K. Sachs and A.M. Wolfe. 1967, ApJ, 147:73

[123] Sahni L. & Wang, H., 2000, Phys.Rev., D62, 103517

[124] Salucci, P., 2001, MNRAS, 320, L1

[125] Sand, D., Treu, T., Graham P. & Ellis R., 2003, astro-ph/0309465

[126] Schuecker P., Bhringer H., Collins C.A. & Guzzo L., 2003, A&A, 398, 867

[127] Schuecker P. et al, 2003 astro-ph/0211480, A&A (in press)

[128] U. Seljak and M. Zaldarriaga., 1996, ApJ, 469:437

[129] U. Seljak and M. Zaldarriaga., Phys. Rev. Lett., 78:2054, 1997.

[130] N. Seto and M. Sasaki. 2000, Phys. Rev. D, 62:123004

[131] Shapiro, P. & Iliev I., 2000 ApJ 542L, 1S

[132] Sheth R.K., Mo H.J. & Tormen G., 2001, MNRAS, 323 ,1

[133] Sheth R.K. & Tormen G., 1999, MNRAS, 308, 119

[134] Sheth R.K. & Tormen G., 2002, MNRAS, 329, 61

[135] A. Sokasian et al., 2004, MNRAS, 350:47

[136] A. Songaila and L.L. Cowie., 1996 AJ, 112:335

[137] A. Songaila., 1998, AJ, 115:2184

[138] Spergel D.N. et al., 2003, ApJ Suppl. Series, 148, 175

[139] Steinhardt P., Wang L. & Zlatev I., 1999, Phys.Rev., D59, 123504

[140] R. Stompor et al., ApJ, 516:L7, 2001.

[141] R.A. Sunyaev and Ya.B. Zel'dovich., 1969. Comm. Astrophys. Space Phys, 4:173

[142] Swaters R.A. et al., 2003 ApJ, 583, 732

[143] M. Tegmark., 1997. Phys. Rev. D, 56:4514

[144] M. Tegmark, J. Silk, M. Rees, et al., 1997 ApJ, 474:1

[145] Tegmark M. et al., 2004, Phys.Rev. D69, 103501

[146] N. Turok A. Lewis, A. Challinor., 2002. Phys. Rev. D, 65:023505

[147] Tyson, A., Kochanski, G.P. & dell'Antonio, I. ApJ, 498L, 107T

[148] van den Bosch al., 2000, AJ, 119, 1579

[149] van den Bosch, F. C., Swaters, R. A. 2001, MNRAS, 325, 1017 (vdBS)

[150] Verde L. et al. 2003 ApJS, 148, 195V

[151] Weinberg M. D., Hernquist, L. & Katz, N. 1997, ApJ, 477, 8

[152] Wetterich C., 1998, Nucl. Phys. B 302, 668

[153] Wetterich C., 1995, A&A, 301, 321

[154] E.J. Wollack. 1995 Rev. Sci. Instr., 66:435

[155] J. Wyithe, B. Stuart, and A. Loeb., 2003. ApJ, 586:693

[156] M. Zaldarriaga., 1998. ApJ, 503:1

[157] M. Zaldarriaga and D.D. Harari., 1995. Phys. Rev. D, 52:3276

[158] M. Zaldarriaga and U. Seljak., 1997. Phys. Rev. D, 55:1830

[159] M. Zaldarriaga and U. Seljak., 1998. Phys. Rev. D, 58:023003

[160] Zlatev I., Wang L. & Steinhardt P., 1999, Phys.Rev.Lett., 82